SAPIENZA
UNIVERSITÀ DI ROMA

Dipartimento di Ingegneria Meccanica e Aerospaziale

Dottorato di Ricerca

Meccanica Teorica e Applicata

XXXII Ciclo

Coarse Grained modelling of nanopore systems

Candidato:

Alberto Gubbiotti

Docente guida:

Prof. Mauro Chinappi

Tutor:

Prof. Carlo Massimo Casciola

Abstract

Nanopore devices are a class of nanofluidic systems which involve the transport of mass and ions through a nanometer sized pore. These systems are widely studied for their attractive applications, ranging from biological analysis (e.g. real-time study of enzyme kinetics, macromolecule detection or sequencing), to blue energy harvesting. Despite their widespread potential applications and the increasing interest of the scientific community, the actual design of nanopore based devices remains a major challenge in the field. In fact, most analytical models fail the quantitative prediction of experimental data, since the assumptions on which they are based often fail in the extremely small nanopore region.

The relevant effects to be taken into account in order to model nanopore systems with reasonable accuracy are: i) at the nanometer scale, thermal fluctuations play a major role in the dynamics of mass and ion transport, consequently, the fluid cannot be treated with a deterministic set of equations. ii) the presence of the confining boundaries at nanoscale induces additional effects due to hydrodynamic interactions with particles moving in the pore region. iii) the presence of surface charges modify the equilibrium ionic distribution, giving rise to peculiar electrohydrodynamic phenomena such as

current rectification and electroosmosis. iv) when dealing with large biological molecules such as proteins, the additional complexity of dealing with their complicated structure has to be considered. A well-known approach which takes into account these physical features is all-atoms Molecular Dynamics, which has been thoroughly used to study many different nanopore systems. Despite their undeniable usefulness, Molecular Dynamics simulations are limited both in the size of the systems which can be simulated and in the total simulated time.

In this thesis, Coarse Grained models are employed to study the dynamics of confined systems on time and space scales not easily accessible to all-atoms Molecular Dynamics. The Coarse Graining of the system is performed by retaining only some of its degrees of freedom, dropping the remaining ones considered not relevant for the desired level of description. The equations of motion are then written for the selected variables, while the action of the dropped variables is introduced as a proper random forcing in the equations of motion. In this thesis, two different levels of Coarse Graining are considered. The first one is Brownian Dynamics for confined rigid particles, the second is a particle based model of the electrolyte fluid based on Dissipative Particle Dynamics.

For what concerns Brownian dynamics of confined rigid particle, the Langevin equation governing the translations and rotations in confined environment is derived. The rotational motion of the particle is based on the quaternion formulation. The effect of confinement is introduced via a configuration dependent mobility matrix. A Brownian code which integrates the equation of motion has been set up, and the dynamics of a spherical rigid

particle diffusing in a nanochannel is studied. The effect of confinement as well as the effect of different force fields on the diffusion of the particle is investigated. The results are in good agreement with experimental evidence.

The second Coarse Grained approach analyzed in this thesis concerns the description of the hydrodynamics of electrolyte solutions including the coupling between hydrodynamic and ionic transport in the nanopore (i.e. electrohydrodynamics), which is crucial in several applications. A new Coarse Grained model based on Dissipative Particle Dynamics is proposed and validated. The model considers each particle to carry a quantity of positive or negative ions. The energy of the system, including the chemical potential due to the concentration of each specie and to the presence of the electric potential, is written as a function of the Coarse Grained variables (positions, velocities and number of ions). A set of ordinary stochastic differential equations has been derived for which the equilibrium distribution is the Boltzmann distribution associated to the chosen thermodynamic potential. The model has been implemented into the LAMMPS software and has been validated against a number of cases for which the analytical solution is available.

Contents

Part I

Introduction

In this part, nanopore systems and some of their applications are introduced. The typical length and time scales as well as the relevant physical phenomena acting on such systems are reported. Two physical phenomena which are crucial in nanopore systems are discussed, i.e. the diffusion in confined environment and the coupled dynamics of ions and fluids in electrolytes, the so-called electrohydrodynamics. The Brownian motion in presence of a nonuniform mobility is briefly discussed. The Poisson-Nernst-Planck-Navier-Stokes equations for the electrohydrodynamics are reported, as well as the equilibrium distribution approximation leading to the Poisson-Boltzmann equation.

Chapter 1

Nanopore Systems

In the last decades, the development of techniques capable of shaping matter at the nanometer scale [1, 2, 3] gave rise to multiple possibilities in the conception of devices with nanometric features for a wide range of applications [4, 5, 6, 7]. In addition to the technological issues related to the reproducible fabrication of nanodevices [8, 9, 10], their design is also challenging from a physical point of view. In fact, the dynamics of systems at nanoscale is dominated by phenomena which are usually negligible for larger sizes, two well-known examples being thermal fluctuations leading to diffusion [11, 12] and surface effects causing the aggregation of particles [13, 14]. A class of nanoscale systems in which these physical features are of mayor importance involve transport of fluids and particles in nanometer sized channels or along nanostructured surfaces [15, 16, 17] , i.e. nanofluidic systems [18]. This thesis is devoted to the study of an important type of nanofluidic systems known as nanopores. Nanopore systems can differ considerably among each other both in the geometrical features and in the materials which are made

of. However, three common elements can be distinguished in most cases, sketched in Figure 1.1a:

- Two chambers are filled with a solution, usually electrically conductive.
- A pored membrane separates the two chambers, the pore or part of it being of nanometric size.
- Two electrodes are placed in the chambers, controlling the voltage difference and measuring the current passing through the pore.

In some cases the informations about the pore state can be obtained by optical measurements instead of electrical ones. This is the case of plasmonic nanopores [19], in which the fluid does not have to be conducting. In general, the nanopore can be a solid state nanopore with different geometries [20] or a biological one, with a variety of different biological channels which can be possibly used [21].

The most known and studied application of nanopore systems is to use them as biological sensors able to retrieve information at a single molecule level [22]. The first idea of a nanopore device as single molecule biosensor was proposed in the late '80s [23] with the aim of sequencing the DNA molecule. The basic principle was simple: a DNA molecule is forced to translocate through the pore by electrophoresis in presence of a potential difference between the chambers. During the translocation, the ionic current flowing through the pore is influenced by the presence of the DNA, provided the pore to be of size comparable to the size of a DNA filament. The ionic current variations can be measured and are related to the nucleobasis which is clogging the pore. The functioning of DNA nanopore sequencing is sketched

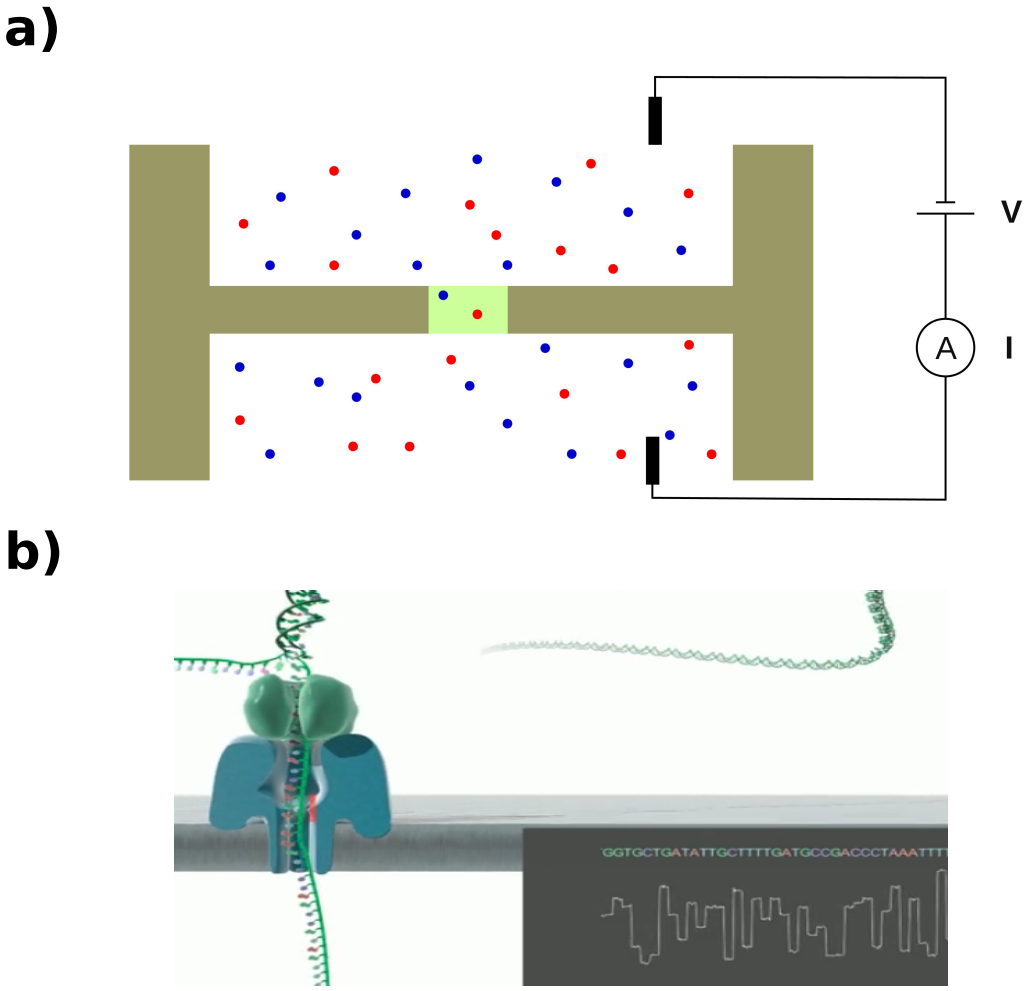

Figure 1.1: a) Sketch of a typical nanopore system set-up with its elementary elements. Two chambers are filled with an electrolyte solution. The chambers are separated by a membrane in which a nanometer sized pore has been made. Two electrodes are placed in the chambers, controlling or measuring the voltage difference between the chambers and the ionic current flowing through the pore. b) Representation of a DNA nanopore sequencing system. A single strand of DNA translocates through a biological nanopore driven by the electric field. Four different levels of ionic current are associated with the four nucleobasis, providing the DNA sequence of a single molecule in real time.

in Figure 1.1b. Despite this simple working principle, it took more than twenty years for DNA sequencing with nanopores to be a reality [24].

Today, nanopores are widely used to study biological systems containing macromolecules [27, 28, 25] obtaining information at a single molecule level which is unaccessible to more conventional measuring techniques, based on average properties of a mixture containing a high number of analytes. A possible application in this field is protein fingerprinting, in which a protein translocates through the nanopore driven by the electric field, electroosmotic flow [29], dielectrophoretic trapping [30] or simply by Brownian motion. The current trace modification caused by the translocation is used to obtain information about the charge, size and shape of the protein. This working principle is represented in Figure 1.2a.

As an example, solid state track-etched conical nanopores can be used to study amyloid aggregation [31]. If specific conditions of pH and temperature are met, a variety of proteins including β-lactoglobulin [32] aggregate to form fibrillar structures. The kinetics of this aggregation process is of interest in food industry [33] and medicine [34]. As a consequence of the amyloid aggregation, a solution containing β-lactoglobulin after the formation of fibrils will result in a mixture of linear protein aggregates with heterogeneous length. Usual techniques for characterizing the aggregates such as Diffusion Light Scattering (DLS) [35] only provide average informations about the mixture, while a single-molecule technique such as nanopore sensing can in principle discriminate fibrils with different sizes, obtaining a real-time information about the aggregation process and the distribution in size of the aggregates [31]. Other challenges in the use of nanopores as bi-

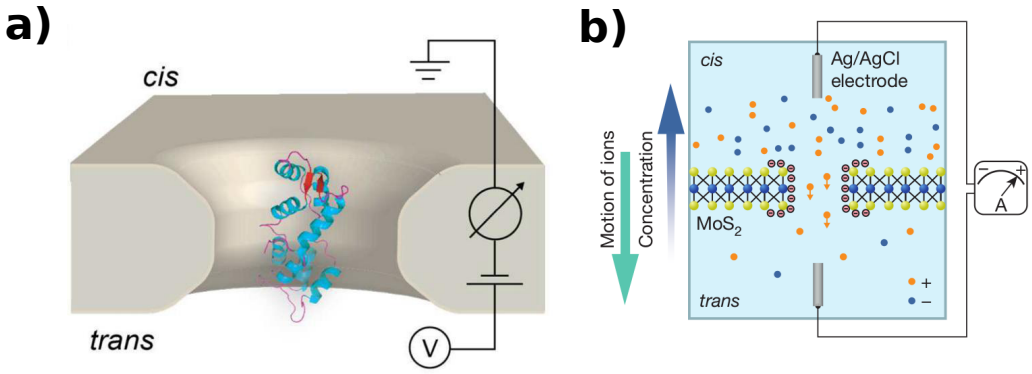

Figure 1.2: Two examples of applications of nanopore systems which have been object of research in the last years. a) Protein fingerprinting (image adapted from Waduge *et al.*, reference [25]). A protein translocates through a nanopore driven by electric field, dielectrophoretic trapping, electroosmotic flow or simple diffusion. The translocation modifies the ionic current flowing through the nanopore. The resulting current trace is associated to different properties of the protein (charge, shape,volume) with the aim of identifying it. b) Nanopore set-up for energy extraction from a salt gradient (image adapted from Feng *et al.*, reference [26]) Two solutions with different salt concentrations are placed in both sides of the nanopore. The nanopore has a net surface charge, and hence it is selective for the ions of opposite sign. As a consequence, the total ion fluxes flowing through the pore will be unbalanced, and a net current flows through the electrodes.

ological sensors involve discriminating among proteins in a solution, either via sequencing [36], as already possible in the case of DNA, or by inferring the shape, size, surface charge of a protein from the current trace registered during translocation, the so-called protein fingerprinting [37].

Nanopore sensing is not the unique appliaction of nanopore devices. The high versatility of such devices is directly related with the high versatility of biological channels [21], whose permeability depend on the charge, shape and chemical properties of the species translocating through them, and can be modulated by multiple external factors such as electric fields, pH, pressure gradients, salt concentration. Inspired by biological nanopores which can be selective for cations, anions, and even for specific ionic species [38], solid state nanopores with ionic selectivity can be realized [39]. Ion-selective nanopores can be used to extract energy from a ionic concentration difference between solutions [40, 26], also known as blue energy production. The selectivity is related to a difference in the conductivity for different ionic species and can be due to the surface charge of the nanopore combined with its shape. Hydrophobic nanopores in which the pore is unaccessible to ions due to the vapour phase water clogging the pore can be used combined with a pressure gradient to desalinate salted water [41].

Despite the great interest arisen by nanopores in the scientific community and the relevant progress made in the understanding of nanopore systems, the modelling and design of devices capable of disruptive applictions such as the above cited protein sequencing [36], protein fingerprinting [37] and energy harvesting from a salt gradient [42] are still open problems. The reason for the design of nanopore systems to be challenging lies in the complex

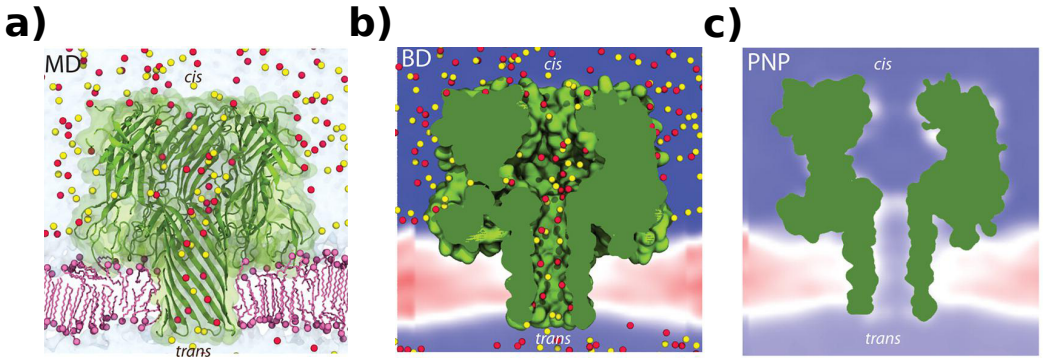

Figure 1.3: Sketch of three possible techniques used to simulate nanopore systems, with different degrees of accuracy and computational cost (image adapted from Maffeo *et al.*, reference [21]). a) All-atoms Molecular Dynamics. The trajectory of every atom of the system is simulated solving the equations of motion with appropriate force fields. It is computationally expensive and very accurate since thermal fluctuations, hydrodynamics, electrostatic interactions, polarization of molecules and the dynamics of biomolecules are taken into account. b) Brownian Dynamics. A mesoscale approach in which the state of the system is represented by the positions and velocities of coarse grained particles representing groups of atoms and molecules moving coherently. It is faster than Molecular Dynamcs and in principle can take into account most of the relevant features for nanopore systems, given that the equations of motion are properly modelled. c) Continuum approach. A continuum model in which the Poisson-Nernst-Planck equations of motion for the cationic and anionic concentrations are solved, modelling the ionic flux with a diffusive term and a drift term related to the conductivity of the solution. It is the less expensive approach from a computational point of view, but it lacks a description of the effects of thermal fluctuations.

physics involved in the mass transport dynamics at nanometric scales. Ions, solvent and particle transport across the nanopore are generally coupled and influenced by many different factors, including thermal fluctuations, external voltage and pressure difference, hydrodynamic, electrostatic and chemical interactions with the confining walls. An additional complexity exists in the case of translocation of biomolecules and/or in the case of biological channels as nanopores, given by the high number of degrees of freedom of such objects which affects the translocation dynamics in ways which are difficult to predict [43].

In this complex scenario, for what concerns nanopores as biosensors, their design demand to solve three technological tasks [44]:

- The particle has to be transported near the pore zone (capture control).
- It has to translocate at a sufficiently low speed to generate a detectable signal (translocation control).
- Different particles (or different parts of a single molecule, as in nanopore sequencing) should induce different signals (distinguishability).

Ideally, the desire is to associate the current blockade generated by the translocation event to some properties of the object which is translocating, such as charge, shape and volume [45]. Such relation is not deterministic due to the thermal fluctuations dominating the dynamic of the translocating particles, and must therefore be expressed in terms of the probability of an event to have a certain relative blockade and dwell time. The experimental determination of the probability distribution is possible by direct observation of the signal produced by a known analyte. However, it depends strongly on

the pore shape, size, charge and chemical composition, which is not always exactly reproducible. It is in general cumbersome to predict the effects of small variations of the system set up on the above cited probability distribution. Even if there is no translocation event, as in the case of blue energy applications, complex and nonlinear effects may arise from the coupling between hydrodynamics and electrostatics [46, 47]. This is even more true in the case of a translocation of a charged object, as is the case of most biological molecules. In this complex context, computational approaches are very useful to have insights into the physical phenomena influencing nanopore experiments and have been widely used. The most used computational tool to study nanopore systems is all-atom molecular dynamics, due to its capability to consider all the relevant effects (thermal fluctuations, hydrodynamic and electrohydrodynamic effects, complexity of biological molecules). However, all-atoms molecular dynamics is limited in size and temporal length of the simulated systems due to its high computational cost. For this reason, many relatively large nanopore systems [48] and/or relatively slow translocation events can't be studied with this tool. These problems are often tackled with analytical reduced models based on strong assumptions such as bulk diffusion, uniform conductivity of the solution, zero surface charge [31]. Although this reduced models may be accurate in some cases and can help a quick understanding of the dominant phenomena in a particular system, the quantitative predictions based on simplified models often fail the experimental data prediction by orders of magnitude [49].

This has given reason for the study of intermediate mesoscale models able to drop the great number of degrees of freedom in all-atoms molecular

dynamics while at the same time retaining the relevant degrees of freedom needed for the model to be predictive. The process of understanding which are the relevant degrees of freedom in a system and of finding a model for the dynamics of such relevant degrees of freedom is called the coarse-graining of a system. With this spirit, Brownian Dynamics computational models have been developed and used to reduce the computational cost of all-atom Molecular Dynamics simulations. In such models, the state of the system is described in terms of the positions and velocities of coarse-grained particles representing groups of atoms or molecules moving coherently. The explicitly described degrees of freedom are assumed to be "slow" degrees of freedom, meaning that the effects of the dynamics of the remaining "fast" degrees of freedom is to introduce a noise term in the equation of motion, which are now non deterministic. A technique which allows to simulate even larger systems is the continuum approach adopted to solve the Poisson-Nernst-Planck equations. In this approach, the state of the system is described by the concentration fields of cations and anions, respectively c^a and c^c, functions of space and time. The cation and anion concentrations obey a continuity equation in which the fluxes are modelled with a diffusive and a conductive term. In addition, the system has to obey the Poisson equation of electrostatics. A generalization of this kind of approach to include the fluid dynamics of the system leads to the Poisson-Nernst-Planck-Navier-Stokes equations and will be briefly reported in section 1.2. These approaches allow the simulation of large systems, with the main drawback that thermal fluctuations are completely neglected. A sketch which synthesizes the three approaches cited here, from the more computationally expensive and accurate Molecu-

lar Dynamics to the coarse-grained Brownian Dynamics to the continuum Poisson-Nernst-Planck is reported in Figure 1.3 This thesis deals with two important phenomena in nanopore systems: the presence of the fluid in which eventually the particle moves in a confined environment (hydrodynamic interactions) and the presence of dissolved charged species which mediate the electrostatic interactions between charged objects and whose dynamic is, in general, coupled with the solvent (electrohydrodynamics).

1.1 Hydrodynamic interactions

At low Reynolds numbers, a typical condition in micro and nano fluidic systems, the (incompressible) Navier-Stokes equations governing the dynamics of incompressible fluids can be linearized into the simpler Stokes equation

$$0 = -\boldsymbol{\nabla} P(\boldsymbol{x}) + \eta \nabla^2 \boldsymbol{u}(\boldsymbol{x}) \, , \tag{1.1}$$

with the incompressibility condition

$$\boldsymbol{\nabla} \cdot \boldsymbol{u}(\boldsymbol{x}) = 0 \, , \tag{1.2}$$

where $\boldsymbol{x}$ is the spatial position, $\boldsymbol{u}$ is the velocity of the fluid, P is the pressure field and η is the fluid viscosity.

Considering a rigid particle moving in such fluid in a domain Ω, (at least) two different boundaries can be identified $\partial\Omega = \partial^i\Omega \cup \partial^e\Omega$. The internal boundaries $\partial^i\Omega$ correspond to the fluid-particle interface, in which the velocity is $\boldsymbol{u}_0$. The external boundaries $\partial^e\Omega$ correspond to the confining walls, plus the free fluid-fluid boundary. If the walls are fixed and satisfy the no-slip boundary condition, and if the fluid-fluid boundary is located sufficiently far

from the moving particle, the velocity on the external boundary vanishes. Thus, the forces exerted on the particle by the fluid can be computed finding the stationary solution of the Stokes equation corresponding to system of Eq. 1.1 with boundary conditions

$$\begin{cases} \boldsymbol{u}(\boldsymbol{x}) = \boldsymbol{u}_0 \quad \boldsymbol{x} \in \partial^i\Omega \ , \\ \boldsymbol{u}(\boldsymbol{x}) = 0 \quad \boldsymbol{x} \in \partial^e\Omega \ . \end{cases} \tag{1.3}$$

If also rotations of the particle are considered, the boundary conditions become

$$\begin{cases} \boldsymbol{u}(\boldsymbol{x}) = \boldsymbol{u}_0 + \boldsymbol{\omega} \times (\boldsymbol{x} - \boldsymbol{x_0}) \quad \boldsymbol{x} \in \partial^i\Omega \ , \\ \boldsymbol{u}(\boldsymbol{x}) = 0 \quad \boldsymbol{x} \in \partial^e\Omega \ , \end{cases} \tag{1.4}$$

where $\boldsymbol{\omega}$ is the angular velocity of the particle and $\boldsymbol{x}_0$ the position of its center. Since the Stokes equation is linear, so is the response of the fluid to the presence of a rigid particle moving at a certain velocity. This proportionality relation is expressed via the mobility matrix $\boldsymbol{M}$

$$\boldsymbol{v} = \boldsymbol{M}\boldsymbol{f} \ , \tag{1.5}$$

where $\boldsymbol{v}$ is the velocity of the body and $\boldsymbol{f}$ is the friction force which the fluid exerts on the body. In general, $\boldsymbol{v}$ can be seen as the 6-D vector of linear and angular velocity while $\boldsymbol{f}$ can be seen as the 6-D vector of forces and torques exerted by the fluid on the body, and hence $\boldsymbol{M}$ is a 6×6 matrix. In principle, $\boldsymbol{M}$ depends at each time on the boundary conditions of the problem, and hence changes if the particle changes its orientation or moves with respect to the confining walls of the system.

As a consequence, in the case of rigid particle, its dynamics in a confined environment needs to consider configuration dependent mobility matrices in

order to properly account the effect of the solvent. At nanometric scales, when a Brownian description of the particle motion is needed, the deterministic forces exerted on the particle by the fluid are linked to the random forces due to the thermal fluctuations the via the fluctuation-dissipation relations [50, 51]. As a consequence, the confinement affects not only the deterministic part of the particle trajectory (the so-called drift), it also affects its thermal motion.

This effect is particularly important in particle transport through nanopores, since at nanometric scales the thermal fluctuations play a major role in particle dynamics. Also,the translational trajectory of a rigid particle can be affected by its rotational dynamics, since the mobility matrix is in general non diagonal, also for spherical particles in presence of confining walls. This is intuitively clear for a no-slip wall, where translations are coupled with rotations, leading to a non-diagonal mobility matrix [52].

In Part II the effects of confinement on the dynamics of a rigid particle in a nanochannel are studied via a rigid body Brownian motion approach [53]. It will be shown that confinement not only affects the translational diffusion, but also modifies the rotational diffusion of the particle, which has to be considered when non spherical particles or particles with a dipole moment translocate through the pore and interact with it at some preferential orientations. Also, it will be shown that under confinement, external forces acting on the particle change its diffusive properties, and not only their average motion.

1.2 Electrohydrodynamics

Electrohydrodynamics deals with the coupled motion of fluids and ions [54]. Such coupling has relevant effects in microfluidics, allowing manipulation of fluids or dispersed particles using electrical stimuli [55]. Electrohydrodynamic effects are of crucial importance are nanopore systems [20]. When a fluid containing ions is located in a confined region as the nanopore, the eventually charged confining surface induces a net motion of fluid in response to an external electric field. The resulting flow is known as electroosmotic flow, and it has been shown to take place both in synthetic [56, 47] and in biological [57, 58, 59] nanopores. The electroosmotic flow can be the dominant effect governing the translocation of particles or molecules through a nanopore [29, 58], and can generate interesting phenomena such as current rectification [56] or complex velocity profiles [60].

In such conditions, the incompressible Navier-Stokes equation is not sufficient to solve the fluid dynamics of the system, and the Nernst-Planck equations for the transport of species must be added, together with the Poisson equation of electrostatics [54]. The resulting set of equations is called the Poisson-Nernst-Planck-Navier-Stokes system

$$\begin{aligned}
\frac{\partial \boldsymbol{u}}{\partial t} + \boldsymbol{u}\boldsymbol{\nabla}\boldsymbol{u} &= -\boldsymbol{\nabla}P + \nabla^2\boldsymbol{u} + (c^a - c^c)\boldsymbol{\nabla}\phi \\
\boldsymbol{\nabla}\cdot\boldsymbol{u} &= 0\ , \\
\frac{\partial c^c}{\partial t} + \boldsymbol{u}\cdot\boldsymbol{\nabla}c^c &= \boldsymbol{\nabla}\cdot(c^c\boldsymbol{\nabla}\phi) + \nabla^2 c^c\ , \\
\frac{\partial c^a}{\partial t} + \boldsymbol{u}\cdot\boldsymbol{\nabla}a^c &= -\boldsymbol{\nabla}\cdot(c^a\boldsymbol{\nabla}\phi) + \nabla^2 c^a\ , \\
\nabla^2\phi &= c^a - c^c\ ,
\end{aligned} \tag{1.6}$$

where $\boldsymbol{u}$ is the fluid velocity, P is the pressure, c^c and c^a are the cationic and anionic concentration fields and ϕ is the potential. All the transport coefficients, the fluid density, the dielectric constant and the charge of the ions have been set to unity. A possible way to simplify this system is to assume that, at the equilibrium, the ionic concentration is given by the Boltzmann distribution, i.e.

$$\begin{aligned} c^c &= c_0 \exp(-\phi) \ , \\ c^a &= c_0 \exp(\phi) \ , \end{aligned} \tag{1.7}$$

where c_0 is a reference concentration at 0 potential. With these conditions, the Poisson equation becomes

$$\nabla^2 \phi = -2c_0 \sinh(\phi) \ , \tag{1.8}$$

which is known as the Poisson-Boltzmann equation. If the Poisson-Boltzmann equation is solved and the potential is found, the electrostatic forcing term in the Navier-Stokes equation becomes a known forcing and the equations decouple. The net flux caused by the electrostatic forcing is called electroosmotic flow and is of great importance in many nanopore applications [29, 59].

Chapter 2

Coarse grained models

The aim of coarse grained models is to describe the dynamics of the system with a different and reduced set of variables with respect to all-atom models, introducing non deterministic terms in the equations of motion which represent the overall effect of the dropped degrees of freedom. The level of coarse graining has to be chosen based on the relevant features of the problem and on the desired level of accuracy. In this thesis, two different models are explored, the Brownian dynamics of particles in confined environments, in which the solvent is not explicitly represented but still acts via the (space dependent) mobility matrix, and Dissipative Particle Dynamics (DPD) [61], a particle method in which the solvent is explicitly represented and composed of interacting particles. Here both techniques are briefly introduced.

2.1 Brownian motion

Consider a point particle immersed in a fluid solvent that acts as a thermal bath at temperature T. The particle mass is assumed to be sufficiently small to neglect inertia, the so-called overdamped regime. The aim is to model the motion of the particle in the inhomogeneous environment where solid walls limit the mobility. To do this, a possibility is to obtain the Fokker-Planck equation for the probability density function (pdf) of the particle associated to the Langevin equation

$$\dot{\boldsymbol{x}}\,(t) = \boldsymbol{u}(\boldsymbol{x}) + \boldsymbol{G}(\boldsymbol{x})\boldsymbol{\xi}(t)\ . \tag{2.1}$$

where $\boldsymbol{x}$ is the particle position vector in the three dimensional space and $\boldsymbol{u}$ is the drift velocity. $\boldsymbol{G}(\boldsymbol{x})\boldsymbol{\xi}(t)$ is a stochastic term with $\boldsymbol{\xi}$ the vector of white noise stochastic processes and $\boldsymbol{G}(\boldsymbol{x})$ a 3×3 matrix, the noise intensity operator, to be discussed in the following.

This term accounts for the fluctuations in the particle velocity induced by the interaction with the thermal bath forming the environment. The drift term basically accounts for the average motion induced by external forces $\boldsymbol{f}$ through the particle friction (in fact its inverse, the mobility) with the environment plus additional effects whose origin is better specified below. In this thesis, the Itô convention for the interpretation of stochastic differential equations is used. The reader may refer to Lau and Lubensky [62] work for a discussion on the role of the different conventions in the correspondence between the Fokker-Planck and the Langevin equations. Integrating eq. (2.1), the trajectory $\boldsymbol{x}(t)$ of the particle can be obtained for a given realization of the noise $\boldsymbol{\xi}$. The probability density function (pdf) of the particle position

at time t is

$$P(\boldsymbol{x}\,', t) = \langle \delta(\boldsymbol{x}\,' - \boldsymbol{x}(t)) \rangle \ , \tag{2.2}$$

where the expectation value, denoted by angular brackets, is taken over the realizations of the noise $\boldsymbol{\xi}$. The pdf obeys the Fokker-Planck equation

$$\frac{\partial P}{\partial t} = \boldsymbol{\nabla} \cdot \left[\left(-\boldsymbol{u} + \frac{1}{2} \boldsymbol{\nabla} \cdot \left(\boldsymbol{G}\boldsymbol{G}^T \right) + \frac{1}{2} \boldsymbol{G}\boldsymbol{G}^T \boldsymbol{\nabla} \right) P \right] \quad . \tag{2.3}$$

If the external force is conservative, $\boldsymbol{f} = -\boldsymbol{\nabla} U$ with U the potential energy, the equilibrium pdf has the canonical expression

$$P_{eq}(\boldsymbol{x}) = \frac{1}{Z} e^{-\beta U} \ , \tag{2.4}$$

where Z is the normalization factor and $\beta = (k_B T)^{-1}$, with k_B the Boltzmann's constant. In the low Reynolds number limit, the response to the external force reads $\boldsymbol{M}\boldsymbol{f}$ with $\boldsymbol{M}$ the hydrodynamic mobility matrix [52] that is always symmetric and positive definite. For the stationary Fokker-Planck equation to admit the equilibrium pdf (2.4) as a solution, the drift term must be written as [62]

$$\boldsymbol{u} = -\boldsymbol{M}\boldsymbol{f} + \boldsymbol{u}\,' \ , \tag{2.5}$$

where $\boldsymbol{u}\,'$ is an additional field. Pretending that equation (2.4) is the equilibrium solution ($\partial P / \partial t = 0$) of the Fokker Plank equation

$$0 = \boldsymbol{\nabla} \cdot \left[\left(\boldsymbol{M}\boldsymbol{f} - \boldsymbol{u}\,' + \frac{1}{2} \boldsymbol{\nabla} \cdot \left(\boldsymbol{G}\boldsymbol{G}^T \right) - \frac{1}{2} \boldsymbol{G}\boldsymbol{G}^T \boldsymbol{f} \right) e^{-\beta U} \right] \ , \tag{2.6}$$

provides two constraints relating the additional drift $\boldsymbol{u}\,'$, the mobility matrix field $\boldsymbol{M}(\boldsymbol{x})$ and the noise intensity operator $\boldsymbol{G}$. Assuming the mobility to be given, the two constraints provide equations for the noise intensity operator $\boldsymbol{G}$ and the additional drift $\boldsymbol{u}\,'$, namely:

1- the matrices $\boldsymbol{M}$ and $\boldsymbol{G}$ are related by the fluctuation-dissipation relation

$$\boldsymbol{G}\boldsymbol{G}^T = \frac{2}{\beta}\boldsymbol{M}\,, \tag{2.7}$$

2- the additional drift term $\boldsymbol{u}'$ reads

$$\boldsymbol{u}' = \frac{1}{\beta}\boldsymbol{\nabla}\cdot\boldsymbol{M}\,. \tag{2.8}$$

As discussed in Lau and Lubensky [62], the operator $\boldsymbol{G}$ is not uniquely defined since it can always be multiplied by any orthogonal matrix without altering the Fokker-Plank equation. In fact, this transformation corresponds to a rotation of the noise vector $\boldsymbol{\xi}$ which leaves the Langevin equation (2.1) invariant. The final overdamped Langevin equation for a point particle reads,

$$\dot{\boldsymbol{x}} = -\boldsymbol{M}\boldsymbol{\nabla}U + \frac{1}{\beta}\boldsymbol{\nabla}\cdot\boldsymbol{M} + \boldsymbol{G}\boldsymbol{\xi}\,. \tag{2.9}$$

2.2 Dissipative Particle Dynamics

A technique which has been widely used to simulate mesoscale systems is Dissipative Particle Dynamics (DPD) [61]. In the DPD framework, the fluid is represented by a system of pairwise interacting particles [63, 64].

Considering N particles interacting inside a domain of volume V, the interactions are described in terms of a conservative force $\boldsymbol{F}^C$, a dissipative force $\boldsymbol{F}^D$, and a random force $\boldsymbol{F}^R$. The equation of motion of the i^{th} particle is hence

$$m\ddot{\boldsymbol{r}}_i = \sum_{j\neq i}^{N}\left(\boldsymbol{F}_{ij}^C + \boldsymbol{F}_{ij}^D + \boldsymbol{F}_{ij}^R\right)\,, \tag{2.10}$$

where m is the particle mass and $\boldsymbol{r}_i$ its position. The forces acting between particles i and j are

$$\begin{aligned} \boldsymbol{F}_{ij}^{C} &= a w^{C}(r_{ij}) \boldsymbol{e}_{ij} \ , \\ \boldsymbol{F}_{ij}^{D} &= -\gamma w^{D}(r_{ij}) \left(\boldsymbol{v}_{ij} \cdot \boldsymbol{e}_{ij}\right) \boldsymbol{e}_{ij} \ , \\ \boldsymbol{F}_{ij}^{R} &= \sigma w^{R}(r_{ij}) \xi_{ij} \boldsymbol{e}_{ij} \ , \end{aligned} \tag{2.11}$$

where $r_{ij} = |\boldsymbol{r}_i - \boldsymbol{r}_j|$, $\boldsymbol{e}_{ij} = (\boldsymbol{r}_i - \boldsymbol{r}_j)/|\boldsymbol{r}_i - \boldsymbol{r}_j|$, $\boldsymbol{v}_{ij} = \dot{\boldsymbol{r}}_i - \dot{\boldsymbol{r}}_j$ and w^C, w^D, w^R are weight functions, while $\xi_{ij} = \xi_{ji}$ are white noise processes. The coefficients a, γ and σ determine the magnitude of each interaction. A fluctuation-dissipation relation exists between the dissipative and random forces to ensure the existence of an equilibrium condition at temperature T [64]

$$\sigma_{ij} = \sqrt{2 k_B T \gamma_{ij}} \ , \tag{2.12}$$

$$w^{D} = \left(w^{R}\right)^2 \ . \tag{2.13}$$

The shape of the conservative force is specified by the weight function w^C, which in principle could have any form. The same is true for the dissipative weight function w^D, the random force being determined by the fluctuation-dissipation relation eq. (2.13). A common choice [65] which is adopted in the simulations reported in this thesis is

$$w^{C} = w^{R} = \left(w^{D}\right)^{\frac{1}{2}} = \begin{cases} 1 - \frac{r_{ij}}{r_c} & \text{if } r_{ij} < r_c \ , \\ 0 & \text{if } r_{ij} > r_c \ , \end{cases} \tag{2.14}$$

with r_c the cut-off radius of the inter-particle interaction. The remaining parameter γ can be used to calibrate the viscosity. In particular, setting $\gamma =$

1200 leads to a (dimensionless) viscosity of 65.5, as estimated by measuring the mean velocity of a Poiseuille profile [66].

The original DPD model was developed to study the rheology of colloidal suspensions [63, 67], but in the last two decades it has been expanded in many different ways in order to simulate increasingly complex systems [68, 69, 70, 71, 72, 73]. Physical systems studied with DPD or derived methods include blood [74, 75], polymers [76], biomolecules [77], biological membranes [78], and droplets [79]. DPD simulations including electrostatic interactions have also been performed, either considering DPD particles with fixed charge [80, 81] or charged polyelectrolytes [82, 83]. A different approach can be used considering the concentrations of ionic species as additional variables associated to each DPD particle, modelling the fluxes of concentration between them [73].

In part III, a mesoscale model based on DPD is presented. The model is able to simulate the electrohydrodynamic phenomena taking place in nanofluidic systems, representing the dissolved ions by adding two degrees of freedom for each particle. The model is tested performing simulations of planar electroosmotic flow, finding an excellent agreement with analytical solutions.

Part II

Particle dynamics under confinement

In this part, the Langevin equation for the translational and rotational Brownian dynamics of a rigid particle under confinement is derived. The orientation of the rigid particle is expressed using the quaternion formulation. To take into account the effect of confining boundaries, the Langevin equation must include a nonuniform mobility as an input. As a case of study, the mobility of a spherical particle in a cylindrical channel has been computed using Dissipative Particle Dynamics simulations. The rigid boundaries of the simulated system (the cylinder and the sphere) have been modelled and calibrated to reproduce the non-slip boundary conditions. Even for such a simple system, the computed mobility matrix is non diagonal, meaning that translations and rotations are coupled. The mobility field has then been used to perform Brownian Dynamics simulations, computing the translational and rotational diffusion matrices as a function of the confinement, i.e. the cylinder radius with respect to the particle radius. For the translational part,

the results are in agreement both with previous numerical results and with experimental evidence in reporting a reduction in diffusion for higher confinements. The rotational diffusion is also found to decrease for more confined systems. The effect of external forces on the diffusion and on the distribution of the particle has also been explored.

Chapter 3

Rigid body Brownian motion

In this chapter, a Langevin equation for the Brownian dynamics of a rigid body is derived with a procedure which is analogous to the one shown in Sec 2.1 and which requires the formulation of the rigid body orientation in terms of quaternions. The quaternion properties needed to do this are reported in the first section of the present chapter.

3.1 Quaternions and Rotations

A quaternion $\boldsymbol{q}$ consists of a scalar part q_0 and a 3-D vector part $\vec{q}$, [84],

$$\boldsymbol{q} = \begin{pmatrix} q_0 \\ \vec{q} \end{pmatrix} . \tag{3.1}$$

The product between two quaternions $\boldsymbol{p}$ and $\boldsymbol{q}$ is non commutative and can be written as [85]

$$\boldsymbol{qp} = \begin{pmatrix} p_0 q_0 - \vec{p} \cdot \vec{q} \\ p_0 \vec{q} + q_0 \vec{p} + \vec{q} \times \vec{p} \end{pmatrix} , \tag{3.2}$$

where $\vec{p} \times \vec{q}$ is the vector product. The conjugated quaternion is obtained changing sign to the vector part of $\boldsymbol{q}$

$$\boldsymbol{q}^* = \begin{pmatrix} q_0 \\ -\vec{q} \end{pmatrix} , \tag{3.3}$$

such that

$$\boldsymbol{q}\boldsymbol{q}^* = \boldsymbol{q}^*\boldsymbol{q} = \begin{pmatrix} \|\boldsymbol{q}\|^2 \\ \vec{0} \end{pmatrix} , \tag{3.4}$$

where $\|\boldsymbol{q}\| = \sqrt{q_0^2 + q_1^2 + q_2^2 + q_3^2}$ is the quaternion norm with q_1, q_2 and q_3 the components of vector part. It follows that the complex conjugate of a quaternion product is the product of the conjugate quaternions taken with inverted order

$$(\boldsymbol{q}\boldsymbol{p})^* = \boldsymbol{p}^*\boldsymbol{q}^* . \tag{3.5}$$

Given a quaternion $\boldsymbol{q}$, it is sometimes convenient to consider suitable matrices

$$\mathbf{Q}_l = \begin{pmatrix} q_0 & -q_1 & -q_2 & -q_3 \\ q_1 & q_0 & -q_3 & q_2 \\ q_2 & q_3 & q_0 & -q_1 \\ q_3 & -q_2 & q_1 & q_0 \end{pmatrix} , \ \mathbf{Q}_r = \begin{pmatrix} q_0 & -q_1 & -q_2 & -q_3 \\ q_1 & q_0 & q_3 & -q_2 \\ q_2 & -q_3 & q_0 & q_1 \\ q_3 & q_2 & -q_1 & q_0 \end{pmatrix} , \tag{3.6}$$

to express the left and right products of $\boldsymbol{q}$ and $\boldsymbol{p}$ as

$$\begin{aligned} \boldsymbol{q}\boldsymbol{p} &= \boldsymbol{Q}_l\boldsymbol{p} , \\ \boldsymbol{p}\boldsymbol{q} &= \boldsymbol{Q}_r\boldsymbol{p} . \end{aligned} \tag{3.7}$$

For unit norm quaternions it is easily shown that $\boldsymbol{q}^*\boldsymbol{q}\boldsymbol{p} = \boldsymbol{Q}_l^T\boldsymbol{Q}_l\boldsymbol{p} = \boldsymbol{p}$, and as a consequence

$$\boldsymbol{Q}_l^{-1} = \boldsymbol{Q}_l^T , \tag{3.8}$$

i.e. the matrices $\boldsymbol{Q}_l$ and $\boldsymbol{Q}_r$ are orthogonal. In the following $\boldsymbol{q}$ will denote a unit quaternion, i.e. a quaternion with unit norm. Unit quaternions are central to rigid body kinematics since they represent rotations of angle ϕ about a generic axis specified by the director $\hat{u}$,

$$\boldsymbol{q} = \boldsymbol{q}(\phi, \hat{u}) = \begin{pmatrix} \cos\left(\frac{\phi}{2}\right) \\ \hat{u}\sin\left(\frac{\phi}{2}\right) \end{pmatrix} . \tag{3.9}$$

The rotation by ϕ about the axis $\hat{u}$ of a 3-D vector $\vec{v}'$ is then expressed as

$$\boldsymbol{v} = \boldsymbol{q}\boldsymbol{v}'\boldsymbol{q}^* . \tag{3.10}$$

It should be stressed that the product implied by this equation involves quaternions as defined in eq. (3.2). In other words, the representation of the ordinary vector $\vec{v}'$ as the quaternion $\boldsymbol{v}'$ is needed. This is given by $\boldsymbol{v}' = (0, \vec{v}')^T$, i.e. the quaternion corresponding to an ordinary vector has zero scalar part. Using (3.2) one obtains

$$\begin{aligned} \boldsymbol{v} = \begin{pmatrix} -\vec{v}'\cdot\vec{q} \\ q_0\vec{v}' + \vec{q}\times\vec{v}' \end{pmatrix} \boldsymbol{q}^* = \begin{pmatrix} -q_0\vec{v}'\cdot\vec{q} + q_0\vec{q}\cdot\vec{v}' + \vec{q}\times\vec{v}'\cdot\vec{q} \\ q_0^2\vec{v}' + q_0\vec{q}\times\vec{v}' + \vec{v}'\cdot\vec{q}\vec{q} - (q_0\vec{v}' + \vec{q}\times\vec{v}')\times\vec{q} \end{pmatrix} = \\ = \begin{pmatrix} 0 \\ q_0^2\vec{v}' + 2q_0\vec{q}\times\vec{v}' + 2(\vec{v}'\cdot\vec{q})\vec{q} - (\vec{q}\cdot\vec{q})\vec{v}' \end{pmatrix} , \end{aligned} \tag{3.11}$$

showing that the scalar part of the quaternion $\boldsymbol{v}$ is zero, i.e. it represents the ordinary vector $\vec{v}$. Using (3.9) yields

$$\begin{aligned} \vec{v} = \left[\cos^2\left(\frac{\phi}{2}\right) - \sin^2\left(\frac{\phi}{2}\right)\right]\vec{v}' + 2\cos\left(\frac{\phi}{2}\right)\sin\left(\frac{\phi}{2}\right)\vec{u}\times\vec{v}' + 2\vec{v}'\cdot\vec{u}\sin^2\left(\frac{\phi}{2}\right)\vec{u} = \\ = \cos(\phi)\,\vec{v}' + \sin(\phi)\vec{u}\times\vec{v}' + (1-\cos\phi)\vec{v}'\cdot\vec{u}\vec{u} , \end{aligned} \tag{3.12}$$

which is the Rodrigues formula for the rotation of the vector $\vec{v}'$ by the angle ϕ about the axis $\vec{u}$. Equation (3.10) can also be written in matrix notation

$$\boldsymbol{v} = \boldsymbol{Q}_r^T \boldsymbol{Q}_l \boldsymbol{v}' \ , \tag{3.13}$$

or

$$\vec{v} = \boldsymbol{B}(\boldsymbol{q})\vec{v}' \ , \tag{3.14}$$

where $\boldsymbol{B}(\boldsymbol{q})$ is the rotation matrix written in terms of quaternions which turns out to be the matrix corresponding to the lowest right 3×3 minor the original 4×4 matrix $\boldsymbol{Q}_r^T \boldsymbol{Q}_l$.

In quaternion notation, the rotation of a previously rotated vector $\boldsymbol{v}_1 = \boldsymbol{q}_1 \boldsymbol{v}' \boldsymbol{q}_1^*$ is $\boldsymbol{v}_2 = \boldsymbol{q}_2 \boldsymbol{q}_1 \boldsymbol{v}' \boldsymbol{q}_1^* \boldsymbol{q}_2^*$, i.e. the composition of two rotations corresponds to multiplication of two unit quaternions. By straightforward generalization, the rotational trajectory of a rigid body can then be represented as

$$\boldsymbol{q}(t + \Delta t) = \boldsymbol{q}(|\vec{\omega}|\Delta t, \vec{\omega}/|\vec{\omega}|)\boldsymbol{q}(t) \ , \tag{3.15}$$

where $\vec{\omega}\,\Delta t$ is the elementary rotation taking place in the (elementary) time interval Δt when the angular velocity of the rigid body is $\vec{\omega}$. Equation (3.15) can be rewritten in matrix notation,

$$\boldsymbol{q}(t + \Delta t) = \boldsymbol{Q}_l(|\vec{\omega}|\Delta t, \vec{\omega}/|\vec{\omega}|)\boldsymbol{q}(t) := \boldsymbol{Q}_{rot}(\vec{\omega}, \Delta t)\boldsymbol{q}(t) \ , \tag{3.16}$$

where $\boldsymbol{Q}_{rot}$ is $4{\times}4$ matrix equivalent to the the left multiplication $\boldsymbol{q}(|\vec{\omega}|\Delta t, \vec{\omega}/|\vec{\omega}|)$, eq. (3.6).

Since $\boldsymbol{q}$ is a unit quaternion at every time, the scalar part of $\boldsymbol{q}\dot{\boldsymbol{q}}^*$ is zero,

$$\boldsymbol{q}\dot{\boldsymbol{q}}^* = \begin{pmatrix} q_0\dot{q}_0 + \vec{q}\cdot\dot{\vec{q}} \\ \dot{q}_0\vec{q} - q_0\dot{\vec{q}} + \dot{\vec{q}}\times\vec{q} \end{pmatrix} = \begin{pmatrix} 0 \\ \dot{q}_0\vec{q} - q_0\dot{\vec{q}} + \dot{\vec{q}}\times\vec{q} \end{pmatrix} \ , \tag{3.17}$$

i.e. it corresponds to a vector. The differential equation describing the rotation of a vector may then be obtained as follows. After differentiating Eq. (3.10),

$$\dot{\boldsymbol{v}} = \dot{\boldsymbol{q}}\boldsymbol{v}'\boldsymbol{q}^* + \boldsymbol{q}\boldsymbol{v}'\dot{\boldsymbol{q}}^* \ , \tag{3.18}$$

left and right multiplication by $\boldsymbol{q}^*$ and $\boldsymbol{q}$, respectively, yield

$$\boldsymbol{q}^*\dot{\boldsymbol{v}}\boldsymbol{q} = \boldsymbol{q}^*\dot{\boldsymbol{q}}\boldsymbol{v}' + \boldsymbol{v}'\dot{\boldsymbol{q}}^*\boldsymbol{q} \ , \tag{3.19}$$

which can be rearranged as

$$\boldsymbol{q}^*\dot{\boldsymbol{v}}\boldsymbol{q} = \boldsymbol{q}^*\dot{\boldsymbol{q}}\boldsymbol{v}' - \boldsymbol{v}'\boldsymbol{q}^*\dot{\boldsymbol{q}} \ . \tag{3.20}$$

after realizing that $d(\boldsymbol{q}^*\boldsymbol{q})/dt = \dot{\boldsymbol{q}}^*\boldsymbol{q} + \boldsymbol{q}^*\dot{\boldsymbol{q}} = 0$. As quaternion representation of vectors, the scalar part of both $\boldsymbol{q}^*\dot{\boldsymbol{q}}$, Eq. (3.17), and $\boldsymbol{v}'$ is zero. The scalar part of $\dot{\boldsymbol{v}}$ is also zero, since, according to Eq. (3.11), $\boldsymbol{v}$ also represents a vector (i.e. its scalar part is zero for all times, implying that the scalar part of its time derivative vanishes identically). This allows for inverting the order in the multiplication of the second term at the left hand side of eq. (3.20), obtaining $\boldsymbol{q}^*\dot{\boldsymbol{q}}\boldsymbol{v}' = -\boldsymbol{v}'\boldsymbol{q}^*\dot{\boldsymbol{q}}$, that gives

$$\boldsymbol{q}^*\dot{\boldsymbol{v}}\boldsymbol{q} = 2\boldsymbol{q}^*\dot{\boldsymbol{q}}\boldsymbol{v}' \ . \tag{3.21}$$

If, in Eq. (3.10), $\boldsymbol{v}'$ represents a position vector in a body fixed reference frame, rotating with respect to an external (fixed) frame, the left side $\boldsymbol{v}$ is the position in the fixed frame and $\dot{\boldsymbol{v}}$ the corresponding velocity. Hence $2\boldsymbol{q}^*\dot{\boldsymbol{q}}$ corresponds to the angular velocity vector (zero scalar part) written in the body reference frame

$$\boldsymbol{\omega}' = 2\boldsymbol{q}^*\dot{\boldsymbol{q}} \ . \tag{3.22}$$

The angular velocity in the fixed reference frame (applying Eq. (3.10)) is then

$$\boldsymbol{\omega} = 2\dot{\boldsymbol{q}}\boldsymbol{q}^* \ . \tag{3.23}$$

In matrix notation Eq. (3.23) is

$$\boldsymbol{\omega} = \begin{pmatrix} 0 \\ \vec{\omega} \end{pmatrix} = 2\boldsymbol{Q}_r^T \dot{\boldsymbol{q}} \ , \tag{3.24}$$

which, after inversion, reads

$$\dot{\boldsymbol{q}} = \frac{1}{2}\boldsymbol{Q}_r\boldsymbol{\omega} = \frac{1}{2}\bar{\boldsymbol{Q}}_r\vec{\omega} \ , \tag{3.25}$$

where the condition of having zero scalar part, $\omega_0 = 0$, has been used to define the reduced 4×3 matrix $\bar{\boldsymbol{Q}}_r$

$$\bar{\boldsymbol{Q}}_r = \begin{pmatrix} -q_1 & -q_2 & -q_3 \\ q_0 & q_3 & -q_2 \\ -q_3 & q_0 & q_1 \\ q_2 & -q_1 & q_0 \end{pmatrix} \ . \tag{3.26}$$

The expression for the angular velocity can now be exploited in the work theorem to obtain the appropriate form of a conservative torque $\vec{t}$ from the potential energy $U(\boldsymbol{q})$ given as a function of the rigid body attitude in terms of the unit quaternion $\boldsymbol{q}$. For such body, the following relation must hold

$$\vec{\omega} \cdot \vec{t} = -\dot{\boldsymbol{q}} \cdot \boldsymbol{S}_q \boldsymbol{\nabla}_{\boldsymbol{q}}[U(\boldsymbol{q})] = -\frac{1}{2}\boldsymbol{Q}_r\boldsymbol{\omega} \cdot \boldsymbol{S}_q \boldsymbol{\nabla}_{\boldsymbol{q}} U \ , \tag{3.27}$$

where the $\boldsymbol{\nabla}_{\boldsymbol{q}}$ denotes the quaternion constructed with the partial derivatives with respect to the four quaternion components and the projector $\boldsymbol{S}_q = \boldsymbol{I} - \boldsymbol{q} \otimes \boldsymbol{q}$ takes into account that the quaternion dynamics is restricted to

the manifold of unit quaternions, i.e. $\|\boldsymbol{q}\| = 1$. Since equation (3.27) holds for arbitrary $\boldsymbol{\omega}$, the torque must be

$$\boldsymbol{t} = \begin{pmatrix} 0 \\ \vec{t} \end{pmatrix} = -\frac{1}{2}\boldsymbol{Q}_r^T \boldsymbol{S}_q \boldsymbol{\nabla} U \ . \tag{3.28}$$

The projection matrix is necessary to ensure that, given any potential energy U, the resulting torque quaternion has zero scalar part. In fact, the product $\boldsymbol{Q}_r^T \boldsymbol{S}_q$ gives

$$\boldsymbol{Q}_r^T \boldsymbol{S}_q = \begin{pmatrix} 0 & 0 & 0 & 0 \\ & & \bar{\boldsymbol{Q}}_r^T & \end{pmatrix} \ . \tag{3.29}$$

A straightforward consequence is

$$\begin{aligned} \bar{\boldsymbol{Q}}_r^T \boldsymbol{S}_q &= \bar{\boldsymbol{Q}}_r^T \ , \\ \boldsymbol{S}_q \bar{\boldsymbol{Q}}_r &= \bar{\boldsymbol{Q}}_r \ , \end{aligned} \tag{3.30}$$

and eq. (3.28) can be expressed as

$$\vec{t} = -\frac{1}{2}\bar{\boldsymbol{Q}}_r^T \boldsymbol{\nabla} U \ . \tag{3.31}$$

The interested reader can find an alternative discussion on quaternion formulation of rigid body Hamiltonian dynamics in [86, 87].

3.2 Rigid body Langevin equation

Using the quaternion formulation, the configuration $\mathbf{x}$ is a 7-D vector including $\vec{x}$, the position of the particle center and the four components of the orientation quaternion $\boldsymbol{q}$

$$\boldsymbol{x} = \begin{pmatrix} \vec{x} \\ \boldsymbol{q} \end{pmatrix} \ . \tag{3.32}$$

The generalized velocity $\boldsymbol{v}$ is a 6-D vector

$$\boldsymbol{v} = \begin{pmatrix} \vec{v} \\ \vec{\omega} \end{pmatrix} . \tag{3.33}$$

The vectors $\boldsymbol{x}$ and $\boldsymbol{v}$ are related via a 7×6 kinematic matrix $\boldsymbol{\Phi}$

$$\dot{\boldsymbol{x}} = \boldsymbol{\Phi}\boldsymbol{v} , \tag{3.34}$$

with

$$\boldsymbol{\Phi} = \begin{pmatrix} \boldsymbol{I} & \boldsymbol{0} \\ \boldsymbol{0} & \frac{1}{2}\bar{\boldsymbol{Q}}_r , \end{pmatrix} . \tag{3.35}$$

where the matrix $\bar{\boldsymbol{Q}}_r$ is defined in Sec. 3.1, eq. (3.26).

The following property of the matrix $\boldsymbol{\Phi}$ will be needed to derive the Langevin equation. For any 6×6 matrix A, we have

$$\boldsymbol{\nabla} \cdot \left(\boldsymbol{\Phi}\boldsymbol{A}\boldsymbol{\Phi}^T\right) = \frac{\partial}{\partial x_j}(\Phi_{ik}A_{kl}\Phi_{jl}) = \frac{\partial \Phi_{ik}}{\partial x_j}A_{kl}\Phi_{jl} + \Phi_{ik}\frac{\partial A_{kl}}{\partial x_j}\Phi_{jl} + \Phi_{ik}A_{kl}\frac{\partial \Phi_{jl}}{\partial x_j} , \tag{3.36}$$

where there is an implied summation over repeated indexes. Given the expression of $\boldsymbol{\Phi}$, the third term of the right hand side of eq. (3.36) is zero and, for a symmetric matrix, the first term yields $-1/4\boldsymbol{x}_i^{(q)} \sum_{j=3}^{6} A_{jj}$, where $\boldsymbol{x}^{(q)} = (0, 0, 0, q_0, q_1, q_2, q_3)^T$ is the quaternion part of the configuration vector. The final result is

$$\boldsymbol{\nabla} \cdot \left(\boldsymbol{\Phi}\boldsymbol{A}\boldsymbol{\Phi}^T\right) = \boldsymbol{\Phi}\boldsymbol{\nabla}\boldsymbol{A} : \boldsymbol{\Phi}^T - \frac{1}{4}Tr(\boldsymbol{A}_{\boldsymbol{3\times 3}})\boldsymbol{x}^{(q)} , \tag{3.37}$$

where $\boldsymbol{A}_{\boldsymbol{3\times 3}}$ is the lower right 3×3 submatrix of $\boldsymbol{A}$.

The generalized velocity of a rigid body can be modelled, in the overdamped Langevin approach, as composed by a deterministic drift term $\boldsymbol{u}$

and a stochastic term $\boldsymbol{G\xi}$, linearly dependent on the 6-D vector of white noise processes $\boldsymbol{\xi}$

$$\boldsymbol{v}\left(t\right)=\boldsymbol{u}\left(\boldsymbol{x}\right)+\boldsymbol{G}\left(\boldsymbol{x}\right)\boldsymbol{\xi}\left(t\right)\quad . \tag{3.38}$$

Using the kinematic relation (3.35) a Langevin equation for the configuration $\boldsymbol{x}$ is obtained

$$\dot{\boldsymbol{x}}\left(t\right)=\tilde{\boldsymbol{u}}\left(\boldsymbol{x}\right)+\tilde{\boldsymbol{G}}\left(\mathbf{x}\right)\boldsymbol{\xi}\left(t\right)\quad , \tag{3.39}$$

where $\tilde{\boldsymbol{u}}$ and $\tilde{\boldsymbol{G}}$ are respectively a 7-D vector and a 7×6 matrix

$$\begin{aligned}\tilde{\boldsymbol{u}}&=\boldsymbol{\Phi u}\ ,\\ \tilde{\boldsymbol{G}}&=\boldsymbol{\Phi G}\ .\end{aligned} \tag{3.40}$$

Integrating $\dot{\boldsymbol{x}}$ over a time interval Δt, starting from a position $\boldsymbol{x}_0=\boldsymbol{x}(0)$ gives

$$\Delta\boldsymbol{x}(\boldsymbol{x}_0,\Delta t)=\boldsymbol{x}(\Delta t)-\boldsymbol{x}_0=\int_0^{\Delta t}\dot{\boldsymbol{x}}(t)\,\mathrm{d}t=\tilde{\boldsymbol{u}}(\boldsymbol{x}_0)\Delta t+\tilde{\boldsymbol{G}}(\boldsymbol{x}_0)\boldsymbol{b}\sqrt{\Delta t}+O(\Delta t)\ , \tag{3.41}$$

where $\boldsymbol{b}$ is a vector of independent Gaussian variables with zero mean and unit variance, and Itô's convention has been adopted. To the required order of accuracy we have

$$\Delta\boldsymbol{x}(\boldsymbol{x}_0,\Delta t)\otimes\Delta\boldsymbol{x}(\boldsymbol{x}_0,\Delta t)=\tilde{\boldsymbol{G}}(\boldsymbol{x}_0)\boldsymbol{b}\otimes\tilde{\boldsymbol{G}}(\boldsymbol{x}_0)\boldsymbol{b}\Delta t+o(\Delta t)\ . \tag{3.42}$$

The expectation value of eqs. (3.41) and (3.42), mean and covariance matrix respectively, are

$$\left\langle\Delta\boldsymbol{x}\right\rangle\left(\boldsymbol{x}_0,\Delta t\right)=\tilde{\boldsymbol{u}}(\boldsymbol{x}_0)\Delta t+o(\Delta t)\ , \tag{3.43}$$

$$\left\langle\Delta\boldsymbol{x}\otimes\Delta\boldsymbol{x}\right\rangle\left(\boldsymbol{x}_0,\Delta t\right)=\tilde{\boldsymbol{G}}(\boldsymbol{x}_0)\tilde{\boldsymbol{G}}^{T}\left(\boldsymbol{x}_0\right)\Delta t+o(\Delta t)\ . \tag{3.44}$$

The pdf of the rigid-body configuration, $P(\boldsymbol{x},t)$, obeys (a straightforward consequence of) Chapman-Kolmogorov equation

$$P(\boldsymbol{x},t+\Delta t)=\int\limits_{\Omega}P(\boldsymbol{x}',t)P(\boldsymbol{x},t+\Delta t|\boldsymbol{x}',t)\,\mathrm{d}\boldsymbol{x}'\ , \tag{3.45}$$

where Ω is the rigid-body configuration space and $P(\boldsymbol{x},t+\Delta t|\boldsymbol{x}',t)$ is the relevant transition probability, namely the conditional pdf that the ridig-body will be found in state $\boldsymbol{x}$ given it was in state $\boldsymbol{x}'$ at the earlier instant,

$$P(\boldsymbol{x},t+\Delta t|\boldsymbol{x}',t)=\langle\delta\left[\boldsymbol{x}-\boldsymbol{x}'-\Delta\boldsymbol{x}(\boldsymbol{x}',\Delta t)\right]\rangle\ . \tag{3.46}$$

Expanding the Dirac delta function around the point $(\boldsymbol{x}-\boldsymbol{x}')$ and taking care of the constraint $\|\boldsymbol{q}\|=1$, one obtains

$$\begin{aligned}P(\boldsymbol{x},t+\Delta t|\boldsymbol{x}',t)&=\delta(\boldsymbol{x}-\boldsymbol{x}')-\boldsymbol{S}\boldsymbol{\nabla}\delta(\boldsymbol{x}-\boldsymbol{x}')\cdot\langle\Delta\boldsymbol{x}(\boldsymbol{x}',\Delta t)\rangle+\\&+\frac{1}{2}\boldsymbol{S}\boldsymbol{\nabla}\otimes\boldsymbol{S}\boldsymbol{\nabla}\delta(\boldsymbol{x}-\boldsymbol{x}'):\langle\Delta\boldsymbol{x}(\boldsymbol{x}',\Delta t)\otimes\Delta\boldsymbol{x}(\boldsymbol{x}',\Delta t)\rangle+o(\Delta t)\ .\end{aligned} \tag{3.47}$$

Here $\boldsymbol{S}$ is a 7×7 matrix

$$\boldsymbol{S}=\begin{pmatrix}\boldsymbol{I}&0\\0&\boldsymbol{S}_q\end{pmatrix}\ . \tag{3.48}$$

Using eqs. (3.43) and (3.44) and substituting eq. (3.47) into eq. (3.45) leads to

$$\begin{aligned}P(\boldsymbol{x},t+\Delta t)=P(\boldsymbol{x},t)-\boldsymbol{\nabla}\cdot(\boldsymbol{S}\tilde{\boldsymbol{u}}P(\boldsymbol{x},t))\,\Delta t+\frac{1}{2}\boldsymbol{\nabla}\otimes\boldsymbol{\nabla}:\left(\boldsymbol{S}\tilde{\boldsymbol{G}}\tilde{\boldsymbol{G}}^T\boldsymbol{S}P(\boldsymbol{x},t)\right)\Delta t+\\+\frac{1}{2}\boldsymbol{\nabla}\cdot\left(\boldsymbol{S}\tilde{\boldsymbol{G}}\tilde{\boldsymbol{G}}^T\boldsymbol{\nabla}\cdot\boldsymbol{S}P(\boldsymbol{x},t)\right)\Delta t+o(\Delta t)\ .\end{aligned} \tag{3.49}$$

From eq. (3.30) it can be seen that $\boldsymbol{S}\boldsymbol{\Phi}=\boldsymbol{\Phi}$ and that $\boldsymbol{\Phi}^T\boldsymbol{S}=\boldsymbol{\Phi}^T$. Using these properties and the fact that $\boldsymbol{\Phi}^T\boldsymbol{\nabla}\cdot\boldsymbol{S}=0$,

$$P(\boldsymbol{x},t+\Delta t)=P(\boldsymbol{x},t)-\boldsymbol{\nabla}\cdot(\tilde{\boldsymbol{u}}P(\boldsymbol{x},t))\,\Delta t+\frac{1}{2}\boldsymbol{\nabla}\otimes\boldsymbol{\nabla}:\left(\tilde{\boldsymbol{G}}\tilde{\boldsymbol{G}}^TP(\boldsymbol{x},t)\right)\Delta t+o(\Delta t)\ . \tag{3.50}$$

Rearranging the terms and taking the limit for small Δt, the Fokker-Planck equation for the pdf evolution is obtained

$$\frac{\partial P}{\partial t} = \boldsymbol{\nabla} \cdot \left[\left(-\tilde{\boldsymbol{u}} + \frac{1}{2} \boldsymbol{\nabla} \cdot \left(\tilde{\boldsymbol{G}} \tilde{\boldsymbol{G}}^T \right) + \frac{1}{2} \tilde{\boldsymbol{G}} \tilde{\boldsymbol{G}}^T \boldsymbol{\nabla} \right) P \right] . \tag{3.51}$$

At the equilibrium, the pdf must satisfy

$$P_{eq} = \frac{1}{Z} e^{-\beta U} , \tag{3.52}$$

where Z is the partition function. Substituting eq. (3.52) into eq. (3.51) leads to

$$\boldsymbol{\nabla} \cdot \left[-\tilde{\boldsymbol{u}} + \frac{1}{2} \boldsymbol{\nabla} \cdot \left(\tilde{\boldsymbol{G}} \tilde{\boldsymbol{G}}^{\boldsymbol{T}} \right) + \frac{\beta}{2} \tilde{\boldsymbol{G}} \tilde{\boldsymbol{G}}^T \boldsymbol{\nabla} U \right] = 0 . \tag{3.53}$$

A way to identically satisfy the above condition is assuming that the drift term $\tilde{\boldsymbol{u}}$ consists of the sum of two terms

$$\tilde{\boldsymbol{u}} = \boldsymbol{\Phi} \boldsymbol{M} \boldsymbol{f} + \tilde{\boldsymbol{u}}' = -\boldsymbol{\Phi} \boldsymbol{M} \boldsymbol{\Phi}^T \boldsymbol{S} \boldsymbol{\nabla} U + \boldsymbol{u}' = \tilde{\boldsymbol{M}} \boldsymbol{\nabla} U + \tilde{\boldsymbol{u}}' , \tag{3.54}$$

where $\tilde{\boldsymbol{M}} = \boldsymbol{\Phi} \boldsymbol{M} \boldsymbol{\Phi}^T$. Inserting eq. (3.54) into eq. (3.51) and imposing the equilibrium condition, eq. (3.52) it can be seen that eq. (3.53) is satisfied for any possible U if two conditions are met. The first condition is associated to the first term in (3.54). It leads to the so-called fluctuation-dissipation relation

$$\boldsymbol{M} = \frac{\beta}{2} \boldsymbol{G} \boldsymbol{G}^T . \tag{3.55}$$

The second condition is associated to the second term in eq. (3.54), and gives reason for the assumed additional drift $\boldsymbol{u}'$

$$\tilde{\boldsymbol{u}}' = \frac{1}{2} \boldsymbol{\nabla} \cdot \left(\tilde{\boldsymbol{G}} \tilde{\boldsymbol{G}}^T \right) = \frac{1}{\beta} \boldsymbol{\nabla} \cdot \tilde{\boldsymbol{M}} . \tag{3.56}$$

The evolution equation for the configuration vector takes the form also reported in [88][89],

$$\dot{\boldsymbol{x}} = -\tilde{\boldsymbol{M}}\boldsymbol{\nabla}U + \frac{1}{\beta}\boldsymbol{\nabla}\cdot\tilde{\boldsymbol{M}} + \tilde{\boldsymbol{G}}\boldsymbol{\xi}\ . \tag{3.57}$$

The second term on the right hand side of eq. (3.57) can be finally rewritten using eq. (3.37)

$$\dot{\boldsymbol{x}} = -\tilde{\boldsymbol{M}}\boldsymbol{\nabla}U + \frac{1}{\beta}\boldsymbol{\Phi}\boldsymbol{\nabla}\boldsymbol{M} : \boldsymbol{\Phi}^T - \frac{tr(\boldsymbol{M}_r)}{4\beta}\boldsymbol{x}_q + \tilde{\boldsymbol{G}}\boldsymbol{\xi}\ , \tag{3.58}$$

where $\boldsymbol{M}_r$ is the rotational 3×3 submatrix of $\boldsymbol{M}$. A straightforward approach to integrate eq. (3.57) is using the Euler-Maruyama algorithm in the Itô interpretation of the stochastic equation,

$$\Delta\boldsymbol{x} = -\boldsymbol{\Phi}\boldsymbol{M}\boldsymbol{\Phi}^T\boldsymbol{\nabla}U\Delta t + \frac{1}{\beta}\boldsymbol{\Phi}\boldsymbol{\nabla}\boldsymbol{M} : \boldsymbol{\Phi}^T\Delta t - \frac{tr(\boldsymbol{M}_r)}{4\beta}\boldsymbol{x}_q\Delta t + \boldsymbol{\Phi}\boldsymbol{G}\boldsymbol{b}\sqrt{\Delta t} + o(\Delta t)\ . \tag{3.59}$$

In this context, the constant velocity $\boldsymbol{v} = \boldsymbol{\Phi}^T\Delta\boldsymbol{x}/\Delta t$ used to update the configuration is

$$\boldsymbol{v} = -\boldsymbol{M}\boldsymbol{\Phi}^T\boldsymbol{\nabla}U + \frac{1}{\beta}\boldsymbol{\nabla}\boldsymbol{M} : \boldsymbol{\Phi}^T + \frac{1}{\sqrt{\Delta t}}\boldsymbol{G}\boldsymbol{b}\ . \tag{3.60}$$

Eq. (3.60) is used in to integrate Eq. 3.38 via successive rotations which don't affect the norm of the quaternion, as descibed in next section.

3.3 Integration of Rigid Body Langevin Equation

The integration of eq. (3.38) is performed using the Euler-Maruyama like algorithm [90], modified to properly handle the rotational part of the equations.

The implementation of the algorithm is straightforward for what concerns the translational components of $\dot{\boldsymbol{x}}$. As concerning the quaternion components, the procedure is slightly more involved and it worths being explicitly described. The reason of the additional complexity is related to the fact that only unit norm quaternions correctly represent rotations. Indeed, at each step, the locally updated quaternion does not exactly satisfy the constraint $\|q\| = 1$. The direct application of the generic Euler step leads to $\boldsymbol{q}_{new} = \boldsymbol{q}_{old} + d\boldsymbol{q}_{new}$, hence the squared norm of the updated quaternion would be

$$\boldsymbol{q}^*_{new}\boldsymbol{q}_{new} = \left(\boldsymbol{q}^*_{old} + d\boldsymbol{q}^*\right)\left(\boldsymbol{q}_{old} + d\boldsymbol{q}\right) = \boldsymbol{q}^*_{old}\boldsymbol{q}_{old} + \boldsymbol{q}^*_{old}d\boldsymbol{q} + d\boldsymbol{q}^*\boldsymbol{q}_{old} + d\boldsymbol{q}^*d\boldsymbol{q} \tag{3.61}$$

(the reader is referred to Sec 3.1 for issues related to quaternion notation and the relevant inner product). While the first term in the right hand side of eq. (3.61) is the norm of $\boldsymbol{q}_{old}$, and, hence, $\boldsymbol{q}^*_{old}\boldsymbol{q}_{old} = 1$, there is no guarantee that, in general, the remaining terms sum to zero. It follows that a naive implementation of the algorithm would not produce a valid quaternion. To circumvent this difficulty, a sort of projection procedure has been devised. The correct quaternion increment is calculated as $\boldsymbol{q}_{new} = \boldsymbol{Q}(\mathrm{d}\vec{\alpha})\boldsymbol{q}_{old}$, where $\boldsymbol{Q}(\mathrm{d}\vec{\alpha})$, Section 3.1, is the 4×4 rotation matrix that produces the new quaternion (with exactly unit norm) from the old one by applying a rotation of angle $\mathrm{d}\alpha$ about the rotation axis $\mathrm{d}\vec{\alpha}/\mathrm{d}\alpha$. The angular displacement $\mathrm{d}\vec{\alpha}$ is calculated as $\mathrm{d}\vec{\alpha} = \vec{\omega}\mathrm{d}t$. The complete algorithm is:

1. At step τ, the mobility matrix $\boldsymbol{M}^{(\tau)} = \boldsymbol{M}\left(\boldsymbol{x}^{(\tau)}\right)$, its derivatives $\boldsymbol{M}_i^{(\tau)} = \partial\boldsymbol{M}^{(\tau)}/\partial x_i$, the generalized forces $\boldsymbol{f}^{(\tau)} = \boldsymbol{f}\left(\boldsymbol{x}^{(\tau)}\right)$ and the kinematic matrix $\boldsymbol{\Phi}^{(\tau)} = \boldsymbol{\Phi}\left(\boldsymbol{x}^{(\tau)}\right)$ are computed from the known configuration,

$\boldsymbol{x}^{(\tau)} = \left(\vec{x}^{(\tau)}, \boldsymbol{q}^{(\tau)}\right)$.

2. The noise intensity matrix $\boldsymbol{G}^{(\tau)}$ is computed from the mobility $\boldsymbol{M}^{(\tau)}$, eq. (3.55), by Cholesky decomposition.

3. The generalized velocity $\boldsymbol{v}^{(\tau)} = \left(\vec{v}^{(\tau)}, \vec{\omega}^{(\tau)}\right)$ at the current time step $\boldsymbol{v}^{(\tau)}$ is estimated with the Euler-Maruyama like algorithm, see eq. (3.60)

$$\boldsymbol{v}^{(\tau)} = \boldsymbol{M}^{(\tau)}\boldsymbol{f}^{(\tau)} + \boldsymbol{M}_i^{(\tau)}\boldsymbol{\phi}_i^{(\tau)} + \frac{1}{\sqrt{\Delta t}}\boldsymbol{G}^{(\tau)}\boldsymbol{b}\,, \tag{3.62}$$

where a summation over the repeated index is implied and the 6-D vector $\boldsymbol{\phi}_i^{(\tau)}$ corresponds to the i^{th} row of matrix $\boldsymbol{\Phi}^{(\tau)}$. The random vector $\boldsymbol{b}$ if formed with 6 independent, normally-distributed random numbers with zero mean and unitary variance.

4. Finally, the configuration at the time step $\tau + 1$ is computed as

$$\boldsymbol{x}^{(\tau+1)} = \begin{pmatrix} \vec{x}^{(\tau)} + \vec{v}^{(\tau)}\Delta t \\ \boldsymbol{Q}(\vec{\omega}^{(\tau)}\Delta t)\boldsymbol{q}^{(\tau)} \end{pmatrix}\,. \tag{3.63}$$

Chapter 4

Mobility of a confined sphere

The algorithm described in Section 3.3 accounts for a space dependent mobility, which means that hydrodynamic effects due to confinement have to be included in the simulation via the mobility field $\boldsymbol{M}$. Since $\boldsymbol{M}$ is a function of the position and the orientation of the particle it should be calculated at each time step. This approach would be computationally too demanding. To reduce the computational cost, the mobility field can be pre-calculated for different configurations to obtain at each time the mobility via interpolation. This look-up table can be evaluated using any hydrodynamic solver, here DPD was used.

4.1 Rigid Boundary Modelling in DPD

Rigid boundaries need to be included in the DPD modeling to deal with confined systems. Enforcing the proper boundary conditions in the DPD framework is not entirely trivial [91]. Concerning wall impermeability, the

natural approach would be adopting reflecting boundary conditions [92]. Alternatively, the wall can be modeled with fixed DPD particles, interacting with the fluid through the same force system used for fluid-fluid interactions by suitably adapting the force parameters. In this case, wall impermeability is controlled by the repulsive, conservative component of the force system. Since the force is everywhere smooth (no divergence at small distance), impermeability cannot be strictly guaranteed by this approach since the stochastic force could sample extremely intense, though highly improbable, events. Impermeability of a DPD wall can in principle be improved by increasing the repulsion parameter or by selecting a higher wall particle density. In both cases significant density wall layering may be induced [93], an undesired feature since the properties of a DPD fluid are strongly density dependent. Concerning the no-slip boundary conditions, several approaches are available, including explicit modeling of particle-wall interactions [94], introduction of non-central forces [95], or addition of an extra variable to progressively intensify the wall interaction depending on wall-particle distance [96]. All these methods, both for the normal and the tangent boundary condition, require a substantial modification of the original DPD scheme. Here, the original DPD scheme is retained tuning the wall properties by acting on the wall particles spatial distribution and the fluid-wall interaction parameters: As it will be shown, this choice allows to satisfy impermeability and no-slip condition to the desired accuracy even for curved moving boundaries.

The wall is modelled as a layer of dimensionless width 2 composed by DPD frozen particles. The wall-normal particles distribution varies according to

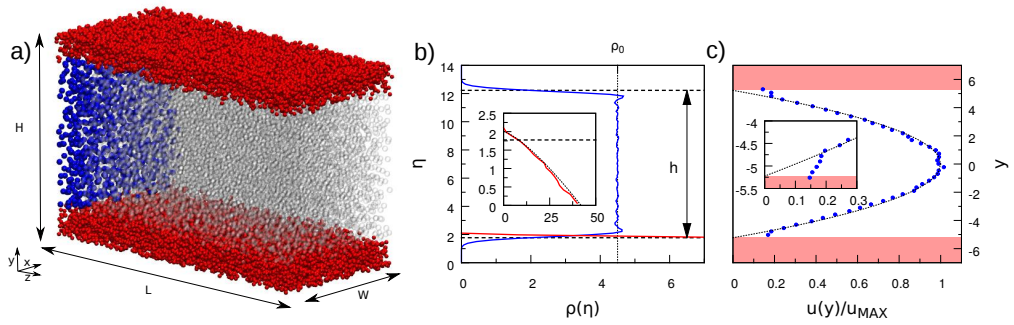

Figure 4.1: Poiseuille flow simulation set-up and wall model. a) The planar channel is made using wall particles (red spheres) distributed following eq. (4.1) with parameters $\rho_w^{(0)} = 24$, $a_{wf} = 5$ and $\alpha = 0.75$. A force parallel to the $\boldsymbol{z}$ direction is applied to each fluid particle in a slab parallel Oxy plane. Those particles are represented as blue spheres, while the remaining fluid particles as gray transparent spheres. b) Density profile of the bottom wall particles (red) and of the fluid particles (blue), as a function of the distance from the lower boundary of the simulation box, η. The horizontal dashed lines represent the quote of the hydrodynamic boundaries, and the vertical dashed line represents the bulk fluid density ρ_0. In the inset, a zoom of the density profile of the wall particles is reported. Again, the horizontal dashed line is the quote of the hydrodynamic boundary, while the dotted represents the density profile of eq. (4.1). c) Velocity profile ($\bar{g} = 0.06$, $\gamma_{wf} = 2 \cdot 10^4$) of the fluid as a function of y. The red areas are the regions below and above the hydrodynamic boundaries while the dashed profile is the analytic prediction (Poiseuille flow) for no-slip walls. It is apparent that, with the exception of a thin region close to the boundaries, the analytical and the numerical solutions are in very good agreement. In the inset, the velocity profile near the hydrodynamic boundary is highlighted.

the profile

$$\rho_w(\eta) = \frac{\rho_w^{(0)}}{c}\,(2-\eta)^{\alpha}\ , \tag{4.1}$$

where $\rho_w^{(0)}$ is the average wall particle density, η is the wall normal coordinate measured from the fluid side and

$$c = \frac{1}{2}\int_0^2 (2-\eta)^{\alpha}\,\mathrm{d}\eta = \frac{2^{\alpha}}{\alpha+1} \tag{4.2}$$

is a normalization factor. The boundary model depends on four parameters, namely $\rho_w^{(0)}$, α, a_{wf} and γ_{wf}, where a_{wf} and γ_{wf} characterize the fluid-wall force field. Impermeability, surface roughness and layering are controlled by $\rho_w^{(0)}$, α and a_{wf}. The slippage at the wall is quantified by the slip length L_s [97, 98]. Given $\rho_w^{(0)}$, α, and a_{wf}, λ can be tuned by changing γ_{wf}.

Planar channel. To evaluate the slip length L_s, a planar Poiseuille flow simulation was set up. The DPD system is simulated in a box of length $L = 42$, height $H = 14$ and width $W = 10$, as reported in figure 4.1a. The parameters of the fluid-fluid interactions are $a_{ff} = 16.67$ and $\gamma_{ff} = 1200$ with fluid bulk density $\rho_0 = 4.5$. The origin of the Cartesian coordinate system is set at the channel center, with the Oxz plane taken parallel to the planar walls and periodic boundary conditions applied in the streamwise, x, and spanwise, z, directions. For the wall particles distribution, eq. (4.1), $\rho_w^{(0)} = 24$ and $\alpha = 0.75$ were used. The wall particle density profile is represented in figure 4.1b (see the inset), red line. Figure 4.1b also reports the fluid particle density, blue line. Apparently, the wall model guarantees impermeability with particles partially entering the wall layer without ever going through. Differently from other approaches [93], a slight layering is

observed with fluid density at the wall within 5% of the bulk value. The density profile was verified to be independent of external forces applied in the streamwise direction.

In homogeneous systems, e.g. a planar or cylindrical channel, a Poiseuille flow can be induced applying a constant and uniform volume force density g along the channel axis. Since the particle density ρ_0 is homogeneous, this amounts to applying a constant force on each single particle. However, such procedure would not work in applications to inhomogeneous systems such as a sphere moving in the bulk. Following an alternative procedure, instead of uniformly forcing all the particles in the system, the planar Poiseuille flow was generated applying a constant force f along the z direction only to the fluid particles contained in a slab Ω of axial length $b = 2$ spanning normally across the channel. These particles are represented as blue spheres in fig 4.1a, while all the other fluid particles are represented as grey spheres.

The first step in mapping the continuum model into the DPD description consists in defining the nominal height of the channel. Indeed, in particle systems in which the wall is modelled by the interaction potential of the solid particles, there is no unique a priori defined bounding surface. The effective height can be defined consistently by establishing a connection between the external forces in the simulated system and the external forcing for a corresponding continuum system. Considering an idealized continuum system with height h, the total force acting on the fluid is

$$F_{TOT} = gWbh \ , \tag{4.3}$$

where g is the force volume density. On the other hand, the total (average)

external force applied to the DPD particles is

$$\langle F_E \rangle = f \langle N_\Omega(t) \rangle \ , \tag{4.4}$$

where $N_\Omega(t)$ is the number of particles in the region Ω at time t. In the bulk part of the Ω region, where the particle density has the constant value ρ_0, the force volume density of the simulated system is

$$g = f\rho_0 \ . \tag{4.5}$$

Under the approximation that eq. (4.5) holds in the whole channel of height h, equating the idealized total force eq. (4.3) to the effective total force eq. (4.4) leads to

$$h = \frac{N_\Omega}{\rho_0 bW} = \frac{N}{\rho_0 LW} \, , \tag{4.6}$$

where N is the total number of DPD fluid particles, and for the last equality the channel has been considered homogeneous along its length. The average value of the force density $\bar{g}$ is then

$$\bar{g} = \frac{F_{TOT}}{WLh} = f\rho_0 \frac{b}{L} \, . \tag{4.7}$$

where it has been considered that eq. (4.5) holds only in the region Ω.

As shown in figure 4.1c the proposed approach generates a parabolic velocity profile. Interestingly, the profile retains its parabolic shape down to a distance of approximately 0.5 from the hydrodynamic boundary, meaning that the correct hydrodynamics is recovered even at distances lower than the DPD particle interaction radius. Moreover, the planar Poiseuille flow can be used to measure the slip length L_s dependence on DPD parameters. Indeed, the analytical expression for planar Poiseuille flow with slippage is

$$u(y) = \frac{\bar{g}}{2\mu} \left(\frac{h^2}{4} - y^2 \right) + \frac{L_s \bar{g} h}{2\mu} \, , \tag{4.8}$$

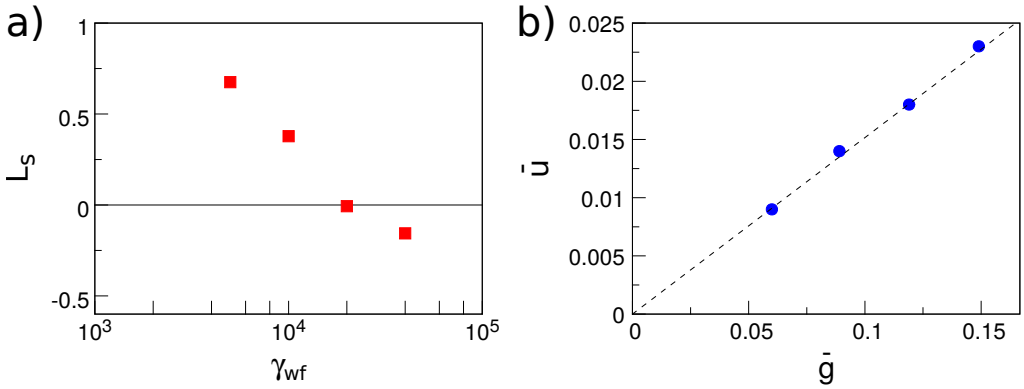

Figure 4.2: Slip length for planar Poiseuille flow. a) Slip length L_s as a function of the dissipative force parameter γ_{wf} between the wall and the fluid particles. L_s is calculated from Poiseuille flow simulations via equation (4.9). b) Mean velocity $\bar{u}$ for the planar Poiseuille flow as a function of the pressure gradient $\bar{g}$ for $\gamma_{wf} = 2 \cdot 10^4$. The dashed line is the analytical expression for no-slip boundaries ($L_s = 0$). The values $\rho_w^{(0)} = 24$, $a_{wf} = 5$ and $\alpha = 0.75$ are used in all the simulations. Error bars for both graphs are of the same size of the points.

with μ the fluid viscosity, from which an expression linking the mean velocity $\bar{u}$ with the slip length L_s is derived

$$\bar{u} = \frac{\bar{g}h^2}{12\mu} + \frac{L_s \bar{g} h}{2\mu} \, . \tag{4.9}$$

Consequently, the estimation of $\bar{u}$ from the simulations allows a direct measurement of L_s. The system was simulated for different γ_{wf}, the results being shown in fig. 4.2a. For $\gamma_{wf} = 2 \cdot 10^4$ a negligible slip length is measured. To confirm the no-slip condition under different forcings, also the $\bar{u}$ was measured for different effective pressure gradient $\bar{g}$, fig. 4.2b, obtaining a good agreement with the predictions for the no-slip condition, eq. (4.9) with $L_s = 0$.

Cylindrical channel. The above described model for the wall with the same parameters can be also used for cylindrical channels. In analogy with eq. (4.6), the effective cylinder radius is defined as

$$R = \sqrt{\frac{N}{\pi \rho_0 L_c}} \, , \tag{4.10}$$

while the slip length reads

$$L_s = \frac{2\mu\bar{u}}{\bar{g}R} - \frac{R}{4} \, , \tag{4.11}$$

with L_c the cylinder length. Imposing a Poiseuille flow with the same technique described above for the planar case we obtain a velocity profile in good agreement with no-slip conditions, see figure 4.3a. It is apparent that all the profiles for the different R collapse near the theoretical prediction for $L_s = 0$. The small discrepancy (the measured maximum velocity is $\simeq 5\%$

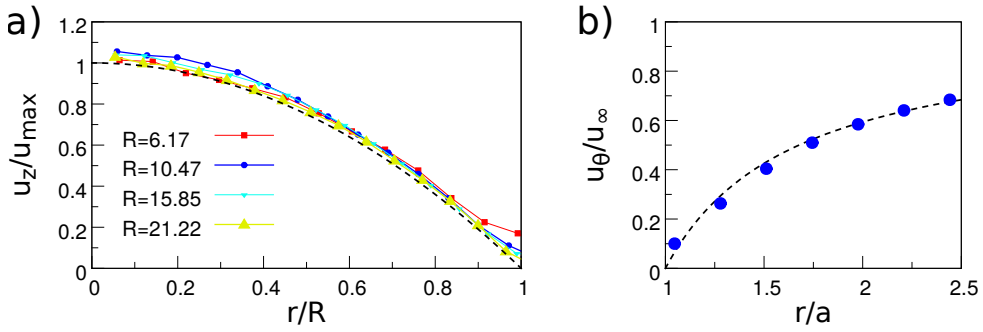

Figure 4.3: Wall model validation for curved surfaces. a) Hagen-Poiseuille velocity profile for cylindrical channel of radius R. The flow is generated as in the planar case, i.e. an axial force f is applied to every particle inside a region of the cylinder of width 2. The cylinder has length $L_c = 42$. Different colors correspond to different R while the black dashed line is the analytical expression. The radial position r is rescaled with the radius of the cylinder R, and the axial velocity is rescaled with the maximum velocity $u_{max} = \bar{g}R^2/(4\mu)$ for no-slip Hagen-Poiseuille flow. b) Tangential flow velocity profile u_θ for the spherical particle at rest in a uniform flow. The velocity is measured in a plane normal to the streaming velocity and passing through the sphere center. The black dashed line is the analytical solution [54] while the computed velocity is in blue circles. The radial coordinate is rescaled with the particle radius a, and the velocity is rescaled with the velocity of the fluid far from the sphere, u_∞. The data refer to $a = 2.13$, i.e. the sphere radius is only two times the size of a DPD particle.

higher than the no-slip maximum velocity) is due to a small slip introduced by the curvature, $L_s \simeq 0.2 \pm 0.1$.

Flow around a fixed sphere. Finally, the model was also tested for a spherical particle fixed in space. The sphere was built using the particle distribution of eq. (4.1) where now η is the radial coordinate originating from the sphere center. To check the capability of the wall model to reproduce a no-slip boundary condition, a triperiodic simulation was performed (cubic cell size $L_{box} = 90$) imposing, as in the Poiseuille simulations, a force f in a thin rectangular slice far from the sphere. After a transient, a stationary flow sets in. The average flow velocity in the slice and the force exerted on the sphere by the flow were measured. The ratio between these two quantities is the translational resistance γ_t that, in a no-slip continuum model, is related to the sphere radius a by the Stokes law $\gamma_t = 6\pi\mu a$. Simulations at different forcings allowed the estimation of the effective hydrodynamic radius as $a = 2.29 \pm 0.013$. The velocity field around the sphere is in good agreement with the continuum prediction, figure 4.3b. Finally, an additional simulation has been performed imposing a constant rotation to the sphere. Then the corresponding torque exerted by the fluid was measured, estimating the hydrodynamic radius from the rotational resistance for a no-slip sphere $\gamma_r = 8\pi\mu a^3$ [52]. The resulting effective sphere radius is $a = 2.13 \pm 0.0037$. The slight discrepancy between the two estimations of the particle radius a can be presumably ascribed to a small slippage that was already observed in the case of cylindrical channel, see figure 4.3a.

4.2 The Mobility Field

The studied system is represented in figure 4.4, consisting in a spherical particle of radius a in a cylindrical channel of radius R. DPD simulations with the previously described model for the cylindrical channel and the sphere were used to compute the mobility matrix $\boldsymbol{M}$, which is needed as an input for the Langevin equation (3.38). As the mobility field in the cylindrical channel is radial, different radial positions of the particle in the channel were considered. For each position, 6 simulations with the sphere translating and rotating along the three axes were performed. As represented in figure 4.4, the three forces and torques acting on the particle were measured, obtaining the complete resistance matrix at each radial position, then inverting it to obtain the mobility. In the bulk, the mobility matrix of a spherical particle is diagonal and, in particular, $M_{11} = M_{22} = M_{33} = (6\pi\mu a)^{-1}$ and $M_{44} = M_{55} = M_{66} = (8\pi\mu a^3)^{-1}$. The confinement affects the mobility matrix $\boldsymbol{M}$ that, in general, is not diagonal and depends on the particle position and orientation (six rigid body degrees of freedom). In the present case, a sphere moving in a cylinder, since the mobility and resistance matrices depend only on the radial coordinate r, it is convenient to represent them in cylindrical coordinates. For symmetry reasons, several terms of the resistance matrix in

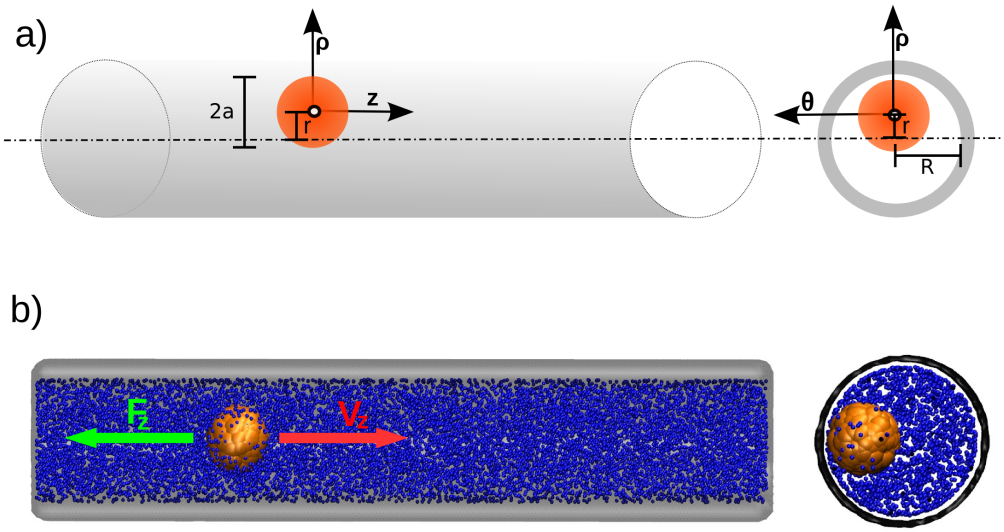

Figure 4.4: Scheme of the simulated system and calculation of the resistance matrix. a) A spherical particle of radius a is located in a cylindrical channel of radius R. The particle reference frame has origin in the particle center and it is constituted by the radial axis $\vec{\rho}$, the transversal axis $\vec{\theta}$ and the axial direction $\vec{z}$. The distance between the particle center and the cylinder center is r. b) Snapshot of the DPD simulation used to calculate the resistance matrix of the particle inside the cylinder. To determine the resistance matrix for a given particle position, six simulations have been carried out. In each simulation one of the six velocity components, three translational in the $\left(\vec{\rho}, \vec{\theta}, \vec{z}\right)$ directions and three rotational, is imposed while the other five are zero. For each run, the six components of the generalized forces, three forces and the three torques, acting on the particle are measured, leading to the 36 values of the resistance matrix eq. (4.12). In the panel b, the procedure to calculate $\gamma_{zz} = -F_z/V_z$, with V_z the imposed translational velocity and F_z the average measured force along the z-axis, is sketched.

cylindrical coordinates $\mathbf{\Gamma}_{cyl}$ are equal to zero and the matrix reads

$$\mathbf{\Gamma}_{cyl} = \begin{pmatrix} \gamma_{\rho\rho} & 0 & 0 & 0 & 0 & 0 \\ 0 & \gamma_{\theta\theta} & 0 & 0 & 0 & \gamma_{\theta\zeta} \\ 0 & 0 & \gamma_{zz} & 0 & \gamma_{z\eta} & 0 \\ 0 & 0 & 0 & \gamma_{\xi\xi} & 0 & 0 \\ 0 & 0 & \gamma_{z\eta} & 0 & \gamma_{\eta\eta} & 0 \\ 0 & \gamma_{\theta\zeta} & 0 & 0 & 0 & \gamma_{\zeta\zeta} \end{pmatrix} . \tag{4.12}$$

Here, the indexes ρ, θ and z represent translations (or forces) along the $\vec{\rho}$, $\vec{\theta}$ and $\vec{z}$ axes in figure 4.4, while ξ, η and ζ represent rotations (or moments) around the same axes. As an example, the $\gamma_{z\eta}$ component was calculated dividing the opposite force along the $\vec{z}$ axis when the particle was rotating around the $\vec{\theta}$ axis or, equivalently, dividing the opposite torque acting along the $\vec{\theta}$ axis when the particle was translating along the $\vec{z}$ axis. Figure 4.5 reports the six diagonal components of the resistance matrix. The first three plots refer to the three translational resistances, and are normalized with respect to the bulk resistance $\gamma_t = 6\pi\mu a$, with $a = 2.13$. The last three plots refer to the three rotational resistances, and are normalized with respect to the bulk resistance $\gamma_r = 8\pi\mu a^3$, with $a = 2.13$. The confinement ratio is defined as $\lambda = R/a$ and the normalized position as $\chi = r/(R - a)$. The components of the resistance matrix for four values of λ and seven values of χ were calculated. Apart from the translational radial component γ_{rr}, all the resulting resistances grow sharply near the wall, as expected.

In order to use the resistance matrix $\mathbf{\Gamma}_{cyl}$ in the Langevin equation (3.38), it has to be transformed in Cartesian coordinates. The transformation is

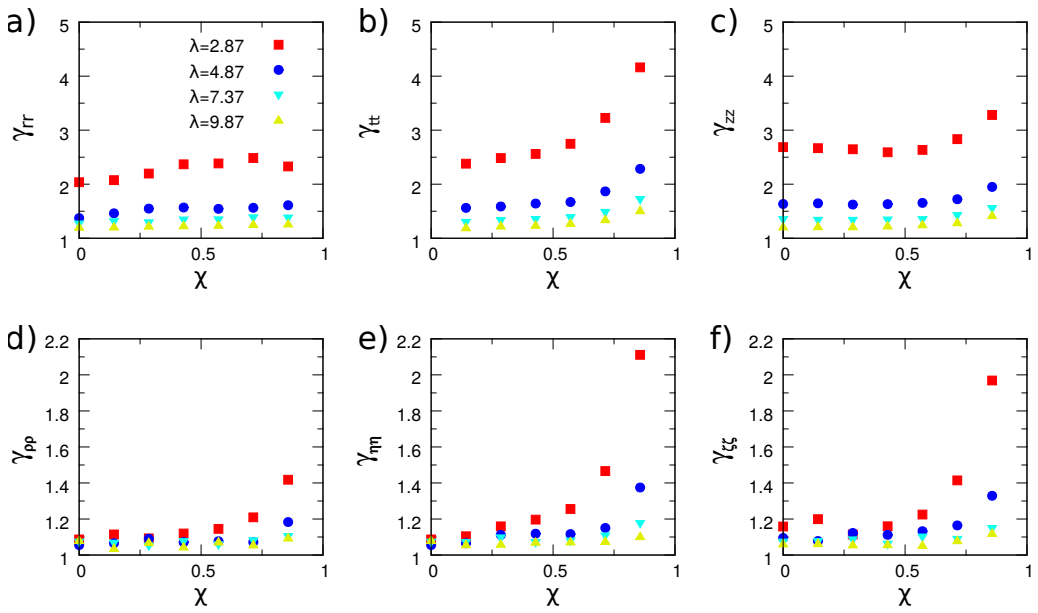

Figure 4.5: Diagonal components of the resistance matrix, eq. (4.12), as a function of the normalized position $\chi = r/(R-a)$ for different confinement ratios $\lambda = R/a$. The resistance values are normalized with respect to the bulk resistance, $\gamma_t = 6\pi\mu a$ for the translational components and $\gamma_r = 8\pi\mu a^3$ for the rotational components.

$\boldsymbol{M}_{cart} = \boldsymbol{R}\boldsymbol{\Gamma}_{cyl}^{-1}\boldsymbol{R}^T$, where $\boldsymbol{R}$ is the change of basis matrix

$$\boldsymbol{R} = \begin{pmatrix} \cos(\psi) & \sin(\psi) & 0 & 0 & 0 & 0 \\ -\sin(\psi) & \cos(\psi) & 0 & 0 & 0 & 0 \\ 0 & 0 & 1 & 0 & 0 & 0 \\ 0 & 0 & 0 & \cos(\psi) & \sin(\psi) & 0 \\ 0 & 0 & 0 & -\sin(\psi) & \cos(\psi) & 0 \\ 0 & 0 & 0 & 0 & 0 & 1 \end{pmatrix}, \tag{4.13}$$

where ψ is the angle which the particle position vector forms with the $\vec{x}$ axis of the Cartesian frame of reference used for the Langevin formulation.

Chapter 5

Diffusion of a spherical particle in a nanochannel

Langevin simulations as described in section 3.3 were performed, using the mobility field obtained with the DPD simulations, see section 4.2. The output of each simulation is a trajectory, i.e. the time evolution of the position of the center of the particle and of the quaternion representing the orientation. In experimental conditions, the quantity which is usually measured is the effective diffusion coefficient D_{eff} along the channel axis [99]. To calculate D_{eff}, the mean square displacement C_{zz} has to be computed

$$C_{zz}(\tau) = \langle (z(t+\tau) - z(t))^2 \rangle_t \,, \tag{5.1}$$

where $\langle \cdot \rangle_t$ refers to the time average. The time evolution of C_{zz} for different $\lambda = R/a$ is plotted in figure 5.1a. C_{zz} increases linearly with τ, indicating, as expected, a diffusive behaviour that can be described in term of the effective

diffusion coefficient

$$D_{eff} = \frac{1}{2} \lim_{\tau \to \infty} \frac{\mathrm{d}C_{zz}(\tau)}{\mathrm{d}\tau} \,, \tag{5.2}$$

here calculated via a linear fitting of the data in fig. 5.1a.

5.1 Free diffusion under confinement

The diffusive motion of the confined particle in four different confining conditions was first simulated. The resulting D_{eff}, as defined in eq. (5.2), rescaled with the bulk value

$$D_t = \frac{k_B T}{6\pi\mu a} \,, \tag{5.3}$$

is plotted in figure 5.1b as a function of confinement parameter λ, red squares. For $\lambda = 2.87$ the diffusion is reduced approximately by a factor 3, in quantitative agreement with experimental observations for similar confining conditions [99]. Figure 5.1b also reports other literature results for the diffusion coefficient of a spherical particle in a cylindrical channel [1]. Two predictions for D_{eff}/D_t were taken into account. The first one, dashed line in figure 5.1b, was obtained by Renkin [101] using the centerline approximation, i.e. considering the mobility of the particle in the whole channel equal to the mobility at the center. The second one, dotted line in figure 5.1b, was obtained by Dechadilok and Deen [100] fitting the results of boundary element method

[1] the present results for the effective diffusion coefficient were compared with the local hindrance factor K_d in formula (2) of the work by Dechadilok and Deen [100], using equations (9), (11), and (16) in the cited work. Notice that, in their work, the symbol λ is defined as the inverse of the λ used here (i.e. $\lambda = a/R$). A similar procedure was done for the centerline approximation results [101]

simulation [102]. The here reported results for the effective diffusion D_{eff} are in good agreement with both these predictions. It is worth noting that the estimation of the diffusion coefficient for both curves uses only the axial hydrodynamic resistance γ_{zz}, while this approach takes into account the complete mobility matrix that includes the coupling between rotations and translations, see eq. (4.12). The good agreement between the Brownian simulations and the results of [101, 100] suggests that in this system constituted by a confined spherical particle the rotation-translation coupling plays a minor role.

The rigid body Langevin approach allows the calculation of the effect of confinement on the rotational diffusion. To calculate the rotational diffusivity, the rotational displacement vector is defined as [103, 88]

$$\Delta\vec{e}(t_1, t_2) = \frac{1}{2}\sum_{i=1}^{3} \vec{e}_i(t_1) \times \vec{e}_i(t_2) \ , \tag{5.4}$$

where $\vec{e}_i$, $i \in [1, 3]$ is a tern of unitary body fixed orthogonal vectors. In analogy with the translational case, the rotational mean square displacement can be defined as

$$\boldsymbol{C}_{rot}(\tau) = \langle \Delta\vec{e}(t, t+\tau) \otimes \Delta\vec{e}(t, t+\tau) \rangle_t \ . \tag{5.5}$$

Since there is no coupling between different rotations, see eq. (4.12), $\boldsymbol{C}_{rot}$ is diagonal, the symbol $C_{\zeta\zeta}$ denotes the rotations parallel to the cylinder axis, and $C_{\eta\eta}$ and $C_{\xi\xi}$ for the other two components corresponding to rotations orthogonal to the cylinder axis. The axial component $C_{\zeta\zeta}$ is plotted in figure 5.1c. Unlike the translational case, it is expected that $C_{\zeta\zeta}$ reaches a plateau (dotted line in figure 5.1c), which in absence of external forcing, has

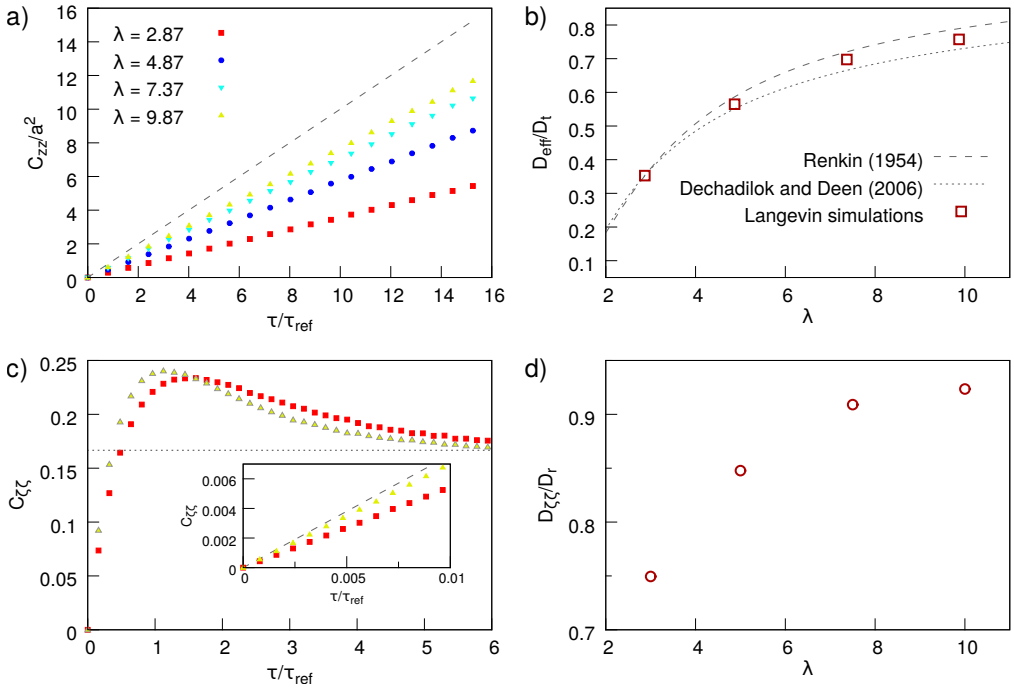

Figure 5.1: Results of the Langevin simulations. a) Mean square displacement C_{zz}, eq. (5.1), for different confinement λ. The axial position is normalized with the radius of the particle a, and the reference time is the time necessary for the particle to move in the bulk of a distance equal to its radius $\tau_{ref} = \frac{a^2}{2D_t}$. The dashed line corresponds to the bulk diffusion slope. b) Effective diffusion coefficient as a function of λ, as computed from the Langevin simulations (red squares). The dashed line is the analytical result calculated with the centerline approximation [101], and the dotted line represents the curve obtained by Dechadilok and Deen fitting computational results [100]. c) Axial rotational displacement covariance $C_{\zeta\zeta}$ for $\lambda = 3$ (red points) and for $\lambda = 10$ (yellow points). The horizontal dotted line represents the value reached for large τ in the case of free diffusion, eq. (5.6) [88]. The inset is a zoom of the curve for low τ, where $C_{\zeta\zeta}$ is almost linear. The rotational diffusion coefficient was computed considering the slope of $C_{\zeta\zeta}$ for small τ. The dashed line in the inset corresponds to the slope in the bulk diffusion case. d) Axial rotational diffusion coefficient $D_{\zeta\zeta}$ as a function of λ.

to be [88]

$$\lim_{\tau\to\infty} C_{\zeta\zeta}(\tau) = \frac{1}{6} \,. \tag{5.6}$$

The slope of $C_{\zeta\zeta}$ for $\tau \to 0$ (see the inset in figure 5.1c) is related to the rotational diffusion coefficient

$$D_{\zeta\zeta} = \lim_{\tau\to 0} \frac{1}{2} \frac{\mathrm{d}C_{\zeta\zeta}}{\mathrm{d}t} \,. \tag{5.7}$$

The rotational diffusion coefficient orthogonal to the cylinder axis, $D_{\xi\xi}$ and $D_{\eta\eta}$, which in absence of external forcing are equal, can be obtained similarly. Figure 5.1d reports the axial, $D_{\zeta\zeta}$ rotational diffusion plotted as a function of the confining parameter λ normalized with respect to the bulk rotational diffusivity

$$D_r = \frac{k_B T}{8\pi\mu a^3} \,. \tag{5.8}$$

The measured reduction of the rotational diffusion coefficient is smaller with respect to the translational case, a maximum reduction of 25% is observed in the most confined case $\lambda = 3$. No significant differences were observed for transverse rotational diffusion coefficients $D_{\xi\xi}$ and $D_{\eta\eta}$.

5.2 Diffusion in presence of a constant external force

The proposed method allows to study the effect of external forces on the particle diffusion. In general, the presence of an external force modifies the equilibrium distribution of the particle (fig. 5.2a). To quantify this effect,

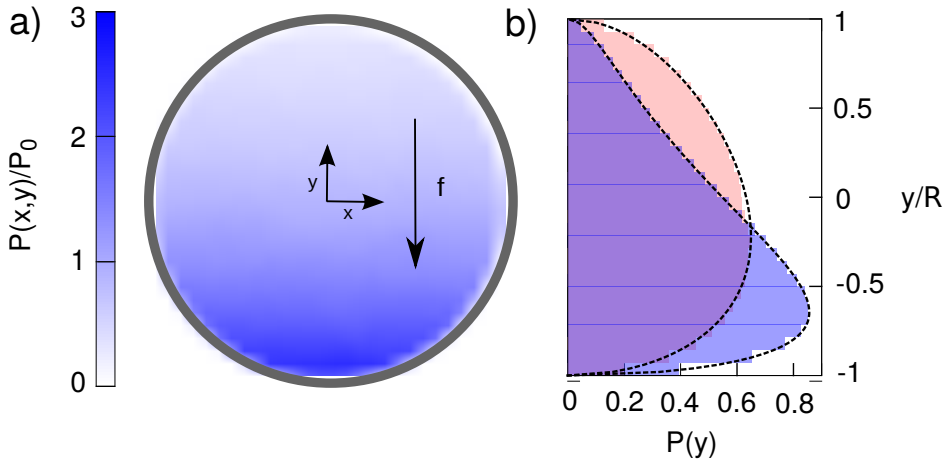

Figure 5.2: Distribution of particle position when a constant force orthogonal to the cylinder axis is applied. The position is projected into a section of the cylinder to obtain a 2-D map. a) Sketch of the applied force and of the corresponding 2-D distribution, for $\lambda = 10$ and $f = 0.125 k_B T/a$. The probability distribution $P(x, y)$ is normalized with respect to the uniform distribution $P_0 = 1/(\pi R^2)$. b) Particle equilibrium distribution along the y axis. The red and blue histograms correspond to $\lambda = 2.87$ and $\lambda = 9.87$, respectively. For both cases, $f = 0.125 k_B T/a$. The dashed lines represent the predictions from eq. (5.10).

a constant force $\vec{f} = -f\hat{y}$ was applied and both the resulting equilibrium distribution and the diffusion coefficients were measured. The force is parallel to the y axis, which is orthogonal to the cylinder axis, and the Langevin simulations were performed for five different values of the external force. The equilibrium distribution of the particle position projected on the cylinder section is the canonical distribution

$$P(x,y) = \frac{1}{Z_1} e^{-\beta f y} \ , \tag{5.9}$$

where Z_1 is a normalization constant. This results in the following distribution along the y axis

$$P(y) = \int_{-\bar{x}(y)}^{\bar{x}(y)} P(x,y)\mathrm{d}x = \frac{2}{Z_1}\sqrt{(R-a)^2 - y^2}\ e^{-\beta f y} \ , \tag{5.10}$$

where $\bar{x}(y) = \sqrt{(R-a)^2 - y^2}$ delimits the integration domain for a circular section of the channel as a function y. In figure 5.2b the function $P(y)$ is plotted for two different cylinders ($\lambda = 9.87$ and $\lambda = 2.87$) for $f = 0.125 k_B T/a$. The $P(y)$ measured from the simulated trajectories is in good agreement with eq. (5.10). The distribution histogram presents a more evident peak in the case of large cylinder (blue). This is expected because the effect of the force depends not only on the force magnitude f, but also on the cylinder radius, as reported in eq. (5.10).

The change in the equilibrium distribution induced by the external force modifies the average mobility explored by the particle. As a consequence, the effective diffusion may differ from the case with no external forces. To quantify this effect, using the same approach as in the free diffusion case, we computed the equivalent axial diffusion coefficient in presence of a constant

external force. The effective diffusion coefficient D_{eff}, as defined in eq. (5.2), is plotted in figure 5.3a as a function of the intensity of the applied force f for different values of λ, and it is normalized with respect to the value in absence of forces (already reported in figure 5.1b). The plot shows that the application of a force results in a reduction of the axial diffusion coefficient which is higher in the less confined case ($\lambda \simeq 10$). This effect can be explained considering that the equilibrium distribution is more peaked in region of low mobility for larger cylinders, see figure 5.2b. Interestingly, for the rotational diffusion, the behaviour with the confinement is more complex. For large f the reduction in diffusion is higher for the most confined systems, while for low f, the reduction in the rotational diffusion coefficients at different confinements is very similar, see figure 5.3b for $D_{\zeta\zeta}$. A similar behaviour is observed for $D_{\eta\eta}$ and $D_{\xi\xi}$.

5.3 Dipolar particle in a uniform electric field

As a second case of study, the dynamics of a particle with a constant dipole moment $\vec{p}$ of intensity p_0 under the action of a uniform electric field directed along the cylinder axis, $\vec{E} = E_0\hat{z}$ was studied. The corresponding potential energy is

$$U(\alpha) = p_0 E_0 \cos(\alpha) \ , \tag{5.11}$$

where α is the angle between the dipole and the electric field. The potential energy can be expressed as a function of the quaternions as

$$U(\boldsymbol{q}) = p_0 E_0 \hat{z} \cdot \boldsymbol{B}(\boldsymbol{q}) \hat{z}' \ , \tag{5.12}$$

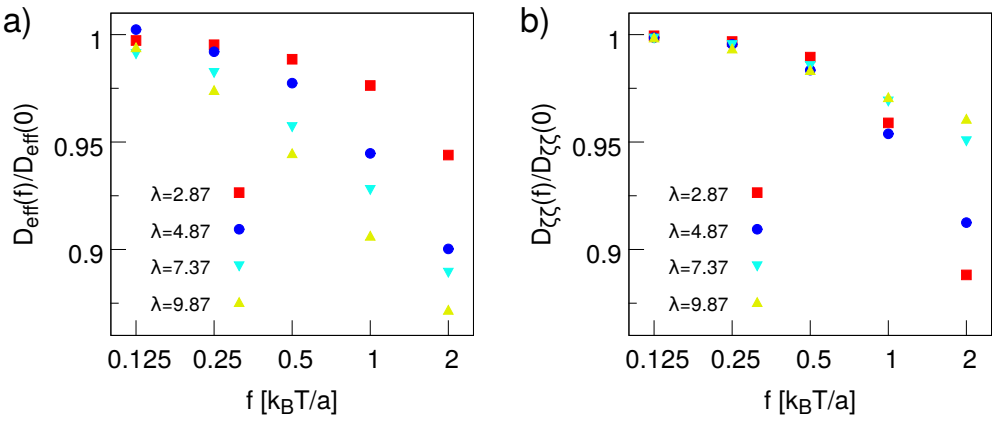

Figure 5.3: Results of the Langevin simulations with a constant force orthogonal to the cylinder axis applied on the particle. a) Effective diffusion coefficient D_{eff} as a function of the external force f, for different confinement parameters λ. For each value of λ, the effective D_{eff} is normalized with respect to $D_{eff}(0)$, i.e. the effective diffusion in absence of external forces, but in presence of confinement. b) Axial rotational diffusion coefficient, eq. (5.6), as a function of f for different λ. Again, the values are normalized with respect to the diffusion in absence of external force.

where the matrix $\boldsymbol{B}(\boldsymbol{q})$ is the rotation matrix that applied to the vector in the body reference frame gives the corresponding fixed reference frame vector, i.e. $\vec{v} = \boldsymbol{B}(\boldsymbol{q})\vec{v}'$, see eq. (3.14). The corresponding torque is given by

$$\vec{t} = -\boldsymbol{\Phi}^T \boldsymbol{\nabla}_{\boldsymbol{q}} U \ , \tag{5.13}$$

which is the external forcing applied in the simulations, with U defined in eq. (5.12). All the simulations are performed at $p_0 = 1$ varying the external field intensity E_0. In the case of no forcing, $E_0 = 0$, the rotational equilibrium distribution has to be uniform, in the sense that all the directions in the space are equiprobable. This implies that the distribution as a function of α, i.e. the angle between the dipole of the particle and the axis of the cylinder, see Figure 5.5a, is

$$\rho_0(\alpha) = \frac{\sin(\alpha)}{2} \ , \tag{5.14}$$

In the following, without loss of generality, the electrical field will be considered parallel to the $\hat{z}$ axis of a Cartesian frame of reference. The potential energy (and therefore the relative probability density function, pdf) depends only on the angle α, which can be expressed in terms of quaternions, i.e. $\alpha = \alpha(\boldsymbol{q})$. The potential energy as a function of the quaternions can be formally written as

$$U(\boldsymbol{q}) = \tilde{U}(\alpha(\boldsymbol{q})) = p_0 E_0 \cos(\alpha(\boldsymbol{q})) \ . \tag{5.15}$$

The corresponding equilibrium pdf is

$$\rho(\boldsymbol{q}) = \frac{1}{Z} e^{-\beta U(\boldsymbol{q})} \delta(|\boldsymbol{q}| - 1) \ , \tag{5.16}$$

where the Dirac delta function accounts for the normalization of the quaternion to unit length and Z is the normalization factor

$$Z = \int_{\mathbb{R}^4} e^{-\beta U(\boldsymbol{q})} \delta(|\boldsymbol{q}| - 1) \mathrm{d}^4\boldsymbol{q} \ . \tag{5.17}$$

The pdf of the angle $\hat{\alpha} = \alpha(\boldsymbol{q})$ is then

$$\rho(\hat{\alpha}) = \frac{1}{Z_\alpha} \int_{\mathbb{R}^4} e^{-\beta U(\boldsymbol{q})} \delta(|\boldsymbol{q}| - 1) \delta(\alpha(\boldsymbol{q}) - \hat{\alpha}) \mathrm{d}^4\boldsymbol{q} \ , \tag{5.18}$$

where Z_α is the corresponding normalization factor

$$Z_\alpha = \int_0^\pi \mathrm{d}\hat{\alpha} \int_{\mathbb{R}^4} e^{-\beta U(\boldsymbol{q})} \delta(|\boldsymbol{q}| - 1) \delta(\alpha(\boldsymbol{q}) - \hat{\alpha}) \mathrm{d}^4\boldsymbol{q} \ . \tag{5.19}$$

In order to compute the integral in eq. (5.18), it is convenient to perform a change of variables, switching to an axis-angle description of the particle orientation, see figure 5.4. In particular, the direction of particle dipole $\hat{p} = \vec{p}/p_0$ is expressed by the two angles $\alpha \in [0, \pi]$ and $\theta \in [0, 2\pi]$, while the rotation around $\hat{p}$ is given by $\psi \in [0, 2\pi]$.

The quaternions can be expressed in terms of α, θ and ψ (from eq. (3.9) after some algebra) as

$$\begin{aligned} q_0 &= \lambda \cos\left(\frac{\psi}{2}\right) \\ q_1 &= \lambda \cos(\theta) \sin(\alpha) \sin\left(\frac{\psi}{2}\right) \\ q_2 &= \lambda \sin(\theta) \sin(\alpha) \sin\left(\frac{\psi}{2}\right) \\ q_3 &= \lambda \cos(\alpha) \sin\left(\frac{\psi}{2}\right) \ , \end{aligned} \tag{5.20}$$

where $\lambda = |\boldsymbol{q}|$ is a scaling parameter introduced to represent a quaternion with arbitrary norm. The jacobian matrix of the transformation (5.20) is

$$\boldsymbol{J} = \begin{pmatrix} -\frac{\lambda}{2}\sin(\frac{\psi}{2}) & \frac{\lambda}{2}\cos(\theta)\sin(\alpha)\cos(\frac{\psi}{2}) & \frac{\lambda}{2}\sin(\theta)\sin(\alpha)\cos(\frac{\psi}{2}) & \frac{\lambda}{2}\cos(\alpha)\cos(\frac{\psi}{2}) \\ 0 & \lambda\cos(\theta)\cos(\alpha)\sin(\frac{\psi}{2}) & \lambda\sin(\theta)\cos(\alpha)\sin(\frac{\psi}{2}) & -\lambda\sin(\alpha)\sin(\frac{\psi}{2}) \\ 0 & -\lambda\sin(\theta)\sin(\alpha)\sin(\frac{\psi}{2}) & \lambda\cos(\theta)\sin(\alpha)\sin(\frac{\psi}{2}) & 0 \\ \cos(\frac{\psi}{2}) & \cos(\theta)\sin(\alpha)\sin(\frac{\psi}{2}) & \sin(\theta)\sin(\alpha)\sin(\frac{\psi}{2}) & \cos(\alpha)\sin(\frac{\psi}{2}) \end{pmatrix}, \tag{5.21}$$

with determinant

$$|\boldsymbol{J}(\theta,\alpha,\psi,\lambda)| = \frac{\lambda^3}{2}\sin(\alpha)\sin^2\left(\frac{\psi}{2}\right) . \tag{5.22}$$

Equation (5.18) can now be rewritten as

$$\rho(\hat{\alpha}) = \frac{1}{Z_\alpha}\int_0^{2\pi}\mathrm{d}\psi\int_0^{2\pi}\mathrm{d}\theta\int_0^{\pi}\mathrm{d}\alpha\int_0^{\infty} e^{-\beta\tilde{U}(\alpha)}\delta(\lambda-1)\delta(\alpha-\hat{\alpha})|\boldsymbol{J}(\theta,\alpha,\psi,\lambda)|\mathrm{d}\lambda . \tag{5.23}$$

Substituting eq. (5.22) into eq. (5.23) and integrating, we are left with

$$\rho(\hat{\alpha}) = \frac{1}{Z_\alpha}\pi^2 e^{-\beta\tilde{U}(\hat{\alpha})}\sin(\hat{\alpha}) , \tag{5.24}$$

where

$$Z_\alpha = \pi^2\int_0^{\pi} e^{-\beta\tilde{U}(\alpha)}\sin(\alpha)\mathrm{d}\alpha . \tag{5.25}$$

Substituting eq. (5.15) into eq. (5.24) and eq. (5.25), the final expression for the pdf of the angle α between the particle dipole $\vec{p}$ and the electric field $\vec{E}$ is obtained

$$\rho(\alpha) = \frac{p_0 E_0}{2\sinh(p_0 E_0)} e^{-\beta p_0 E_0\cos(\alpha)}\sin(\alpha) . \tag{5.26}$$

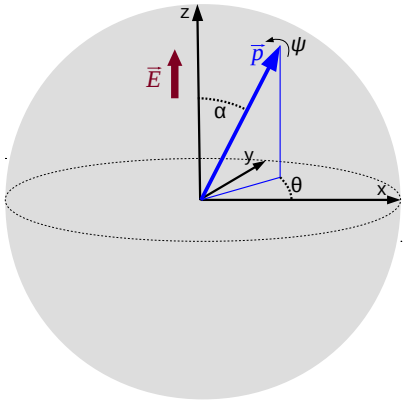

Figure 5.4: Sketch of the relative orientation between particle dipole $\vec{p}$ and electric field $\vec{E}$. Two angles, α and θ, specify the orientation of the dipole direction $\hat{p} = \vec{p}/p_0$ while the angle ψ specifies the rotation of the particle around $\hat{p}$. The electric field is directed along $\hat{z}$.

Figure 5.5b reports the analytical prediction of eq. (5.26) and the numerical results, that are in perfect agreement. As discussed in section 5.1, the simulations allowed the calculation of effective axial diffusion coefficient D_{eff}. We observe no detectable effect of the applied electric field on D_{eff}.

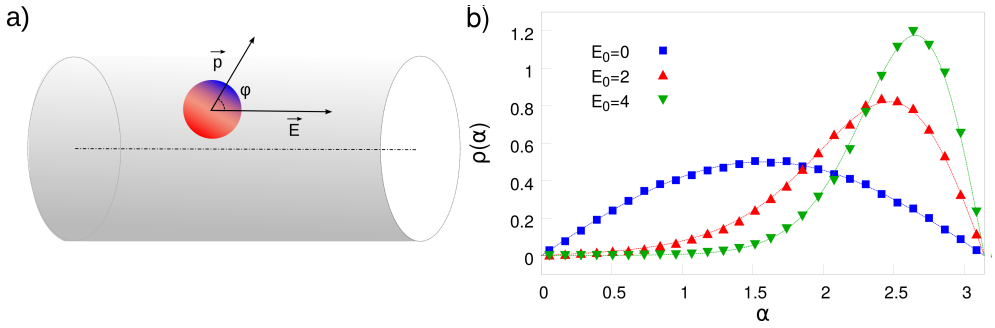

Figure 5.5: Results of the Langevin simulations with a constant electric field $\vec{E} = E_0\hat{z}$ parallel to the cylinder axis applied on a particle with an electric dipole. a) Sketch of the system. A particle with an electric dipole $\vec{p}$ moves in a cylindrical channel in which a constant electric field $\vec{E}$ is applied. The relevant angle for the potential energy of the particle, i.e. eq. (5.11), is the angle α between $\vec{p}$ and $\vec{E}$. b) Probability distribution of α for three different values of the electric field intensity E_0. The numerical results, squares and triangles, are compared with the analytical formula, eq. (5.26), dashed lines.

Part III
Coarse-graining of charged fluids

In this part, a model for the dynamics of electrolytes in presence of pressure gradients and/or electric fields is presented. The model is based on the Dissipative Particle Dynamics equations of motion with the addition of the electrostatic force. Each particle is described by the usual position and velocity, plus two additional variables representing the quantity of cations and anions carried. The equations of motion for the new variables are written in such a way that the resulting set of equations has as an equilibrium solution the Boltzmann distribution for the appropriate thermodynamic potential, which includes the electrostatic energy. The conductance of the resulting electrolyte is shown to be linearly dependent on the concentration of ions. The model is validated against some electrohydrodynamic systems which have a known analytical solution under the Debye approximation.

Chapter 6

DPD model for electrohydrodynamics

In this chapter, a coarse grained model able to simulate the electrohydrodynamic phenomena taking place in electrolyte solutions will be presented. The fluid is modelled as a system of N interacting particles with equal mass whose equations of motion are inspired to Dissipative Particle Dynamics. In order to represent the effect of dissolved charges, two additional degrees of freedom are included for each particle. In addition to the 6 degrees of freedom representing the positions and velocities of the i^{th} particle $\boldsymbol{x}_i$ and $\boldsymbol{v}_i$, the variables n_i^c and n_i^a represent the quantity of two species carried by the particle, the cations and the anions respectively. Although only two charged species are considered, the model can be easily generalized to include electrolyte solutions with more species. The equations of motion for the above mentioned variables will be reported, and it will be shown that, if appropriate fluctuation-dissipation conditions are satisfied, the proposed dynamics

admits an equilibrium distribution. Since the equilibrium distribution of a system is related to its thermodynamic potential, this gives a link between the terms arising in the equations of motion and the thermodynamic properties of the particles, allowing a consistent definition of pressure and chemical potential of the particle. The electrostatic interactions between charged particles are computed considering the charge carried by each particle to be distributed as a Gaussian of constant variance located in the particle center. The chemical potential used in the model is that of a perfect gas plus a contribution due to the electrostatic interactions. The dissipative factors (such as γ in standard DPD) for the ionic transport are modelled to reproduce a conductance which is linearly dependent on the ionic average concentration. It will be shown that this implies the necessity of considering an additional drift in order for the system to reach the desired equilibrium distribution.

6.1 Structure of the equations of motion

The fluid is described by N particles of equal mass m. The state of the i^{th} particle is described by its position $\boldsymbol{x}_i$, velocity $\boldsymbol{v}_i$, quantity of cations n_i^c and quantity of anions n_i^a. The vector of state has therefore dimension $8N$. The

equations for the dynamics of the state variables for the i^{th} particles are

$$\begin{aligned}
&\mathrm{d}\boldsymbol{x}_i = \boldsymbol{v}_i \mathrm{d}t \ , \\
&m\mathrm{d}\boldsymbol{v}_i = \boldsymbol{F}_i^C \mathrm{d}t + \sum_{j\neq i} \left[\gamma w^D(r_{ij}) \left(\boldsymbol{v}_{ji}\cdot\boldsymbol{e}_{ij}\right)\mathrm{d}t + \sigma w^R(r_{ij})\mathrm{d}W_{ij}^v\right]\boldsymbol{e}_{ij} \ , \\
&\mathrm{d}n_i^c = \sum_{j\neq i} \left[\gamma^c w^D(r_{ij})\mu_{ji}^c \mathrm{d}t + w^D(r_{ij})h_{ij}^c \mathrm{d}t + \sigma^c w^R(r_{ij})\mathrm{d}W_{ij}^c\right] \ , \\
&\mathrm{d}n_i^a = \sum_{j\neq i} \left[\gamma^a w^D(r_{ij})\mu_{ji}^a \mathrm{d}t + w^D(r_{ij})h_{ij}^a \mathrm{d}t + \sigma^a w^R(r_{ij})\mathrm{d}W_{ij}^a\right] \ ,
\end{aligned} \tag{6.1}$$

where there is an implied summation over the j indexes. The first and second equations have the structure of the standard DPD equations, where $\boldsymbol{F}_{ij}^C$ is a (for now unspecified) conservative force, and the quantities γ and σ are constant parameters which control the intensity of the other two forces, i.e. the dissipative force

$$\boldsymbol{F}_{ij}^D = \gamma w^D(r_{ij}) \left(\boldsymbol{v}_{ji}\cdot\boldsymbol{e}_{ij}\right)\boldsymbol{e}_{ij} \ , \tag{6.2}$$

and the stochastic force

$$\boldsymbol{F}_{ij}^R = \sigma w^R(r_{ij})\boldsymbol{e}_{ij}\mathrm{d}W_{ij}^v \ . \tag{6.3}$$

The functions w^D and w^R are weight functions which depend on the relative particle distance $r_{ij} = |\boldsymbol{x}_i - \boldsymbol{x}_j|$. Such weight functions are maximum for $r_{ij} = 0$, and vanish if the interparticle distance is larger than a cutoff radius r_c, their practical effect being to exclude interactions between distant particles and to increase the interaction between near particles. There is no prescribed functional form for the weight functions, here the original DPD expressions

are used

$$w^R(r_{ij}) = \begin{cases} 1 - r_{ij}/r_c & \text{if } r_{ij} \leq r_c \ , \\ 0 & \text{if } r_{ij} > r_c \ , \end{cases} \tag{6.4}$$
$$w^D(r_{ij}) = \left(w^R(r_{ij})\right)^2 \ .$$

Both the dissipative and stochastic forces act in the direction of the particle-particle unit vector, i.e. $\boldsymbol{e}_{ij} = (\boldsymbol{x}_i - \boldsymbol{x}_j)/r_{ij}$. The dissipative force depends on the axial component of the relative particle velocity, i.e. $\boldsymbol{e}_{ij} \cdot \boldsymbol{v}_{ji} = \boldsymbol{e_{ij}} \cdot (\boldsymbol{v_j} - \boldsymbol{v}_i)$, while the stochastic force depends on a set of independent white noise processes

$$\xi^v_{ij} = \frac{\mathrm{d}W^v_{ij}}{\mathrm{d}t} \ , \tag{6.5}$$

one for each pair of particles. These stochastic processes are such that

$$\begin{aligned} \left\langle \xi^v_{ij}(t) \right\rangle &= 0 \ , \\ \left\langle \xi^v_{ij}(\tau_1) \xi^v_{ij}(\tau_2) \right\rangle &= \delta(\tau_1 - \tau_2) \ , \end{aligned} \tag{6.6}$$

with $\xi_{ij} = \xi_{ji}$, a consequence being that the dissipative and random forces both conserve total momentum. The third and fourth equations govern the dynamics of the quantity of cations and ions carried by the particles, and are composed by a sum of three terms in which the structure of the first and the third have analogous structure if compared with the dissipative and random forces in the equation for the velocities. In fact, the above cited weight functions w^D and w^R appear in both equations and, as in the equation for the velocity, the magnitude of the dissipative and stochastic terms is controlled by four (not constant) factors, two dissipative factors γ^c and σ^c and two noise factors γ^a and σ^a. The second term arises from the fact that γ^c and γ^a are not constant but depend on the state of the system, and it will be shown that

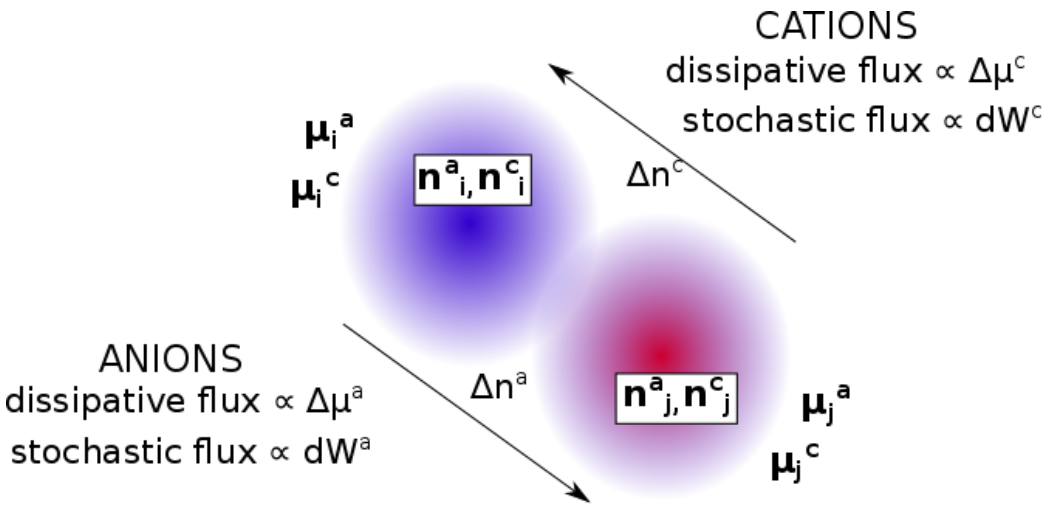

Figure 6.1: Sketch of the exchange of ions between two particles. The two particles i and j represented have different concentrations of both species, resulting in different charge and chemical potential. Two cation fluxes and two anion fluxes arise, one dissipative flux related to the difference of chemical potential, and one stochastic flux proportional to a white noise process.

this term is needed to guarantee the existence of an equilibrium solution for system of Eq. (6.1). The dissipative term in the third and fourth equations is proportional to the chemical potential difference between the particles, i.e. $\mu^c_{ji} = \mu^c_j - \mu^c_i$,where the chemical potential is a function to be specified $\mu^c_i = \mu^c_i(\boldsymbol{x}, \boldsymbol{n^c}, \boldsymbol{n^a})$. The second term is the stochastic ion flux, including one independent white noise process for each pair of particles, respectively

$$\xi^c_{ij} = \frac{\mathrm{d}W^c_{ij}}{\mathrm{d}t} \ , \tag{6.7}$$

and

$$\xi^a_{ij} = \frac{\mathrm{d}W^a_{ij}}{\mathrm{d}t} \ . \tag{6.8}$$

Again, the following relations hold for the white noise processes

$$\begin{aligned} \left\langle \xi^c_{ij}(t) \right\rangle &= 0 \ , \\ \left\langle \xi^c_{ij}(\tau_1) \xi^c_{ij}(\tau_2) \right\rangle &= \delta(\tau_1 - \tau_2) \ , \end{aligned} \tag{6.9}$$

with $\xi^c_{ij} = -\xi^c_{ji}$, and similar relations hold for ξ^a_{ij}. With this definition for the noise, the overall quantity of both species is strictly conserved during the dynamics, an important consequence being the conservation of the total charge during the dynamics of the system. The dynamics of ionic fluxes between particles is sketched in fig. 6.1.

6.2 Equilibrium solution

Equation (6.1) can be written in the compact form of a Langevin equation

$$\dot{\boldsymbol{y}} = \boldsymbol{u}(\boldsymbol{y}) + \boldsymbol{G}(\boldsymbol{y})\boldsymbol{\xi} \ , \tag{6.10}$$

where, employing a compact notation here and in the following,

$$\boldsymbol{y} = (\boldsymbol{x}_1, \ldots, \boldsymbol{x}_N, \boldsymbol{v}_1, \ldots, \boldsymbol{v}_N, n_1^c, \ldots, n_N^c, n_1^a, \ldots, n_N^c)^T = (\boldsymbol{x}_i, \boldsymbol{v}_i, n_i^c, n_i^a)^T \tag{6.11}$$

is the state vector which has dimension $8N$, and $i \in [1, N]$. The drift $\boldsymbol{u} = (\boldsymbol{u}_i^x, \boldsymbol{u}_i^v, u_i^c, u_i^a)^T$ is composed by the deterministic terms in eq. (6.1)

$$\boldsymbol{u}(\boldsymbol{y}) = \begin{pmatrix} \boldsymbol{v}_i \\ m^{-1}\boldsymbol{F}_i^C + m^{-1}\sum\limits_{j\neq i} \gamma w_D(r_{ij})\left(\boldsymbol{v}_{ji}\cdot\boldsymbol{e}_{ij}\right)\boldsymbol{e}_{ij} \\ \sum\limits_{j\neq i}\left[\gamma^c w_D(r_{ij})\mu_{ji}^c + w^D(r_{ij})h_{ij}^c\right] \\ \sum\limits_{j\neq i}\left[\gamma^a w_D(r_{ij})\mu_{ji}^a + w^D(r_{ij})h_{ij}^a\right] \end{pmatrix} . \tag{6.12}$$

The stochastic vector $\boldsymbol{\xi} = (\boldsymbol{\xi^v}, \boldsymbol{\xi^c}, \boldsymbol{\xi^a})^T$ is composed of independent Wiener processes and has dimension $3N(N-1)/2$, i.e. three times the total number of particle pairs. The matrix $\boldsymbol{G}$ has therefore dimension $8N \times 3N(N-1)/2$, and is composed by the following blocks

$$\boldsymbol{G}(\boldsymbol{y}) = \begin{pmatrix} \boldsymbol{0} & \boldsymbol{0} & \boldsymbol{0} \\ \boldsymbol{G^v} & \boldsymbol{0} & \boldsymbol{0} \\ \boldsymbol{0} & \boldsymbol{G^c} & \boldsymbol{0} \\ \boldsymbol{0} & \boldsymbol{0} & \boldsymbol{G^a} \end{pmatrix} . \tag{6.13}$$

The matrix $\boldsymbol{G^v}$ has dimension $3N \times N(N-1)/2$ and can be written in a compact form as $\boldsymbol{G}_{i\alpha}^{\boldsymbol{v}} = m^{-1} f_{i\alpha}\sigma w^R(r_\alpha)\boldsymbol{e}_\alpha$, where α is an index which spans all the particle pairs, i.e. $\alpha = (i', j')$ with $i' \in [1, N-1]$ and $j' \in [i'+1, N]$, in such a way that $\dot{\boldsymbol{v}}_i = \boldsymbol{u}_i^{\boldsymbol{v}} + \sum\limits_\alpha \boldsymbol{G}_{i\alpha}^{\boldsymbol{v}}\boldsymbol{\xi}_\alpha^{\boldsymbol{v}}$. Hence, $r_\alpha = r_{i'j'}$, $\boldsymbol{e}_\alpha = \boldsymbol{e}_{i'j'}$ and $f_{i\alpha}$

is such that

$$f_{i\alpha} = \begin{cases} 0 & \text{if } i \neq i' \text{ and } i \neq j' \ , \\ 1 & \text{if } i = i' \ , \\ -1 & \text{if } i = j' \ . \end{cases} \tag{6.14}$$

The matrices $\boldsymbol{G^c}$ and $\boldsymbol{G^a}$ have dimension $N \times N(N-1)/2$ and their components are, respectively, $G^c_{i\alpha} = f_{i\alpha}\sigma^c w^R(r_\alpha)$ and $G^a_{i\alpha} = f_{i\alpha}\sigma^a w^R(r_\alpha)$. Once defined the vectors $\boldsymbol{y}$, $\boldsymbol{u}$ and $\boldsymbol{\xi}$ and the matrix $\boldsymbol{G}$, the Fokker-Planck equation associated with eq. (6.10) can be written as (see Section 2.1)

$$\frac{\partial P(\boldsymbol{y},t)}{\partial t} = \boldsymbol{\nabla_y} \cdot \left[\left(-\boldsymbol{u} + \frac{1}{2}\boldsymbol{\nabla_y} \cdot \boldsymbol{G}\boldsymbol{G}^T + \frac{1}{2}\boldsymbol{G}\boldsymbol{G}^T\boldsymbol{\nabla_y} \right) P(\boldsymbol{y}) \right] \ . \tag{6.15}$$

In the following, the operator $\boldsymbol{\nabla_y}$ will be represented simply as $\boldsymbol{\nabla}$. It is convenient to introduce the matrix $\boldsymbol{D} = \boldsymbol{G}\boldsymbol{G}^T/2$, which has dimension $8N \times 8N$ and can be decomposed in blocks

$$\boldsymbol{D} = \begin{pmatrix} \boldsymbol{0} & \boldsymbol{0} & \boldsymbol{0} & \boldsymbol{0} \\ \boldsymbol{0} & \boldsymbol{D^v} & \boldsymbol{0} & \boldsymbol{0} \\ \boldsymbol{0} & \boldsymbol{0} & \boldsymbol{D^c} & \boldsymbol{0} \\ \boldsymbol{0} & \boldsymbol{0} & \boldsymbol{0} & \boldsymbol{D^a} \ , \end{pmatrix} \tag{6.16}$$

with

$$\begin{aligned} \boldsymbol{D^v_{ij}} =& \frac{1}{2}\sum_\alpha \boldsymbol{G^v_{i\alpha}} \otimes \boldsymbol{G^v_{j\alpha}} = \frac{1}{2m^2}\sum_\alpha f_{i\alpha}f_{j\alpha}\left(\sigma w^R(r_\alpha)\right)^2 \boldsymbol{e}_\alpha \otimes \boldsymbol{e}_\alpha \ , \\ D^c_{ij} =& \frac{1}{2}\sum_\alpha G^c_{i\alpha}G^c_{j\alpha} = \frac{1}{2}\sum_\alpha f_{i\alpha}f_{j\alpha}\left(\sigma^c w^R(r_\alpha)\right)^2 \ , \\ D^a_{ij} =& \frac{1}{2}\sum_\alpha G^a_{i\alpha}G^a_{j\alpha} = \frac{1}{2}\sum_\alpha f_{i\alpha}f_{j\alpha}\left(\sigma^a w^R(r_\alpha)\right)^2 \ , \end{aligned} \tag{6.17}$$

where there is an implied summation between the pairs α. These expressions can be simplified observing that the action of the product $f_{i\alpha}f_{j\alpha}$ on the

summation is different in the two cases $i = j$ and $i \neq j$. In the first case, the product $f_{i\alpha}f_{i\alpha}$ equals 1 for all the pairs of particles involving particle i, and vanishes for all the other pairs. In the second case, the product $f_{i\alpha}f_{j\alpha}$ is -1 for the pair i, j and 0 for all the other pairs. With this in mind, the expressions for the blocks of matrix $\boldsymbol{D}$ are

$$\begin{aligned}
\boldsymbol{D}^v_{ij} =& \frac{1}{2m^2}\delta_{ij}\sum_k \left[\left(\sigma w^R(r_{ik})\right)^2 \boldsymbol{e}_{ik}\otimes\boldsymbol{e}_{ik}\right] + \frac{1}{2m^2}\left(\delta_{ij}-1\right)\left(\sigma w^R(r_{ij})\right)^2 \boldsymbol{e}_{ij}\otimes\boldsymbol{e}_{ij} \ , \\
D^c_{ij} =& \frac{1}{2}\delta_{ij}\sum_k \left(\sigma^c w^R(r_{ik})\right)^2 + \frac{1}{2}\left(\delta_{ij}-1\right)\left(\sigma^c w^R(r_{ij})\right)^2 \ , \\
D^a_{ij} =& \frac{1}{2}\delta_{ij}\sum_k \left(\sigma^a w^R(r_{ik})\right)^2 + \frac{1}{2}\left(\delta_{ij}-1\right)\left(\sigma^a w^R(r_{ij})\right)^2 \ ,
\end{aligned} \tag{6.18}$$

where in the first terms of the three expressions there is an implied summation on the particle index k. Let's assume that the dynamics generated by eq. (6.10) is such that an equilibrium distribution exists in the form

$$P_{eq}(\boldsymbol{y}) \propto \exp\left(S(\boldsymbol{y})\right) \ , \tag{6.19}$$

where S is an appropriate thermodynamic potential as a function of the coarse-grained variables. In the present model, since we are dealing with an isolated system, S is the entropy of the system, the Boltzmann's constant assumed to be $k_B = 1$. Imposing that the distribution of eq. (6.19) is the solution of the Fokker-Planck eq. (6.15) and using the notation with matrix $\boldsymbol{D}$ leads to

$$0 = \boldsymbol{\nabla}\cdot\left[\left(-\boldsymbol{u} + \boldsymbol{\nabla}\cdot\boldsymbol{D} + \boldsymbol{D}\boldsymbol{\nabla}S\right)P_{eq}(\boldsymbol{y})\right] \ , \tag{6.20}$$

It is now convenient to separate the drift term into two parts, i.e. $\boldsymbol{u} = \boldsymbol{u_C} + \boldsymbol{u_D}$, the conservative drift $\boldsymbol{u_C}$ and the dissipative drift $\boldsymbol{u_D}$, where

$$\boldsymbol{u_C} = \begin{pmatrix} \boldsymbol{v}_i \\ m^{-1}\boldsymbol{F}_i^C \\ 0 \\ 0 \end{pmatrix} , \tag{6.21}$$

and

$$\boldsymbol{u_D} = \begin{pmatrix} 0 \\ m^{-1}\sum_{j\neq i} \gamma w_D(r_{ij})\left(\boldsymbol{v}_{ji}\cdot\boldsymbol{e}_{ij}\right)\boldsymbol{e}_{ij} \\ \sum_{j\neq i} \gamma^c w_D(r_{ij})\mu^c_{ji} \\ \sum_{j\neq i} \gamma^a w_D(r_{ij})\mu^a_{ji} \end{pmatrix} . \tag{6.22}$$

The conservative drift gives no contribution to the equilibrium Fokker-Planck equation (6.20) if the two following conditions are met

$$\frac{\partial S}{\partial \boldsymbol{x}_i} = \beta \boldsymbol{F}_i^{\boldsymbol{C}} , \tag{6.23}$$

$$\frac{\partial S}{\partial \boldsymbol{v}_i} = -\beta m \boldsymbol{v}_i , \tag{6.24}$$

where $\beta = T^{-1}$. Here it is assumed that the temperature is homogeneous in all the system, all the particles having the same thermal energy. Using the conditions of Eq. (6.23) and Eq. (6.24), the conservative drift $\boldsymbol{u^C}$ gives no contribution to Eq. (6.20), i.e.

$$\boldsymbol{\nabla}\cdot(\boldsymbol{u_C}P_{eq}) = \left(\boldsymbol{\nabla}\cdot\boldsymbol{u_C} + \boldsymbol{u_C}\cdot\boldsymbol{\nabla}S\right)P_{eq} = \beta\left(\boldsymbol{v}\cdot\boldsymbol{F}^C - m^{-1}\boldsymbol{F}^C\cdot m\boldsymbol{v}\right)P_{eq} = 0 . \tag{6.25}$$

Equation (6.23) specifies the conservative force once the function S is chosen, while eq. (6.24) is a condition which has to be taken into account when

the function S has to be modelled. Since the conservative drift gives no contribution, Equation (6.20) is identically satisfied if

$$\boldsymbol{u_D} = \boldsymbol{\nabla} \cdot \boldsymbol{D} + \boldsymbol{D}\boldsymbol{\nabla} S \; . \tag{6.26}$$

This equation gives a condition for the Fokker-Planck equation (6.15) to have the equilibrium solution of eq. (6.19) with S satisfying eq. (6.23) and eq. (6.24). In order to explicitly write the dissipative drift as prescribed by eq. (6.26), it is useful to decompose it into its four subvectors, i.e. $\boldsymbol{u_D} = \left(\boldsymbol{u_D^x}, \boldsymbol{u_D^v}, \boldsymbol{u_D^c}, \boldsymbol{u_D^a}\right)^T$. The equation for the first subvector is trivial, giving $\boldsymbol{u_D^x} = 0$. The equation for the second subvector can be explicitly computed considering the expression of $\boldsymbol{D_{ij}^v}$ of eq. (6.18)

$$\boldsymbol{u_{Di}^v} = \frac{1}{2m^2}\left(\sigma w^R(r_{ij})\right)^2 \boldsymbol{e}_{ij}\otimes\boldsymbol{e}_{ij}\left(\frac{\partial S}{\partial \boldsymbol{v}_i} - \frac{\partial S}{\partial \boldsymbol{v}_j}\right) = \frac{\beta}{2m}\left(\sigma w^R(r_{ij})\right)^2 \left(\boldsymbol{v}_{ji}\cdot\boldsymbol{e}_{ij}\right)\boldsymbol{e}_{ij} \; , \tag{6.27}$$

where there is an implied summation on the index j and eq. (6.24) has been used. It can be seen by comparing eq. (6.27) with eq. (6.22) that the two terms are equal if two conditions are met

$$\begin{aligned} \gamma &= \frac{\beta\sigma^2}{2} \; , \\ w^D(r) &= \left(w^R(r)\right)^2 \; . \end{aligned} \tag{6.28}$$

If these two condition are satisfied, the Fokker Planck equation (6.15) has the Boltzmann distribution of eq. (6.19) as equilibrium solution in absence of any ionic exchange between particles. These are the same conditions found by Español and Warren [64] for the classical DPD model.

The two remaining components of the dissipative drift in eq. (6.26) read

$$\begin{aligned} u^c_{Di} &= \frac{1}{2}\left(w^R(r_{ij})\right)^2\left(\frac{\partial\left(\sigma^c\right)^2}{\partial n^c_i}-\frac{\partial\left(\sigma^c\right)^2}{\partial n^c_j}\right)+\frac{1}{2}\left(\sigma^c w^R(r_{ij})\right)^2\left(\frac{\partial S}{\partial n^c_i}-\frac{\partial S}{\partial n^c_j}\right)\,, \\ u^a_{Di} &= \frac{1}{2}\left(w^R(r_{ij})\right)^2\left(\frac{\partial\left(\sigma^a\right)^2}{\partial n^a_i}-\frac{\partial\left(\sigma^a\right)^2}{\partial n^a_j}\right)+\frac{1}{2}\left(\sigma^a w^R(r_{ij})\right)^2\left(\frac{\partial S}{\partial n^a_i}-\frac{\partial S}{\partial n^a_j}\right)\,, \end{aligned} \tag{6.29}$$

where there is an implied summation on the index j. Using the condition of eq. (6.28) for the weight functions and defining the chemical potential of particle i as

$$\begin{aligned} \mu^c_i &= -\frac{1}{\beta}\frac{\partial S}{\partial n^c_i}\,, \\ \mu^a_i &= -\frac{1}{\beta}\frac{\partial S}{\partial n^a_i}\,, \end{aligned} \tag{6.30}$$

equations (6.29) can be rewritten as

$$\begin{aligned} u^c_{Di} &= \frac{1}{2}w^D(r_{ij})\left(\frac{\partial\left(\sigma^c\right)^2}{\partial n^c_i}-\frac{\partial\left(\sigma^c\right)^2}{\partial n^c_j}\right)+\frac{\beta}{2}\left(\sigma^c\right)^2 w^D(r_{ij})\mu^c_{ji}\,, \\ u^a_{Di} &= \frac{1}{2}w^D(r_{ij})\left(\frac{\partial\left(\sigma^a\right)^2}{\partial n^a_i}-\frac{\partial\left(\sigma^a\right)^2}{\partial n^a_j}\right)+\frac{\beta}{2}\left(\sigma^a\right)^2 w^D(r_{ij})\mu^a_{ji}\,. \end{aligned} \tag{6.31}$$

If the quantities γ_c, γ_a, σ_c and σ_a are constant parameters, the first terms on the left side ef eqs. 6.31 vanish, giving

$$\begin{aligned} u^c_{Di} &= \frac{\beta}{2}\left(\sigma^c\right)^2 w^D(r_{ij})\mu^c_{ji}\,, \\ u^a_{Di} &= \frac{\beta}{2}\left(\sigma^a\right)^2 w^D(r_{ij})\mu^a_{ji}\,. \end{aligned} \tag{6.32}$$

Comparing eq. (6.32) with eq. (6.22) leads to two additional fluctuation-dissipation conditions

$$\begin{aligned} \sigma^c &= \sqrt{\frac{2\gamma^c}{\beta}} \\ \sigma^a &= \sqrt{\frac{2\gamma^a}{\beta}}\,. \end{aligned} \tag{6.33}$$

Such conditions specify the form of σ^c and σ^a once given the dissipative factors γ^c and γ^a. If the dissipative factors are not constant but depend on the quantity of cations and ions carried by the particles i and j, it can be seen from eq. (6.31) that the additional drift h_{ij} is not zero anymore and reads

$$\begin{aligned} h_{ij}^c &= w^D(r_{ij})\frac{1}{\beta}\left(\frac{\partial\gamma^c}{\partial n_i^c} - \frac{\partial\gamma^c}{\partial n_j^c}\right) \\ h_{ij}^a &= w^D(r_{ij})\frac{1}{\beta}\left(\frac{\partial\gamma^a}{\partial n_i^a} - \frac{\partial\gamma^a}{\partial n_j^a}\right) \ , \end{aligned} \tag{6.34}$$

where equation (6.33) has been used.

6.3 Model for the dynamics of the system

In the previous section it was shown that if the conditions of Eqs. (6.33), Eqs. (6.28), Eqs. (6.34), Eq. (6.23) and Eq. (6.24) are met, the system of equations (6.1) admits a stationary equilibrium solution with the form given by (6.19) such that the conservative force $\boldsymbol{F}^C$, the particle velocity $\boldsymbol{v_i}$ and the chemical potentials μ_i^c and μ_i^a are related to the entropy of the system S by eq. (6.23), eq. (6.24), and eqs. (6.30). Considering the whole system to be isolated and constituted by particles which represent portions of the system locally at the thermodynamic equilibrium, the system total energy E_{TOT} is constant and reads

$$E_{TOT} = U_E + \sum_{i=1}^{N}\left(\frac{m}{2}\boldsymbol{v_i}\cdot\boldsymbol{v_i} + U_i\right) \ , \tag{6.35}$$

where U_E is the electrostatic energy of the system due to the interactions of charged particles, and the summation includes the kinetic energy of particle i $m/2\boldsymbol{v_i}\cdot\boldsymbol{v_i}$ and the internal energy of particle i U_i. Introducing the Helmhotz

free energy of the particle A_i, the entropy of particle i can be expressed as

$$S_i = \beta \left(U_i - A_i \right) \ . \tag{6.36}$$

Hence, the total entropy reads

$$S = \sum_{i=1}^{N} S_i = \sum_{i=1}^{N} \beta \left(U_i - A_i \right) = \beta \left[E_{TOT} - U_E - \sum_{i=0}^{N} \left(A_i + \frac{m}{2} \boldsymbol{v_i} \cdot \boldsymbol{v_i} \right) \right] \ , \tag{6.37}$$

where eq. (6.35) has been used. Since E_{TOT} is a constant, to define S only the free energy A_i and the electrostatic energy U_E are still to be specified as a function of the coarse-grained variables. In order to complete the definition of A_i, the particle volume has to be defined as a function of the position of the coarse grained particles. It is convenient to define the inverse volume of the particle as a sum over particle pairs of a funcion of their relative distances (e.g. see other DPD derived techniques such as Smoothed Dissipative Particle Dynamics [68])

$$\frac{1}{V_i} = \sum_{j=1}^{N} w(r_{ij}) \ , \tag{6.38}$$

where the function $w(r)$ can be any positive differentiable function having a maximum in $r = 0$, normalized to 1, and such that $w(r) = 0$ if r is larger than a cutoff r_c. Here, the function w^D as defined in eq. (6.4) is used $w(r) = w_0 w^D(r)$, where $w_0 = 15/2\pi$ is a normalization factor. With this definition of particle volume, it is possible to formulate an expression for A_i using the tools of statistical mechanics.

6.3.1 Free energy model

In order to consistently choose the free energy of the particle A_i as a function of the coarse-grained variables, some assumptions on the nature of the microscopic atomistic system represented by particle i might be done. Here, the coarse-grained particle i is considered to be constituted by M atomistic-scale particles of three different kind and equal mass. The three kind of particles are the cations n^c, the anions n^a and neutral (solvent) particles n^n. The proportion of cations, anions and neutral particles may change during the dynamics, but their sum remains constant, i.e.

$$n^c + n^a + n^n = M = \text{const} \, . \tag{6.39}$$

This assumption is consistent with the fact that the coarse-grained particles have a constant mass. The simplest expression for A_i can be obtained considering the Helmhotz free energy of a system composed by three non interacting species [104]

$$A = \frac{n^c}{\beta}\left[\log\left(\frac{n^c\lambda}{V}\right) - 1\right] + \frac{n^a}{\beta}\left[\log\left(\frac{n^a\lambda}{V} - 1\right)\right] + \frac{n^n}{\beta}\left[\log\left(\frac{n^n\lambda}{V}\right) - 1\right] , \tag{6.40}$$

where λ is a constant parameter. In such a system, the Helmhotz free energy is a function of the volume V, the temperature T, n^c, n^a and n^n. However, the dependence on n^n and T may be dropped, the first because of the constraint of eq. (6.39), the second because as already pointed out T is assumed to be constant during the dynamics for all the coarse-grained particles. The dependence on volume of A_i can be converted in a dependence on the density

ρ_i, as defined in eq. (6.38), i.e.

$$A_i(V_i, n_i^c, n_i^a) = \frac{n^c}{\beta} \log\left(\frac{n^c}{M - n^c - n^a}\right) + \frac{n^a}{\beta} \log\left(\frac{n^a}{M - n^c - n^a}\right) + \frac{M}{\beta} \log\left[\frac{(M - n^a - n^c)\,\lambda}{V_i}\right] , \tag{6.41}$$

where the constant terms have been omitted. The solvent particles disappear from the free energy definition due to the constraint (6.39), and the only effect of their presence is to introduce a parameter M in the free energy which can be tuned to modify the pressure of the system.

6.3.2 Electrostatics

In order to complete the expression for the entropy of eq. (6.37), the electrostatic energy is the last term to be specified. The coarse-grained variables n^c and n^a are associated to the quantity of cations and ions carried by the particle i, and hence to its charge, i.e.

$$q_i = Z_c n_i^c - Z_a n_i^a , \tag{6.42}$$

where Z_c and Z_a are, respectively, the charge of the single cation and anion. However, such quantities do not provide any information on how the charge is distributed within the particle volume. A possible approach could be to assume all the ions are distributed at the center of the particles, i.e. to treat the particles as point charges interacting via a Coulomb potential. If such approach is adopted, the particles could interact very strongly since there is no constraint or strongly repulsive force which prevents the interparticle distance to be extremely small. In addition, the aim of coarse graining is not only to reduce the degrees of freedom of the system, but also to smooth down the sharp potentials acting in all-atoms methods. With this in mind,

the charge distribution associated to a particle i of charge q_i has been chosen as a Gaussian distribution centered in $\boldsymbol{x}_i$ and with variance s, i.e.

$$\rho_i(\boldsymbol{r}) = \rho(\boldsymbol{r}, \boldsymbol{x}_i, q_i) = \frac{q_i}{(2\pi s^2)^{3/2}} \exp \frac{-|\boldsymbol{r} - \boldsymbol{x_i}|^2}{2s^2} \ , \tag{6.43}$$

where $\boldsymbol{r}$ is the generic position in the physical space. The electrostatic energy arising from the interaction of two such distributions is [105]

$$U_{ij}^E = \int \int \frac{\rho_i(\boldsymbol{r})\rho_j(\boldsymbol{r'})}{|\boldsymbol{r} - \boldsymbol{r'}|} \mathrm{d}\boldsymbol{r}\mathrm{d}\boldsymbol{r'} = \frac{q_i q_j}{r_{ij}} \operatorname{erf}\left(\frac{r_{ij}}{2s}\right) \tag{6.44}$$

if $i \neq j$. In the case $i = j$ the self-energy of the Gaussian distribution is

$$U_{ii}^E = \frac{1}{2} \int \int \frac{\rho_i(\boldsymbol{r})\rho_i(\boldsymbol{r'})}{|\boldsymbol{r} - \boldsymbol{r'}|} \mathrm{d}\boldsymbol{r}\mathrm{d}\boldsymbol{r'} = \frac{q_i^2}{2s\sqrt{\pi}} \ . \tag{6.45}$$

The self-energy of the distribution does not appear in the electrostatic force, but it still modifies the electrostatic potential. The electrostatic potential of particle i is defined as

$$\Phi_i = \frac{\partial U^E}{\partial q_i} = \frac{q_i}{s\sqrt{\pi}} + \sum_{i \neq j}^{N} \frac{q_j}{r_{ij}} \operatorname{erf}\left(\frac{r_{ij}}{2s}\right) \ . \tag{6.46}$$

With this choice, the electrostatic energy can be expressed as

$$U_E = \frac{1}{2} \sum_{i=0}^{N} q_i \Phi_i \tag{6.47}$$

Using the fact that $\lim_{r \to 0} \operatorname{erf}(r/(2s))/r = 1/(s\sqrt{\pi})$, the potential of the particle can be rewritten as

$$\Phi_i = \sum_{j=0}^{N} \frac{q_j}{r_{ij}} \operatorname{erf}\left(\frac{r_{ij}}{2s}\right) \ , \tag{6.48}$$

where now the summation includes the term $j = i$ for which $r_{ij} = 0$.

6.3.3 Chemical potential and conservative force

The definition of electrostatic energy completes the expression of the entropy (eq. (6.37)), allowing the calculation of the chemical potential as defined in eq. (6.30). The chemical potential for the cations and the anions results

$$\begin{aligned}\mu_i^c &= -\frac{1}{\beta}\frac{\partial S}{\partial n_i^c} = \frac{\partial\left(A_i + U_E\right)}{\partial n_i^c} = \frac{1}{\beta}\log\left(\frac{n^c}{M - n^c - n^a}\right) + Z_c\Phi_i \ , \\ \mu_i^a &= -\frac{1}{\beta}\frac{\partial S}{\partial n_i^a} = \frac{\partial\left(A_i + U_E\right)}{\partial n_i^a} = \frac{1}{\beta}\log\left(\frac{n^a}{M - n^c - n^a}\right) - Z_a\Phi_i \ .\end{aligned} \tag{6.49}$$

the chemical potential has a contribution which is independent on the electrostatic interactions and a contribution due to the electrostatic interactions which is proportional to the electrostatic potential. The conservative force is also obtained by differentiating the entropy S (see Eq. (6.23))

$$\boldsymbol{F}_i^{\boldsymbol{C}} = \frac{1}{\beta}\frac{\partial S}{\partial \boldsymbol{x_i}} = -\frac{\partial\left(U_E + A\right)}{\partial \boldsymbol{x_i}} = \boldsymbol{F}_i^{\boldsymbol{E}} + \boldsymbol{F}_i^{\boldsymbol{P}} \ , \tag{6.50}$$

where $A = \sum_{j=1}^{N} A_j$ is the total free energy of the system. It emerges that the conservative force has two terms, an electrostatic force $\boldsymbol{F}_i^{\boldsymbol{E}}$ due to the change of electrostatic energy of the particle and a pressure force $\boldsymbol{F}_i^{\boldsymbol{P}}$ due to the change in volume (and hence of free energy) of the particle. The electrostatic force can be computed using Eq. (6.47) and Eq. (6.46) for U_E, giving

$$\boldsymbol{F}_i^{\boldsymbol{E}} = -\sum_{j\neq i} q_i \frac{\partial\Phi_i}{\partial r_{ij}}\boldsymbol{e}_{ij} = \sum_{j\neq i} q_i q_j \frac{\sqrt{\pi}s\,\mathrm{erf}\left(r_{ij}/(2s)\right) - r_{ij}\exp\left(-r_{ij}^2/(4s^2)\right)}{s\sqrt{\pi}r_{ij}^2}\boldsymbol{e}_{ij} \ . \tag{6.51}$$

The pressure force can be computed using Eq. (6.41) for A, giving

$$\boldsymbol{F}_i^{\boldsymbol{P}} = -\sum_j \frac{\partial A_j}{\partial V_j}\frac{\partial V_j}{\partial \boldsymbol{x_i}} = \sum_{j\neq i} \frac{2w_0 M}{r_c\beta}\left(V_j + V_i\right) w^R(r_{ij})\boldsymbol{e}_{ij} \ , \tag{6.52}$$

where Eq. (6.38) has been used.

6.3.4 Dissipative factors

The dissipative factors γ^c and γ^a control the quantity of ions exchanged between two particles due to a chemical potential difference μ_{ij}, and are linked to the noise intensities σ^c and σ^a and to the additional drift h^c and h^a via the fluctuation-dissipation relations of eq. (6.33). As these functions do not appear in the entropy, the equilibrium distribution is not affected by their expression. Instead, such functions are expected to control the ionic mobility, i.e. the ionic flux caused by a chemical potential difference, and as a consequence, the conductivity of the solution. If γ^c and γ^a are taken to be constant, the resulting conductivity is independent on the electrolyte concentration, which is generally not true. In order to model a more realistic conductivity two conditions are reasonable

1. The functions γ^c and γ^a increase linearly with the averge quantities of cations or anions in the two particles i and j, i.e $\gamma^{c/a}(\lambda n_i^c, \lambda n_j^c) = \lambda\gamma^{c/a}(n_i^c, n_j^c)$.

2. If the number of ions in one of the particles goes to zero, the stochastic flux between them, and hence σ^c, also go to zero.

A functional form for γ_c and γ_a which satisfies both conditions is

$$\begin{aligned} \gamma^c(n_i^c, n_j^c) &= \gamma_0^c\sqrt{n_i^c n_j^c} \\ \gamma^a(n_i^a, n_j^a) &= \gamma_0^a\sqrt{n_i^a n_j^a}\ . \end{aligned} \tag{6.53}$$

In section 7.2.1 is shown that these choices for the ionic exchange functions leads to a conductivity linearly dependent on the electrolyte concentration,

a realistic condition when dealing with low concentrated solutions [106]. The fluctuation-dissipation relations of eqs. (6.33) then provide the expressions for σ^c and σ^a

$$\begin{aligned} \sigma^c(n_i^c, n_j^c) &= \sqrt{\frac{2\gamma_0^c \sqrt{n_i^c n_j^c}}{\beta}} \\ \sigma^a(n_i^a, n_j^a) &= \sqrt{\frac{2\gamma_0^a \sqrt{n_i^a n_j^a}}{\beta}} \end{aligned} \tag{6.54}$$

and for h_c and h_a

$$\begin{aligned} h_c(n_i^c, n_j^c) &= \frac{\gamma_0^c}{\beta}\left(\sqrt{\frac{n_j^c}{n_i^c}} - \sqrt{\frac{n_i^c}{n_j^c}}\right) \\ h_a(n_i^a, n_j^a) &= \frac{\gamma_0^a}{\beta}\left(\sqrt{\frac{n_j^a}{n_i^a}} - \sqrt{\frac{n_i^a}{n_j^a}}\right) \end{aligned} \tag{6.55}$$

Chapter 7

Model validation

In this chapter, the testing and validation of the model presented in Chapter 6 is reported. After giving a few details about the implementation of the model, a bulk electrolyte under the action of a constant electric field is simulated as a first test. These simulations show that, as observed in standard DPD for the viscosity of the fluid, the transport coefficients can be controlled changing the magnitude of the dissipative and stochastic forcing in the evolution equations (i.e. the dissipative parameters γ_0^c and γ_0^a). In particular, the mobility of cations or anions can be tuned by calibrating the parameters controlling the dissipative and stochastic ion exchange between particles. As a case of study to validate the model, a system consisting of a planar channel with given surface charge at the boundaries is set up. Different settings of this kind of system (surface charges with the same or opposite size, different surface charges and ionic charges) are simulated and compared with analytical solutions based on the Debye approximation, showing an excellent agreement.

7.1 Model implementation

In Chapter 6 it was shown that the system of Eq. (6.1) equipped with the conditions given by Eqs. (6.28), Eqs. (6.33) and Eqs. (6.34) admits an equilibrium solution of the form (6.19) if S is such that Eq. (6.23) and Eq. (6.24) are verified. In addition, the selected model for the conservative force between particles $\boldsymbol{F^C}$ and the chemical potentials $\boldsymbol{\mu^c}$ and $\boldsymbol{\mu^a}$ had been described. The free parameters of the model are the dissipative parameters γ, γ_0^c and γ_0^a, the variance of the Gaussian used to model the electrostatic interactions s, the free energy parameter M and the ionic charges Z_c and Z_a. The model was implemented in the LAMMPS software [107] as a modification of the DPD package. The Euler-Maruyama algorithm [90] was used to integrate Eq. (6.1) in the Itô formalism. In order to compute electrostatic forces and potentials the Coulombic interactions between charged parts of the system have to be considered. Such interactions are long-ranged (i.e. they vanish slower than r^{-3}, where r is the distance between the considered parts of the system), and the accurate and efficient computation of such interactions is a well-known problem in Molecular Dynamics simulations [108]. One of the techniques used to compute the electrostatic interactions in systems of charged particles is the Ewald summation [109]. The original Ewald summation deals with distributions of point charges, here it is used in a modified form as formulated by Kiss et al. [105] which is suitable in the case of the interaction of Gaussian distributions.

In the set of Eqs. (6.1) there is no guarantee that the quantity n^c and n^a is positive. In fact, due to the stochastic nature of the equations, improbable

but strong events can cause a negative quantity of ions in the particle. To avoid this problem, a natural way is to increase the total ions in the system, which is established by the initial conditions. The larger is the average ion quantity in the particles, the lower is the probability of having a negative number of ions at some point of the simulation. However, since both the chemical potential of Eq. (6.49) and the dissipative factors γ^a and γ^c of Eqs. (6.34) are not defined for negative values of n_i^a and n_i^b, a low limiting value of $\bar{n}$ is considered such that in the improbable case that $n_i^a < \bar{n}$ or $n_i^c < \bar{n}$, then $\bar{n}$ is used instead in Eq. (6.49) and Eqs. (6.34). A value of $\bar{n} = 0.018$ has been used in all the simulations reported in this Chapter, and it has been verified that changing $\bar{n} \in [0.01, 0.03]$ does not affect the output of the simulation in a detectable way. In the rest of the present Chapter all the units will be expressed non-dimensionally taking as a reference length the cutoff of the particle interaction $L_{ref} = r_c$, as a reference energy the thermal energy $E_{ref} = \beta^{-1}$ and as a reference mass the mass of the particles $M_{ref} = m$. The dielectric constant is always $\varepsilon = (4\pi)^{-1}$. For all the simulations here reported, the time step is $\Delta t = 10^{-4}$, the fluid has a density of particles $\rho = 3$, the variance of the Gaussian used for the electrostatic interactions is $s = 0.4$, the free energy parameter is $M = 75$ and $\gamma = 500$.

7.2 Bulk fluid under constant electric field

As a first test, a triperiodic cubic box of size $L = 10$ was simulated with a constant external electric field E applied along the direction $\hat{z}$. The external electric field introduces an additional electrostatic energy for each particle

$U^{EXT} = q_i E z$. This has three implications on the equations of motion:

- An external force appears $\boldsymbol{F_i^{EXT}} = q_i E \hat{\boldsymbol{z}}$.
- The chemical potential for the cations is modified, adding the term $\Delta\mu_i^c = Z_c E z$.
- Also the chemical potential for the anions is modified, $\Delta\mu_i^a = -Z_a E z$.

The electric field generates a net flow of cations and anions, respectively j_z^c and j_z^a, which can be measured as a sum of two contributions

$$\begin{aligned} j_z^c &= \sum_{i=0}^{N} \left[n_i^c \boldsymbol{v_i} \cdot \hat{\boldsymbol{z}} + \sum_{j=i+1}^{N} \frac{\Delta n_{ij}^c}{\Delta t} z_{ij} \right] , \\ j_z^a &= \sum_{i=0}^{N} \left[n_i^a \boldsymbol{v_i} \cdot \hat{\boldsymbol{z}} + \sum_{j=i+1}^{N} \frac{\Delta n_{ij}^a}{\Delta t} z_{ij} \right] , \end{aligned} \tag{7.1}$$

where $z_{ij} = z_i - z_j$ and Δn_{ij}^c and Δn_{ij}^a are respectively, the quantity of cations and anions exchanged between particles i and j at a given step. The first contribution is the ionic flux due to the ions carried by a moving particle, while the second term is the ionic flux due to the exchange of ions between particles located at different positions. Once defined the observables j_z^c and j_z^a, the net current flowing in the $\hat{\boldsymbol{z}}$ direction can be obtained as

$$I_z = \frac{1}{L} \left(Z_c j_z^c - Z_a j_z^a \right) . \tag{7.2}$$

This formula allows the computation of the conductivity of the simulated fluid. The simulations reported in this section have $Z_c = Z_a = 0.1$, while the dissipative parameters γ_0^c and γ_0^a are changed to tune the conductivity.

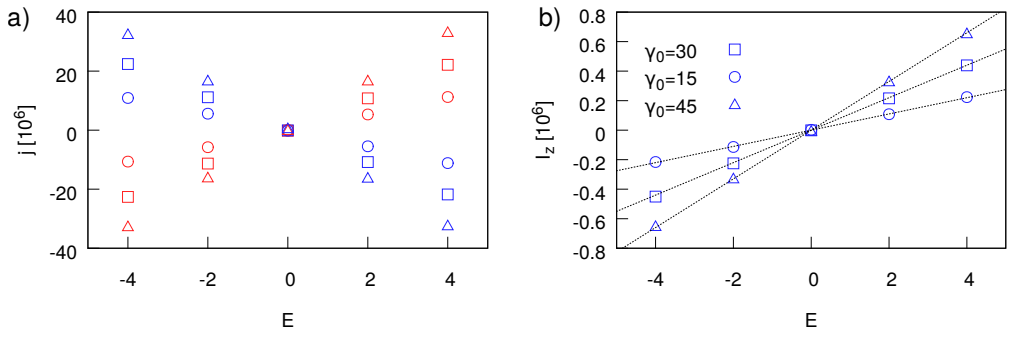

Figure 7.1: Bulk fluid simulation. Case with symmetric ionic mobilities, i.e. $\gamma_0^c = \gamma_0^a = \gamma_0$ (triangles: $\gamma_0 = 45$, squares: $\gamma_0 = 30$, circles: $\gamma_0 = 15$). a)Ionic fluxes for the cationic specie j_z^c (red) and for the anionic specie j_z^a (blue) as a function of the dissipative parameter γ_0. b) Electric current I_z computed as a function of the electric field for different γ_0. The slope of this line is related to the conductivity of the fluid, which results $\kappa \simeq 550$ for $\gamma_0 = 15$, $\kappa \simeq 1100$ for $\gamma_0 = 30$ and $\kappa \simeq 1650$ for $\gamma_0 = 45$.

7.2.1 Conductivity measurement

The conductivity was tuned by changing the dissipative parameters γ_0^c and γ_0^a. In these simulations the initial number of cations and anions was uniformly $n_0 = 10$ in all the particles. As a first case, a solution of ions with symmetric mobilities is considered, i.e. $\gamma_0^c = \gamma_0^a = \gamma_0$. Five different values of γ_0 and E have been considered. The ionic current I_z as well as the fluxes j_z^c and j_z^a computed with Eq. (7.1) and Eq. (7.2) as a function of the electric field for different γ_0 are plotted in Fig. 7.1. It is apparent that both ionic fluxes and the ionic current are linearly dependent on the applied field. The fact that $\gamma_0^c = \gamma_0^a$ guarantees the symmetry of the ionic mobilities and hence the fact that both ionic species contribute to the total ionic current equally. The conductivity of the electrolyte κ is defined as

$$\kappa = \frac{I}{L^2 E} \tag{7.3}$$

The slope of the I-E curve of Fig. 7.1 is hence related to the conductivity of the solution and is found to be linearly dependent on γ_0 for this range of values, with $\kappa \simeq 550$ for $\gamma_0 = 15$, $\kappa \simeq 1100$ for $\gamma_0 = 30$ and $\kappa \simeq 1650$ for $\gamma_0 = 45$. As a second case, a system with non symmetric mobilities was tested, i.e. $\gamma_0^c \neq \gamma_0^a$. In this case, the dissipative parameters have been set to $\gamma^c = 45$ and $\gamma^a = 15$. The same calculations as in the previous symmetric case have been performed and the results are plotted in Fig. 7.2. The ionic fluxes plotted in Fig. 7.2a are not symmetric anymore, thus confirming that the two ionic species have now different mobilities and contribute differently to the total current. The conductivity of the solution is $\kappa \simeq 1100$ as in the symmetric case for $\gamma_0 = 30$, confirming that for the chosen range of values

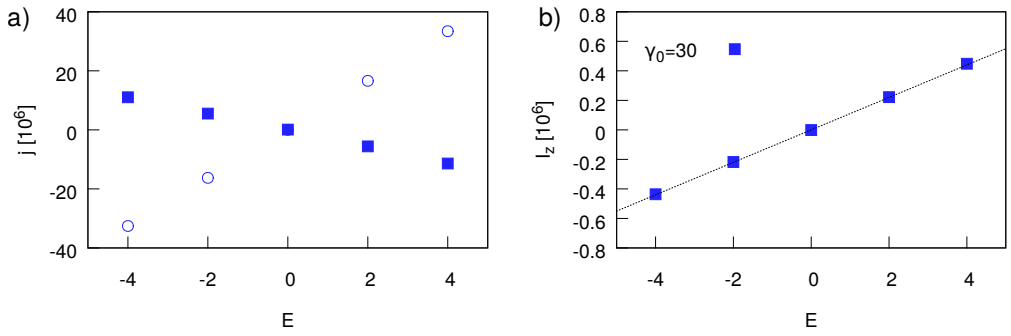

Figure 7.2: Bulk fluid simulation. Case with asymmetric ionic mobilities, i.e. $\gamma_0^c = 45$ and $\gamma_0^a = 15$. a)Ionic fluxes for the cationic specie j_z^c (empty circles) and for the anionic specie j_z^a (full squares) as a function of the dissipative parameter γ_0. b) Electric current I_z computed as a function of the electric field for different γ_0. The slope of this line is related to the conductivity of the fluid, which results $\kappa \simeq 550$.

the change in the dissipative parameters linearly affects the conductivity. In all the simulations reported in this section, there was no net measurable mass flux of the fluid.

7.2.2 Dependence on concentration

The dependence of the conduction properties of the solution on the ionic concentration is also tested. Simulations at five different initial ions per particle n_0 were carried out keeping the dissipative parameter constant, i.e. $\gamma_0^c = \gamma_0^a = \gamma_0 = 30$. Different values of n_0 correspond to different values of average concentration $c_0 = \rho n_0$ where $\rho = 3$ is the particle density. The electric field was $E = 4$ for all the simulations. The ionic current was measured

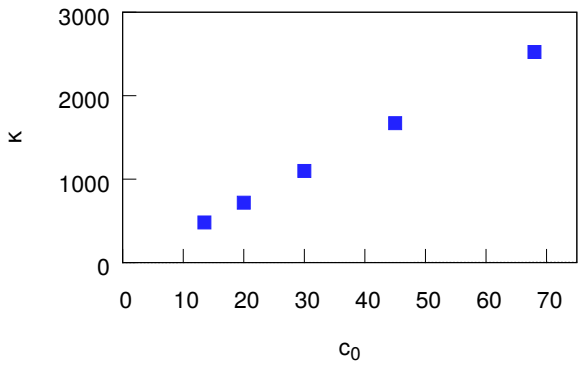

Figure 7.3: Conductance of the solution κ as a function of the concentration $c_0 = \rho n_0$ for $\gamma^a = \gamma^c = 30$ and $E = 4$.

and the conductance was calculated with Eq. (7.3). The results plotted in Fig. 7.3 show a linear dependence of the conductance on the concentration of ions, a realistic condition for diluted solutions. This linear dependence is due to the model chosen for the dissipative factors γ^a and γ^c which are not constant but depend on the number of ions carried by each interacting pair of particles (see Sec. 6.3.4).

7.3 Planar electroosmotic flow

The model has been validated simulating a few electrohydrodynamic systems whose analytical solution under appropriate approximations is known. The system chosen is a planar channel with charged walls containing the solution, being L the separation between charged walls. In such systems, at the equilibrium, the ions with opposite charge with respect to the wall charge will accumulate near the wall region, while the other ions will be repelled.

This results in a nonuniform distribution of ions along the channel direction perpendicular to the walls, $\hat{\boldsymbol{z}}$, which is governed by the Poisson-Boltzmann equation

$$\frac{\mathrm{d}^2\phi(z)}{\mathrm{d}z^2} = \frac{2Zc_0}{\varepsilon}\sinh\left(\beta Z\phi(z)\right) \ , \tag{7.4}$$

where $Z_a = Z_c = Z$ was assumed and c_0 is the concentration of ions. To obtain Eq. (7.4) it has been used the fact that, at the equilibrium, the ions follow a Boltzmann distribution, i.e.

$$c = c_0 \exp(\pm Z\phi(z)) \tag{7.5}$$

for both species, giving a net electrical charge density

$$\rho_E = -2Zc_0 \sinh(Z\phi(z)) \ . \tag{7.6}$$

Introducing the zeta potential ζ, i.e. the maximum $\phi(z)$ which happens at the wall, the condition

$$\beta Z\zeta \ll 1 \tag{7.7}$$

allows to substitute the hyperbolic sine in Eq. (7.4) with the identity. This is known as the Debye approximation and the resulting equation is

$$\frac{\mathrm{d}^2\phi(z)}{\mathrm{d}z^2} = \frac{2Z^2c_0\beta}{\varepsilon}\phi(z) = \frac{1}{\lambda_D^2}\phi(z) \ , \tag{7.8}$$

where λ_D is the Debye length, a parameter which controls the size of the region where the charge imbalance is present

$$\lambda_D = \sqrt{\frac{\varepsilon}{2\beta Z^2 c_0}} \ . \tag{7.9}$$

With this approximation, the Poisson-Boltzmann equation becomes linear and easily solvable

$$\phi(z) = C_1 \exp\left(\frac{z}{\lambda_D}\right) + C_2 \exp\left(-\frac{z}{\lambda_D}\right) \ , \tag{7.10}$$

where the integration constants C_1 and C_2 depend on the boundary conditions. If the system is globally neutral, the following boundary conditions hold

$$\begin{aligned} \frac{\mathrm{d}\phi}{\mathrm{d}z}\Big|_{L/2} &= \frac{\sigma_{SUP}}{\varepsilon} \,, \\ \frac{\mathrm{d}\phi}{\mathrm{d}z}\Big|_{-L/2} &= -\frac{\sigma_{INF}}{\varepsilon} \,, \end{aligned} \tag{7.11}$$

where σ_{SUP} and σ_{INF} are, respectively, the surface charges of the superior and inferior walls. Two different settings will be reproduced in the simulations, one symmetric system with both walls equally charged, i.e. $\sigma_{SUP} = \sigma_{INF} = \sigma$, and one antisymmetric system with opposite charges at the walls, i.e. $\sigma_{SUP} = -\sigma_{INF} = \sigma$. In the first case, Eq. (7.10) becomes

$$\phi(z) = \frac{\lambda_D \sigma}{\varepsilon} \frac{\cosh(x/\lambda_D)}{\sinh(L/(2\lambda_D))} \,, \tag{7.12}$$

while in the antisymmetric case

$$\phi(z) = \frac{\lambda_D \sigma}{\varepsilon} \frac{\sinh(x/\lambda_D)}{\cosh(L/(2\lambda_D))} \,. \tag{7.13}$$

In both cases the relation between the zeta potential ζ and the surface charge σ is

$$\zeta = \frac{\lambda_D \sigma}{\varepsilon \tanh(L/2\lambda_D)} \tag{7.14}$$

in the symmetric case and

$$\zeta = \frac{\lambda_D \sigma \tanh(L/2\lambda_D)}{\varepsilon} \tag{7.15}$$

in the antisymmetric case. To link the electrostatics of the problem with the hydrodynamics, the Stokes equation has to be considered

$$\boldsymbol{\nabla} P = \mu \nabla^2 \boldsymbol{u} - \rho_E \boldsymbol{\nabla} \phi_{EXT} \,, \tag{7.16}$$

where $\boldsymbol{u}$ is the velocity of the fluid, P its pressure, ρ its density, μ its viscosity and a volume force due to the electric field acting on the charged regions of fluid has been added, where ρ_E is given by Eq. (7.6), while ϕ_{EXT} is an external potential, which is assumed to act only in the $\hat{\boldsymbol{x}}$ direction and to be due to a constant electric field E, i.e. $\phi_{EXT} = Ex$. Considering Eq. (7.16) together with the incompressibility condition and the fact that the system to be studied is uniform in one direction (namely the $\hat{\boldsymbol{y}}$ direction) and imposing $\boldsymbol{u} = u_x\hat{\boldsymbol{x}}$ gives a scalar equation

$$\frac{\mathrm{d}P}{\mathrm{d}x} = \mu\frac{\mathrm{d}^2u_x}{\mathrm{d}z^2} - E\rho_E \ , \tag{7.17}$$

where the first term is a function of x and the second a function of z, meaning that both of them must be constant. Assuming that no pressure drop exists between the beginning and the end of the channel, the constant can be put to zero, giving

$$\frac{\mathrm{d}^2}{\mathrm{d}z^2}\left(u_x + \frac{E\varepsilon}{\mu}\phi\right) = 0 \ , \tag{7.18}$$

where the Poisson equation has been used to express the charge density as the second derivative of the potential. Here ϕ is the equilibrium potential as reported in Eq. (7.12) and Eq. (7.13). The general solution of Eq. (7.18) is

$$u_x(z) = -\frac{E\varepsilon}{\mu}\phi + C_3z + C_4 \ , \tag{7.19}$$

where C_3 and C_4 are integration constants. Using the no-slip boundary conditions $u_x(-L/2) = u_x(L/2) = 0$ leads for the symmetric case (ϕ given by Eq. (7.12))

$$u_x(z) = \frac{E\varepsilon}{\mu}\left(\zeta - \phi\right) \ , \tag{7.20}$$

while for the antisymmetric case (ϕ given by Eq. (7.13))

$$u_x(z) = \frac{E\varepsilon}{\mu}\left(\frac{2\zeta z}{L} - \phi\right) . \tag{7.21}$$

Defining the electroosmotic velocity

$$v_{eo} = \frac{E\varepsilon\zeta}{\mu} , \tag{7.22}$$

and the non-dimensional potential in the symmetric and antisymmetric case $\tilde{\phi}^S$ and $\tilde{\phi}^A$ as

$$\begin{aligned} \tilde{\phi}^S &= \frac{\cosh(z/\lambda_D)}{\cosh(L/(2\lambda_D))} , \\ \tilde{\phi}^A &= \frac{\sinh(z/\lambda_D)}{\sinh(L/(2\lambda_D))} , \end{aligned} \tag{7.23}$$

the velocity in the symmetric and antisymmetric case, respectively u_x^S and u_x^A can be written in a compact form

$$\begin{aligned} u_x^S &= v_{eo}\left(1 - \tilde{\phi}^S\right) , \\ u_x^A &= v_{eo}\left(\frac{2z}{L} - \tilde{\phi}^A\right) . \end{aligned} \tag{7.24}$$

These formulas are used in Section 7.6 to compare the velocity profiles resulting from the simulation with the analytical prediction.

7.4 System set-up

In order to simulate a planar channel flow a simulation box of dimension $20 \times 20 \times 10$ was set up. The walls, orthogonal to the $\hat{\boldsymbol{z}}$ axis were implemented using a reflecting boundary condition plus a layer of width 1 of fixed wall particles of constant density $\rho_{wall} = 2$. The layer of fixed particles is

needed to avoid large density fluctuations due to layering, to increase the friction properties of the wall reducing the slip length and to provide a charge to the wall. The wall particles interact with the fluid particles via a conservative repulsive force $F_{ij}^W = aw^R(r_{ij})\boldsymbol{e}_{ij}$, with $a = 200$, and via the usual dissipative and stochastic forces with dissipative parameter $\gamma_W = 1000$. The wall particles have a charge $q_w = \sigma/\rho_{wall}$ and don't exchange ions with the fluid particles. The fluid particles have a dissipative parameter $\gamma^c = \gamma^a = 30$, and an average number of cations and anions $n_0^a = n_0^c = 10$. It has been verified that with this settings, the wall reproduces well the non-slip conditions and that the viscosity of the fluid is $\mu \simeq 30$. An external electric field E parallel to the walls was applied in order to reproduce the electroosmotic flow. Both the symmetric and antisymmetric systems above described were simulated, tuning the ion charge $Z_c = Z_a = Z$ to tune the Debye length λ_D and the surface charge σ via the charge of the wall particles q_{wall}. Also, different values of the external electric field E were applied in order to tune the electroosmotic velocity v_{eo}. The simulations were run on 50 cores for 6 hours. The steps needed for the equilibration of the system were 80000, while the production steps were 160000.

7.5 Equilibrium charge distribution

After the equilibration time, it was possible to observe the presence of the Debye layer near the charged walls. Ten systems were simulated five each for the symmetric and antisymmetric setting, corresponding to three values of Debye length at fixed zeta potential and to two different values of zeta

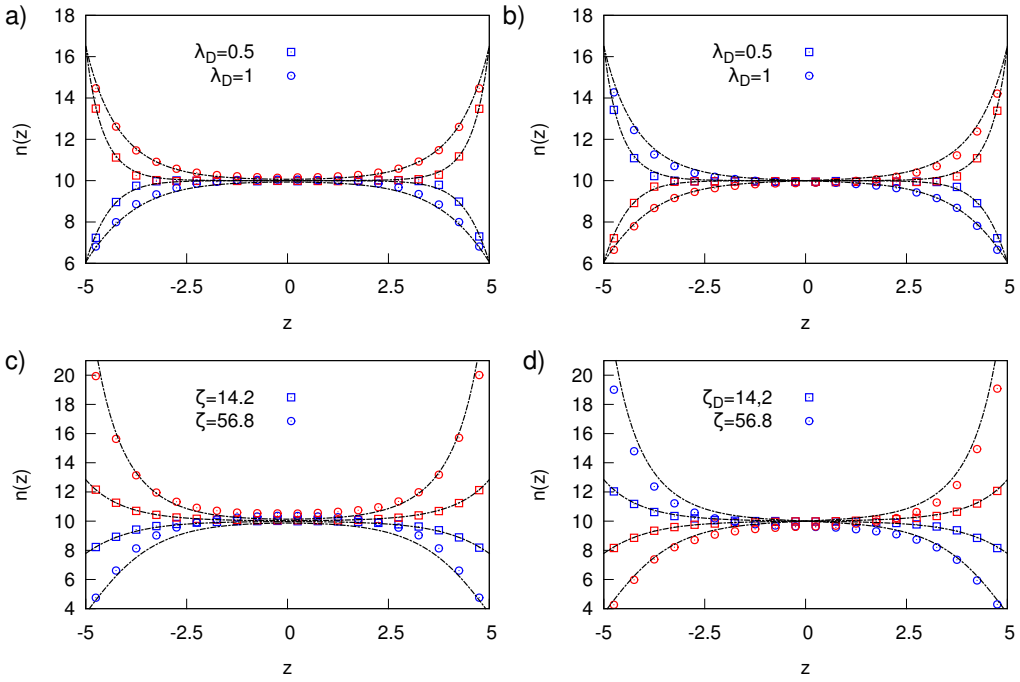

Figure 7.4: Ionic density profile for the cations (blue) and the anions (red) compared with the analytical solutions (black dashed lines). Figures a) and c) are cases with symmetric wall charges, while figures b) and d) are cases with antisymmetric wall charges. In the two top plots, two different values of the Debye length are considered anf $\zeta = 28.4$, while in the bottom plots the zeta potential is changed and $\lambda_D = 1$.

potential at fixed Debye length. The cationic and anionic density profiles are plotted in Fig. 7.4 as well as the particle electrostatic potential for both the symmetric and antisymmetric system, and compared with the analytical expressions arising from the Poisson-Boltzmann equation under the Debye approximation. The simulated ionic density is in excellent agreement with the analytical predictions for all the simulations except for the simulations carried out with the maximum zeta potential (see Fig. 7.4c). This fact seems to suggest that in those ranges of ζ, the Debye approximation on which the analytical predictions are based fails, being for those simulations $\beta Z\zeta = 1$ and being the Debye approximation valid if the condition of Eq. (7.7) is met.

7.6 Electroosmotic flow

The application of an external electric field directed parallel to the channel walls generates a net mass flow due to the charge imbalance near the walls, the electroosmotic flow. The resulting velocity profile for different Debye lengths and electroosmotic velocities is plotted in Fig. 7.5 and compared with the analytical prediction, showing a good agreement.

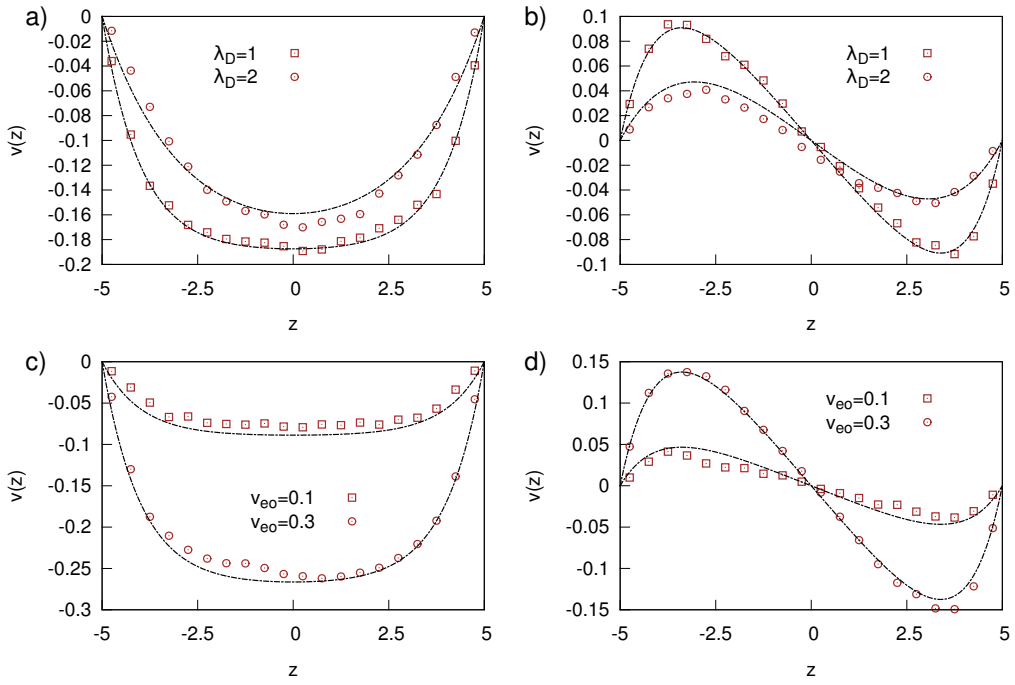

Figure 7.5: Velocity profile of the electroosmotic flow generated by a constant electric field parallel to the walls compared with the analytical solutions (black dashed lines). Figures a) and c) correspond to cases with symmetric wall charges, while figures b) and d) are cases with antisymmetric wall charges. In the two top plots, two different values of the Debye length are considered, while in the bottom plots the electroosmotic velocity is changed by changing the electric field and $\lambda_D = 1$. In all the plots, $\zeta = 28.4$.

Part IV

Conclusions

In this thesis a coarse-graining approach is used to study typical problems arising when dealing with complex mesoscale systems such as nanopore sensors. Specifically, the work has been focused on two of the many physical phenomena which are relevant for nanopore systems. The first problem is the effect of a confined environment, and thus of hydrodynamic interactions, on the diffusive dynamics of rigid particles, including both translations and rotations. To address this problem, a Brownian Dynamics approach has been used, writing the rotational Langevin equations in the quaternion formalism to represent rotations in a way which accounts for a spatially dependent mobility. The effect of confinement is then to modify the structure of the mobility matrix and, as a consequence, of the stochastic forcing acting on the rigid particle. To simulate the roto-translational diffusive motion, the mobility matrix is thus needed as an input which contains all the information concerning the solvent and the walls. As a tool to compute the mobility matrix a coarse-grained technique in which the fluid is constituted by interacting particles, Dissipative Particle Dynamics, has been used developing a

model for the boundaries which is able to reproduce the non-slip conditions even for curved surfaces. As a case of study a rigid spherical particle in a cylindrical nanochannel has been chosen. The mobility matrix was computed as a function of the radial position of the particle, and was the input of the rigid body Brownian simulations. The axial translational diffusion of the particle under confinement has been computed, resulting in agreement with analytical approximations, other numerical methods and experimental data in quantifying a reduction of 25-70% with respect to the bulk diffusion for confinement ratios in the range 3-10. The rotational diffusion under confinement has also been computed, finding that it is also reduced, reaching the 75% of its bulk value in the same range of confinement ratios. The Brownian simulations have also been used to study the effects of external forces on particle diffusion. A constant force transverse with respect to the channel axis reduces the translational diffusion up to an additional 10% with respect to the value in absence of forces, and has a similar effect also on the rotational diffusion. The case of the electrostatic force which a constant axial electric field exerts on a particle with a constant dipole moment has also been explored, finding no relevant differences in the diffusion coefficient. This kind of Brownian Dynamics simulations can be easily extended to the case of other external forces which, by modifying the particle distribution inside the channel, alter their diffusion, and to more complex systems, provided the mobility matrix.

The second problem addressed in this thesis is the problem of electrohydrodynamics, i.e., the fluid-electric field coupling that exists in electrolyte solutions. To address this problem, a new coarse-grained method has been

formulated. The method is based on the structure of stochastic differential equations of DPD, expanding them to add two new degrees of freedom for each particle, namely the quantity of cations and anions carried by the particle. The Fokker-Planck equation associated to the system of equations is obtained, and the fluctuation-dissipation conditions necessary to guarantee the existence of an equilibrium solution are obtained. Moreover, a statistical mechanics interpretation is given to the function governing the equilibrium, which is interpreted as the total entropy of the system. Assuming that each particle is locally at the equilibrium, the tools of statistical mechanics can be used in order to find a physically meaningful functional form for the fluxes governing the equations of motion. It has been shown that the transport coefficients such as the ionic mobility can be tuned by changing the parameters of the model, and that the conductivity of the solution grows linearly with the quantity of ions in solution, at least in the range of values which has been tested. Finally, the model has been implemented in the LAMMPS parallel computing software and validated against some cases of planar electroosmotic flows for which an (approximated) analytical solution exists.

Bibliography

[1] Jayesh A Bafna and Gautam V Soni. Fabrication of low noise borosilicate glass nanopores for single molecule sensing. *PloS one*, 11(6):e0157399, 2016.

[2] Yifang Chen. Nanofabrication by electron beam lithography and its applications: A review. *Microelectronic Engineering*, 135:57–72, 2015.

[3] Xin Sun and Hao Li. A review: Nanofabrication of surface-enhanced raman spectroscopy (sers) substrates. *Current Nanoscience*, 12(2):175–183, 2016.

[4] Wubin Bai, Tairong Kuang, Chandani Chitrakar, Ruiguo Yang, Shulin Li, Donghui Zhu, and Lingqian Chang. Patchable micro/nanodevices interacting with skin. *Biosensors and Bioelectronics*, 122:189–204, 2018.

[5] Yunus Alapan, Kutay Icoz, and Umut A Gurkan. Micro-and nanodevices integrated with biomolecular probes. *Biotechnology advances*, 33(8):1727–1743, 2015.

[6] Stephanie J Heerema and Cees Dekker. Graphene nanodevices for dna sequencing. *Nature nanotechnology*, 11(2):127, 2016.

[7] J Justin Gooding and Katharina Gaus. Single-molecule sensors: Challenges and opportunities for quantitative analysis. *Angewandte Chemie International Edition*, 55(38):11354–11366, 2016.

[8] Mathilde Lepoitevin, Mikhael Bechelany, Jean-Marc Janot, and Sebastien Balme. Nanopore functionalization for biological channel mimicking. *Science Letters*, 4:188, 2015.

[9] Leonardo Vicarelli, Stephanie J Heerema, Cees Dekker, and Henny W Zandbergen. Controlling defects in graphene for optimizing the electrical properties of graphene nanodevices. *ACS nano*, 9(4):3428–3435, 2015.

[10] YM Nuwan DY Bandara, Buddini Iroshika Karawdeniya, and Jason R Dwyer. Real-time profiling of solid-state nanopores during solution-phase nanofabrication. *ACS applied materials & interfaces*, 8(44):30583–30589, 2016.

[11] Anish Tuteja, Michael E Mackay, Suresh Narayanan, Subashini Asokan, and Michael S Wong. Breakdown of the continuum stokes- einstein relation for nanoparticle diffusion. *Nano letters*, 7(5):1276–1281, 2007.

[12] Jun Liu, Dapeng Cao, and Liqun Zhang. Molecular dynamics study on nanoparticle diffusion in polymer melts: a test of the stokes- einstein law. *The journal of physical chemistry C*, 112(17):6653–6661, 2008.

[13] Taehoon Kim, Chang-Ha Lee, Sang-Woo Joo, and Kangtaek Lee. Kinetics of gold nanoparticle aggregation: experiments and modeling. *Journal of colloid and interface science*, 318(2):238–243, 2008.

[14] Ernest M Hotze, Tanapon Phenrat, and Gregory V Lowry. Nanoparticle aggregation: challenges to understanding transport and reactivity in the environment. *Journal of environmental quality*, 39(6):1909–1924, 2010.

[15] Yan Xu. Nanofluidics: Nanofluidics: A new arena for materials science (adv. mater. 3/2018). *Advanced Materials*, 30(3):1870019, 2018.

[16] Jonas Heverhagen, Mykola Tasinkevych, Atikur Rahman, Charles T Black, and Antonio Checco. Slip length enhancement in nanofluidic flow using nanotextured superhydrophobic surfaces. *Advanced Materials Interfaces*, 3(17):1600303, 2016.

[17] Eleonora Secchi, Sophie Marbach, Antoine Niguès, Derek Stein, Alessandro Siria, and Lydéric Bocquet. Massive radius-dependent flow slippage in carbon nanotubes. *Nature*, 537(7619):210, 2016.

[18] Joshua Edel, Aleksandar Ivanov, and MinJun Kim. *Nanofluidics*. Royal Society of Chemistry, 2016.

[19] Daniel V Verschueren, Sergii Pud, Xin Shi, Lorenzo De Angelis, L Kuipers, and Cees Dekker. Label-free optical detection of dna translocations through plasmonic nanopores. *ACS nano*, 13(1):61–70, 2018.

[20] Cees Dekker. Solid-state nanopores. *Nature nanotechnology*, 2(4):209–215, 2007.

[21] Christopher Maffeo, Swati Bhattacharya, Jejoong Yoo, David Wells, and Aleksei Aksimentiev. Modeling and simulation of ion channels. *Chemical reviews*, 112(12):6250–6284, 2012.

[22] Wenqing Shi, Alicia K Friedman, and Lane A Baker. Nanopore sensing. *Analytical chemistry*, 89(1):157–188, 2016.

[23] David Deamer, Mark Akeson, and Daniel Branton. Three decades of nanopore sequencing. *Nature biotechnology*, 34(5):518, 2016.

[24] Grégory F Schneider and Cees Dekker. Dna sequencing with nanopores. *Nature biotechnology*, 30(4):326, 2012.

[25] Pradeep Waduge, Rui Hu, Prasad Bandarkar, Hirohito Yamazaki, Benjamin Cressiot, Qing Zhao, Paul C Whitford, and Meni Wanunu. Nanopore-based measurements of protein size, fluctuations, and conformational changes. *ACS nano*, 11(6):5706–5716, 2017.

[26] Jiandong Feng, Michael Graf, Ke Liu, Dmitry Ovchinnikov, Dumitru Dumcenco, Mohammad Heiranian, Vishal Nandigana, Narayana R Aluru, Andras Kis, and Aleksandra Radenovic. Single-layer mos 2 nanopores as nanopower generators. *Nature*, 536(7615):197, 2016.

[27] Kherim Willems, Veerle Van Meervelt, Carsten Wloka, and Giovanni Maglia. Single-molecule nanopore enzymology. *Philosophical Transactions of the Royal Society B: Biological Sciences*, 372(1726):20160230, 2017.

[28] Calin Plesa, Daniel Verschueren, Sergii Pud, Jaco van der Torre, Justus W Ruitenberg, Menno J Witteveen, Magnus P Jonsson, Alexan-

der Y Grosberg, Yitzhak Rabin, and Cees Dekker. Direct observation of dna knots using a solid-state nanopore. *Nature nanotechnology*, 11(12):1093, 2016.

[29] Alina Asandei, Irina Schiopu, Mauro Chinappi, Chang Ho Seo, Yoonkyung Park, and Tudor Luchian. Electroosmotic trap against the electrophoretic force near a protein nanopore reveals peptide dynamics during capture and translocation. *ACS applied materials & interfaces*, 8(20):13166–13179, 2016.

[30] Alina Asandei, Mauro Chinappi, Jong-kook Lee, Chang Ho Seo, Loredana Mereuta, Yoonkyung Park, and Tudor Luchian. Placement of oppositely charged aminoacids at a polypeptide termini determines the voltage-controlled braking of polymer transport through nanometer-scale pores. *Scientific reports*, 5:10419, 2015.

[31] Nicoletta Giamblanco, Diego Coglitore, Alberto Gubbiotti, Tianji Ma, Emmanuel Balanzat, Jean-Marc Janot, Mauro Chinappi, and Sebastien Balme. Amyloid growth, inhibition, and real-time enzymatic degradation revealed with single conical nanopore. *Analytical chemistry*, 2018.

[32] Daizo Hamada and Christopher M Dobson. A kinetic study of β-lactoglobulin amyloid fibril formation promoted by urea. *Protein Science*, 11(10):2417–2426, 2002.

[33] Simon M Loveday, Jiahong Su, M Anandha Rao, Skelte G Anema, and Harjinder Singh. Effect of calcium on the morphology and functional-

ity of whey protein nanofibrils. *Biomacromolecules*, 12(10):3780–3788, 2011.

[34] Tuomas PJ Knowles, Michele Vendruscolo, and Christopher M Dobson. The amyloid state and its association with protein misfolding diseases. *Nature reviews Molecular cell biology*, 15(6):384–396, 2014.

[35] Mauro Manno, Emanuela Fabiola Craparo, Vincenzo Martorana, Donatella Bulone, and Pier Luigi San Biagio. Kinetics of insulin aggregation: disentanglement of amyloid fibrillation from large-size cluster formation. *Biophysical journal*, 90(12):4585–4591, 2006.

[36] Giovanni Di Muccio, Aldo Eugenio Rossini, Daniele Di Marino, Giuseppe Zollo, and Mauro Chinappi. Insights into protein sequencing with an α-hemolysin nanopore by atomistic simulations. *Scientific reports*, 9(1):6440, 2019.

[37] Erik C Yusko, Brandon R Bruhn, Olivia M Eggenberger, Jared Houghtaling, Ryan C Rollings, Nathan C Walsh, Santoshi Nandivada, Mariya Pindrus, Adam R Hall, David Sept, et al. Real-time shape approximation and fingerprinting of single proteins using a nanopore. *Nature nanotechnology*, 12(4):360, 2017.

[38] William A Catterall, Indira M Raman, Hugh PC Robinson, Terrence J Sejnowski, and Ole Paulsen. The hodgkin-huxley heritage: from channels to circuits. *Journal of Neuroscience*, 32(41):14064–14073, 2012.

[39] Kyaw Sint, Boyang Wang, and Petr Král. Selective ion passage through functionalized graphene nanopores. *Journal of the American Chemical Society*, 130(49):16448–16449, 2008.

[40] Chih-Chang Chang and Ruey-Jen Yang. Electrokinetic energy conversion efficiency in ion-selective nanopores. *Applied Physics Letters*, 99(8):083102, 2011.

[41] Jongho Lee and Rohit Karnik. Desalination of water by vapor-phase transport through hydrophobic nanopores. *Journal of Applied Physics*, 108(4):044315, 2010.

[42] Alessandro Siria, Marie-Laure Bocquet, and Lydéric Bocquet. New avenues for the large-scale harvesting of blue energy. *Nature Reviews Chemistry*, 1(11):0091, 2017.

[43] Daniele Di Marino, Emma Letizia Bonome, Anna Tramontano, and Mauro Chinappi. All-atom molecular dynamics simulation of protein translocation through an α-hemolysin nanopore. *The journal of physical chemistry letters*, 6(15):2963–2968, 2015.

[44] Mauro Chinappi and Fabio Cecconi. Protein sequencing via nanopore based devices: a nanofluidics perspective. *Journal of Physics: Condensed Matter*, 30(20):204002, 2018.

[45] Jared Houghtaling, Cuifeng Ying, Olivia M Eggenberger, Aziz Fennouri, Santoshi Nandivada, Mitu Acharjee, Jiali Li, Adam R Hall, and Michael Mayer. Estimation of shape, volume, and dipole moment of

individual proteins freely transiting a synthetic nanopore. *ACS nano*, 2019.

[46] Laetitia Jubin, Anthony Poggioli, Alessandro Siria, and Lydéric Bocquet. Dramatic pressure-sensitive ion conduction in conical nanopores. *Proceedings of the National Academy of Sciences*, 115(16):4063–4068, 2018.

[47] Nadanai Laohakunakorn, Vivek V Thacker, Murugappan Muthukumar, and Ulrich F Keyser. Electroosmotic flow reversal outside glass nanopores. *Nano letters*, 15(1):695–702, 2014.

[48] Hirokazu Watanabe, Alberto Gubbiotti, Mauro Chinappi, Natsumi Takai, Koji Tanaka, Kouhei Tsumoto, and Ryuji Kawano. Analysis of pore formation and protein translocation using large biological nanopores. *Analytical Chemistry*, 2017.

[49] M Muthukumar. Communication: Charge, diffusion, and mobility of proteins through nanopores, 2014.

[50] Maxi San Miguel and Raul Toral. Stochastic effects in physical systems. *Instabilities and nonequilibrium structures VI*, 5:35–127, 2000.

[51] Nicolaas Godfried Van Kampen. *Stochastic processes in physics and chemistry*, volume 1. Elsevier, 1992.

[52] Sangtae Kim and Seppo J Karrila. *Microhydrodynamics: principles and selected applications*. Courier Corporation, 2013.

[53] Alberto Gubbiotti, Mauro Chinappi, and Carlo Massimo Casciola. Confinement effects on the dynamics of a rigid particle in a nanochannel. *Physical Review E*, 100(5):053307, 2019.

[54] Henrik Bruus. *Theoretical microfluidics*, volume 18. Oxford university press Oxford, 2008.

[55] Antonio Ramos. *Electrokinetics and electrohydrodynamics in microsystems*, volume 530. Springer Science & Business Media, 2011.

[56] Erik C Yusko, Ran An, and Michael Mayer. Electroosmotic flow can generate ion current rectification in nano-and micropores. *Acs Nano*, 4(1):477–487, 2009.

[57] Emma Letizia Bonome, Fabio Cecconi, and Mauro Chinappi. Electroosmotic flow through an α-hemolysin nanopore. *Microfluidics and Nanofluidics*, 21(5):96, 2017.

[58] Mordjane Boukhet, Fabien Piguet, Hadjer Ouldali, Manuela Pastoriza-Gallego, Juan Pelta, and Abdelghani Oukhaled. Probing driving forces in aerolysin and α-hemolysin biological nanopores: electrophoresis versus electroosmosis. *Nanoscale*, 8(43):18352–18359, 2016.

[59] Gang Huang, Kherim Willems, Misha Soskine, Carsten Wloka, and Giovanni Maglia. Electro-osmotic capture and ionic discrimination of peptide and protein biomarkers with frac nanopores. *Nature communications*, 8(1):935, 2017.

[60] Mauro Chinappi and Paolo Malgaretti. Charge polarization, local electroneutrality breakdown and eddy formation due to electroosmosis in varying-section channels. *Soft matter*, 14(45):9083–9087, 2018.

[61] Pep Español and Patrick B Warren. Perspective: Dissipative particle dynamics. *The Journal of Chemical Physics*, 146(15):150901, 2017.

[62] Andy WC Lau and Tom C Lubensky. State-dependent diffusion: Thermodynamic consistency and its path integral formulation. *Physical Review E*, 76(1):011123, 2007.

[63] PJ Hoogerbrugge and JMVA Koelman. Simulating microscopic hydrodynamic phenomena with dissipative particle dynamics. *EPL (Europhysics Letters)*, 19(3):155, 1992.

[64] Pep Espanol and Patrick Warren. Statistical mechanics of dissipative particle dynamics. *EPL (Europhysics Letters)*, 30(4):191, 1995.

[65] Robert D Groot and Patrick B Warren. Dissipative particle dynamics: Bridging the gap between atomistic and mesoscopic simulation. *The Journal of chemical physics*, 107(11):4423–4435, 1997.

[66] Arman Boromand, Safa Jamali, and Joao M Maia. Viscosity measurement techniques in dissipative particle dynamics. *Computer Physics Communications*, 196:149–160, 2015.

[67] Dan S Bolintineanu, Gary S Grest, Jeremy B Lechman, Flint Pierce, Steven J Plimpton, and P Randall Schunk. Particle dynamics modeling methods for colloid suspensions. *Computational Particle Mechanics*, 1(3):321–356, 2014.

[68] Pep Espanol and Mariano Revenga. Smoothed dissipative particle dynamics. *Physical Review E*, 67(2):026705, 2003.

[69] I Pagonabarraga and D Frenkel. Dissipative particle dynamics for interacting systems. *The Journal of Chemical Physics*, 115(11):5015–5026, 2001.

[70] J Bonet Avalos and AD Mackie. Dissipative particle dynamics with energy conservation. *EPL (Europhysics Letters)*, 40(2):141, 1997.

[71] Pep Espanol. Dissipative particle dynamics with energy conservation. *EPL (Europhysics Letters)*, 40(6):631, 1997.

[72] Zhen Li, Alireza Yazdani, Alexandre Tartakovsky, and George Em Karniadakis. Transport dissipative particle dynamics model for mesoscopic advection-diffusion-reaction problems. *The Journal of chemical physics*, 143(1):014101, 2015.

[73] Mingge Deng, Zhen Li, Oleg Borodin, and George Em Karniadakis. cdpd: A new dissipative particle dynamics method for modeling electrokinetic phenomena at the mesoscale. *The Journal of chemical physics*, 145(14):144109, 2016.

[74] Dinar Katanov, Gerhard Gompper, and Dmitry A Fedosov. Microvascular blood flow resistance: role of red blood cell migration and dispersion. *Microvascular research*, 99:57–66, 2015.

[75] Ansel L Blumers, Yu-Hang Tang, Zhen Li, Xuejin Li, and George E Karniadakis. Gpu-accelerated red blood cells simulations with trans-

port dissipative particle dynamics. *Computer physics communications*, 217:171–179, 2017.

[76] T Kreer. Polymer-brush lubrication: a review of recent theoretical advances. *Soft Matter*, 12(15):3479–3501, 2016.

[77] Emanuel K Peter, Kirill Lykov, and Igor V Pivkin. A polarizable coarse-grained protein model for dissipative particle dynamics. *Physical Chemistry Chemical Physics*, 17(37):24452–24461, 2015.

[78] GJA Sevink and JGEM Fraaije. Efficient solvent-free dissipative particle dynamics for lipid bilayers. *Soft Matter*, 10(28):5129–5146, 2014.

[79] Yuxiang Wang and Shuo Chen. Droplets impact on textured surfaces: mesoscopic simulation of spreading dynamics. *Applied Surface Science*, 327:159–167, 2015.

[80] Robert D Groot. Electrostatic interactions in dissipative particle dynamicssimulation of polyelectrolytes and anionic surfactants. *The Journal of chemical physics*, 118(24):11265–11277, 2003.

[81] Minerva González-Melchor, Estela Mayoral, María Eugenia Velázquez, and José Alejandre. Electrostatic interactions in dissipative particle dynamics using the ewald sums. *The Journal of chemical physics*, 125(22):224107, 2006.

[82] Dissipative particle dynamics study of electrostatic self-assembly in aqueous mixtures of copolymers containing one neutral water-soluble block and one either positively or negatively charged polyelectrolyte block.

[83] Martin Lísal, Zuzana Limpouchová, and Karel Procházka. The self-assembly of copolymers with one hydrophobic and one polyelectrolyte block in aqueous media: a dissipative particle dynamics study. *Physical Chemistry Chemical Physics*, 18(24):16127–16136, 2016.

[84] Arthur Sherburne Hardy. *Elements of quaternions*. Ginn, Heath, & Company, 1881.

[85] John Voight. Quaternion algebras. *Version v0*, 9(3), 2017.

[86] Peter Betsch and Ralf Siebert. Rigid body dynamics in terms of quaternions: Hamiltonian formulation and conserving numerical integration. *International journal for numerical methods in engineering*, 79(4):444–473, 2009.

[87] Martin Bjerre Nielsen and Steen Krenk. Conservative integration of rigid body motion by quaternion parameters with implicit constraints. *International Journal for Numerical Methods in Engineering*, 92(8):734–752, 2012.

[88] Steven Delong, Florencio Balboa Usabiaga, and Aleksandar Donev. Brownian dynamics of confined rigid bodies. *The Journal of chemical physics*, 143(14):144107, 2015.

[89] Ioana M Ilie, Wim J Briels, and Wouter K den Otter. An elementary singularity-free rotational brownian dynamics algorithm for anisotropic particles. *The Journal of chemical physics*, 142(11):03B610_1, 2015.

[90] Desmond J Higham. An algorithmic introduction to numerical simulation of stochastic differential equations. *SIAM review*, 43(3):525–546, 2001.

[91] MB Liu, GR Liu, LW Zhou, and JZ Chang. Dissipative particle dynamics (dpd): an overview and recent developments. *Archives of Computational Methods in Engineering*, 22(4):529–556, 2015.

[92] M Revenga, I Zuniga, and P Espanol. Boundary conditions in dissipative particle dynamics. *Computer physics communications*, 121:309–311, 1999.

[93] Igor V Pivkin and George Em Karniadakis. Controlling density fluctuations in wall-bounded dissipative particle dynamics systems. *Physical review letters*, 96(20):206001, 2006.

[94] Jens Smiatek, Michael P Allen, and Friederike Schmid. Tunable-slip boundaries for coarse-grained simulations of fluid flow. *The European Physical Journal E*, 26(1-2):115–122, 2008.

[95] S Kumar Ranjith, BSV Patnaik, and Srikanth Vedantam. No-slip boundary condition in finite-size dissipative particle dynamics. *Journal of Computational Physics*, 232(1):174–188, 2013.

[96] Zhen Li, Xin Bian, Yu-Hang Tang, and George Em Karniadakis. A dissipative particle dynamics method for arbitrarily complex geometries. *Journal of Computational Physics*, 355:534–547, 2018.

[97] Olga I Vinogradova. Slippage of water over hydrophobic surfaces. *International journal of mineral processing*, 56(1-4):31–60, 1999.

[98] Eric Lauga, Michael Brenner, and Howard Stone. Microfluidics: the no-slip boundary condition. *Springer handbook of experimental fluid mechanics*, pages 1219–1240, 2007.

[99] Luyang Zhao, Yaning Zhong, Yanli Wei, Nathalia Ortiz, Fang Chen, and Gufeng Wang. Microscopic movement of slow-diffusing nanoparticles in cylindrical nanopores studied with three-dimensional tracking. *Analytical chemistry*, 88(10):5122–5130, 2016.

[100] Panadda Dechadilok and William M Deen. Hindrance factors for diffusion and convection in pores. *Industrial & Engineering Chemistry Research*, 45(21):6953–6959, 2006.

[101] Eugene M Renkin. Filtration, diffusion, and molecular sieving through porous cellulose membranes. *The Journal of general physiology*, 38(2):225–243, 1954.

[102] JJL Higdon and GP Muldowney. Resistance functions for spherical particles, droplets and bubbles in cylindrical tubes. *Journal of Fluid Mechanics*, 298:193–210, 1995.

[103] Daniela J Kraft, Raphael Wittkowski, Borge Ten Hagen, Kazem V Edmond, David J Pine, and Hartmut Löwen. Brownian motion and the hydrodynamic friction tensor for colloidal particles of complex shape. *Physical Review E*, 88(5):050301, 2013.

[104] Kerson Huang. *Statistical Mechanics*. Wiley, 1987.

[105] Péter T Kiss, Marcello Sega, and András Baranyai. Efficient handling of gaussian charge distributions: An application to polarizable molecu-

lar models. *Journal of chemical theory and computation*, 10(12):5513–5519, 2014.

[106] Theodore Shedlovsky. An equation for electrolytic conductance. *Journal of the American Chemical Society*, 54(4):1405–1411, 1932.

[107] Steve Plimpton. Fast parallel algorithms for short-range molecular dynamics. *Journal of computational physics*, 117(1):1–19, 1995.

[108] Michael P Allen and Dominic J Tildesley. *Computer simulation of liquids*. Oxford university press, 2017.

[109] Cundari Thomas R Lipkowitz, Kenny B and Donald B Boyd. *Reviews in Computational Chemistry 24*. Wiley Online Library, 2007.